UNIVERSIDADE FEDERAL DO RIO GRANDE DO SUL

INSTITUTO DE GEOCIÊNCIAS

PROGRAMA DE PÓS-GRADUAÇÃO EM GEOCIÊNCIAS

GEOLOGIA E GEOQUÍMICA DA ZONA INFERIOR DO CORPO DE MINÉRIO INGÁ, DISTRITO AURÍFERO DE CRIXÁS, GOIÁS, BRASIL: IMPLICAÇÕES GENÉTICAS E EXPLORATÓRIAS

MARCO ANTÔNIO SARTORI CASTOLDI

ORIENTADOR: Prof. Dr. José Carlos Frantz

COORIENTADORA: Profª. Drª. Juliana Charão Marques

Porto Alegre – 2018

UNIVERSIDADE FEDERAL DO RIO GRANDE DO SUL

INSTITUTO DE GEOCIÊNCIAS

PROGRAMA DE PÓS-GRADUAÇÃO EM GEOCIÊNCIAS

GEOLOGIA E GEOQUÍMICA DA ZONA INFERIOR DO CORPO DE MINÉRIO INGÁ, DISTRITO AURÍFERO DE CRIXÁS, GOIÁS, BRASIL: IMPLICAÇÕES GENÉTICAS E EXPLORATÓRIAS

MARCO ANTÔNIO SARTORI CASTOLDI

ORIENTADOR: Prof. Dr. José Carlos Frantz

COORIENTADORA: Profª. Drª. Juliana Charão Marques

BANCA EXAMINADORA

      Prof. Dr. Artur Cezar Bastos Neto

         Instituto de Geociências – Universidade Federal do Rio Grande do Sul

      Prof. Dr. Artur Lemos Giovannini

         Instituto de Geociências – Universidade Federal do Rio Grande do Sul

      Prof. Dr. Diego Machado Marques

         Instituto de Geociências – Universidade Federal do Rio Grande do Sul

Dissertação de Mestrado apresentada como requisito parcial para a obtenção do Título de Mestre em Geociências

Porto Alegre – 2018

AGRADECIMENTOS

RESUMO

O corpo de minério Ingá foi descoberto em 2012 e é localizado na Unidade Serra Grande da AngloGold Ashanti, depósito de classe mundial no Distrito Aurífero de Crixás, Brasil central. Localizado nas rochas supracrustais, o corpo Ingá é dividido em Zona Superior e Zona Inferior. A Zona Superior contém lentes de sulfeto maciço hospedadas em dolomitos. A Zona Inferior foi sistematicamente estudada por DRX, FRX, ICP-MS, microssonda eletrônica e LA-ICP-MS. É controlada por uma falha de empurrão de baixo ângulo principal (Estrutura III) e suas litologias incluem, do topo para a base: dolomitos, filito carbonoso (GXN), veio de quartzo massivo (VQZ), quartzo-clorita-sericita-granada xisto e metagrauvaca com dois raros tipos de dique cortando a estratigrafia. Halos de alteração hidrotermal desenvolveram-se a partir da Estrutura III: silicificação, potássico, fílico e carbonático. A mineralização ocorre em três diferentes estágios. Três tipos de arsenopirita foram identificados: Aspy1 (cedo hidrotermal), Aspy2 (tardi hidrotermal, possivelmente rica em ouro invisível) e Aspy3 (tardi hidrotermal, rica em ouro visível como inclusões, preenchendo fraturas ou ao longo de suas margens). Ouro visível também ocorre como cristais livres nos níveis basais do VQZ e na matriz do GXN. Possível remobilização de ouro invisível inferido em Aspy2 para formar ouro visível em Aspy3 ao longo de fraturas tardias e alteração seletiva em direção às margens dos cristais, ocorreu como consequência do dobramento F2, aumentando a quantidade de ouro passível de extração no corpo de minério. Os gráficos de Bi ppm x Se ppm e S % x Bi ppm e consideráveis ganhos de As, Ni e Co na zona de silicificação sobre GXN rico em arsenopirita, podem ser usados para identificar zonas potencialmente ricas em ouro. Quatro parâmetros prospectivos foram estabelecidos: VQZ, Aspy2 e Aspy3, falhas de acomodação e zona de silicificação.

Palavras-chave: Ouro; Crixás; Greenstone; Mineralização; Arsenopirita.

ABSTRACT

The Ingá orebody was discovered in 2012 and is located in the world-class AngloGold Ashanti – Serra Grande Unit of the Crixás Gold District, Central Brazil. Located in the supracrustal rocks, Ingá is divided into Upper and Lower Zones. The Upper Zone contains massive sulfide lenses hosted in dolomites. The Lower Zone was systematically studied by XRD, XRF, ICP-MS, EMP and LA-ICP-MS. It is controlled by a major low angle thrust fault (Structure III) and lithologies include, from top to bottom: dolomites, carbonaceous phyllite (GXN), major quartz vein (VQZ), quartz-chlorite-sericite-garnet schist, and metagraywacke with two types of rare cross-cutting dikes. Hydrothermal alteration haloes developed outwards from Structure III: silicification, potassic, phyllic and carbonatic. Mineralization occurs in three different stages. Three types of arsenopyrite were identified: Aspy1 (early hydrothermal), Aspy2 (late hydrothermal, possibly invisible gold-rich) and Aspy3 (later hydrothermal, visible gold-rich as inclusions, filling fractures or along its margins). Visible gold also occurs as free crystals in the VQZ basal levels and in the GXN matrix. Possible remobilization of inferred invisible gold in Aspy2 to form visible gold in Aspy3 along late crystal fractures and selective alteration towards the margins occurred as consequence of F2 folding, increasing the orebody gold budget. The Bi ppm x Se ppm and S percent x Bi ppm plots and major gains in As, Ni and Co in the arsenopyrite rich GXN silicification zone could be used to identify potentially gold rich zones. Four prospective parameters were established: VQZ, Aspy2 and Aspy3, accommodation faults, and silicification zone.

Keywords: Gold; Crixás; Greenstone; Mineralization; Arsenopyrite.

SUMÁRIO

1. INTRODUÇÃO

O distrito aurífero de Crixás constitui o quarto maior distrito de ouro atualmente em produção no Brasil. A região e seu potencial aurífero, explorada como garimpos desde o século XVIII pelos Bandeirantes, foi consolidada a partir da década de 1980 com o estabelecimento da Mineração Serra Grande (mineração subterrânea mecanizada), posteriormente objeto de negociações empresariais e atualmente controlada totalmente pela empresa AngloGold Ashanti – Serra Grande.

Nos últimos anos, programas de exploração mineral para ampliação de recursos e reservas resultaram no descobrimento de novos corpos mineralizados a ouro, como o corpo Ingá em 2012. Possuindo 0.59 MOz de ouro a um teor médio de 5.91 g/t (31/12/2017), o corpo Ingá iniciou sua produção em 2017. A caracterização do corpo de minério Ingá está vinculada a projeto do grupo de trabalho da Universidade Federal do Rio Grande do Sul junto a AngloGold Ashanti – Serra Grande que objetiva investir na caracterização geológica e da alteração hidrotermal de corpos de minério descobertos recentemente no distrito aurífero de Crixás, como o corpo Palmeiras em 2006 (Almeida, 2006), Pequizão em 2011 (Sobiesiak, 2011) e Mangaba em 2018 (de Souza, em andamento). Além disso, o presente estudo visa contribuir no entendimento da gênese e configuração do corpo e sua mineralização aurífera, de modo a contribuir para futuras novas descobertas de corpos de minério no *greenstone belt* de Crixás.

1.1. SOBRE A ESTRUTURA DA DISSERTAÇÃO

A presente dissertação de mestrado está estruturada em torno de artigo submetido a periódico. Sua organização compreende as seguintes partes principais:

a) Introdução sobre o tema e descrição do objeto de pesquisa, onde se sumariza os objetivos e estado da arte;

b) Artigo submetido a periódico com corpo editorial permanente e revisores independentes, escrito pelo autor durante o desenvolvimento de seu mestrado, com comprovante de submissão;

c) Referências bibliográficas citadas no capítulo 1 dessa dissertação;

d) Histórico escolar do autor contendo as disciplinas cursadas e respectivas notas durante o mestrado;

e) Pareceres da banca examinadora composta por três professores doutores.

1.2.   OBJETIVOS

O presente trabalho tem como objetivo principal avançar no conhecimento da evolução geológica e metalogenética da zona inferior do corpo mineralizado Ingá, do *greenstone belt* de Crixás, através da caraterização petrográfica e geoquímica do corpo.

Entre os objetivos específicos, destacam-se:

- Caracterizar a petrografia e a geoquímica das rochas hospedeiras, halos de alteração hidrotermal e a mineralização aurífera;

- Caracterizar a associação entre ouro e arsenopirita;

- Discutir a gênese do corpo de minério Ingá;

- Discutir a concentração de ouro na base do veio de quartzo massivo;

- Estabelecer parâmetros prospectivos que a indústria possa utilizar.

1.3.   ESTADO DA ARTE E CONTEXTUALIZAÇÃO TEÓRICA

1.3.1. Depósitos de ouro do tipo veio de quartzo-carbonato em *greenstone belts*

De acordo com a classificação de Robert *et al.* (1997), há dezesseis tipos diferentes de depósitos de ouro, formados em diferentes ambientes geológicos e profundidades crustais. O depósito de ouro do tipo veio de quartzo-carbonato em *greenstone belt* é a classificação atribuída ao depósito e corpo de minério do presente estudo: Corpo Ingá, Mina de Serra Grande, *greenstone belt* de Crixás (Figura 1). Alguns outros exemplos no mundo são: Mt. Charlotte, Norseman, Victory (Australia), Giant, Contact Lake, San Antonio, Dome, Kerr Addison, Sigma-Lamaque (Canada), Mother Lode e Grass Valley (EUA). Este tipo de depósito é espacialmente associado a zonas de falhas expressivas em terrenos *greenstone* deformados, com

venulações mineralizadas associadas a zonas de cisalhamento dúcteis-rúpteis e localmente relacionados a falhas extensionais.
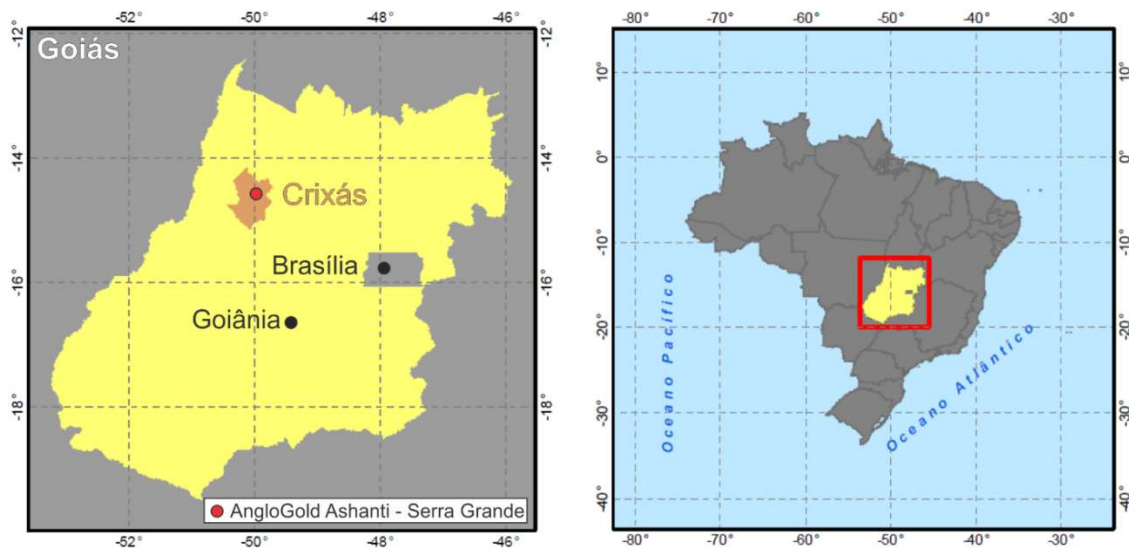
Figura 1. Localização do município de Crixás e dependências da AngloGold Ashanti – Serra Grande. Modificado de Matsui (2002).

A principal alteração hidrotermal associada a esse grupo de depósitos minerais é a carbonatação, sericitização e piritização, contendo assinatura geoquímica com a presença de elementos como Au, Ag, W, B, ± As, Mo, Bi, Pb, Sb, Te, W, Zn. Costumam formar depósitos de 1 a 10 milhões de toneladas de minério a 5-10 g/t Au, contendo 25-100 toneladas de Au. Além disso, esse tipo de depósito possui idades entre Arqueano médio e Terciário (Groves *et al.,* 2003), grau metamórfico entre xistos verdes inferior a granulito, com mineralização tardi-tectônica a sin ou pós pico metamórfico, com temperatura e pressão de formação entre (200º-650ºC, 0.5-5 kbars) e fluídos de baixa salinidade (H2O-CO2 ± CH4 ± N2). Outros diagramas de classificação também foram elaborados por Groves *et al.* (1998), Hagemann *e* Cassidy (2000) e Bierlein e Crowe (2000).

1.3.2. A Província Tocantins e os *greenstone belts* de Goiás

A Província Tocantins (Almeida *et al*., 1977), localizada a oeste do Cráton São Francisco, engloba as faixas Araguaia, Brasília, Paraguai e Arco Magmático de Goiás e Maciço de Goiás. A região oriental da Província Tocantins foi subdividida (Fuck et al., 1993; Fuck, 1994) nos seguintes compartimentos tectônicos: Zona

Cratônica, Faixa Brasília – Zona Externa, Faixa Brasília – Zona Interna, Maciço de Goiás e Arco Magmático do Oeste de Goiás. A área de estudo situa-se no domínio do Maciço de Goiás (Figura 2).

O Maciço de Goiás (Barbosa *et al.*, 1969) é composto por terrenos granito-*greenstone belts* de idade arqueana, complexos máficos-ultramáficos e sequências vulcano-sedimentares de idade paleo-mesoproterozoicas. As rochas de idade paleo-mesoproterozoica consistem dos complexos máficos-ultramáficos de Barro Alto, Niquelândia e Canabrava além das sequências vulcano-sedimentares de Jucelândia, Coitezeiro e Palmeirópolis. Em relação aos terrenos arqueanos no Maciço de Goiás (Figura 2), eles representam associações de complexos granito-gnáissicos e *greenstone belts* orientados NE-SW com limites inteiramente tectônicos. A norte e oeste estão limitados com o Arco Magmático de Goiás representado por rochas metavulcânicas, metassedimentares e gnáissicas de idade neoproterozóica. Ao sul e a nordeste estão limitados pela faixa de rochas metassedimentares e metavulcânicas do paleoproterozoico da região de Mossâmedes (Pimentel *et al.,* 2000). Ao leste e nordeste limitam-se com as rochas metassedimentares do grupo Araxá.
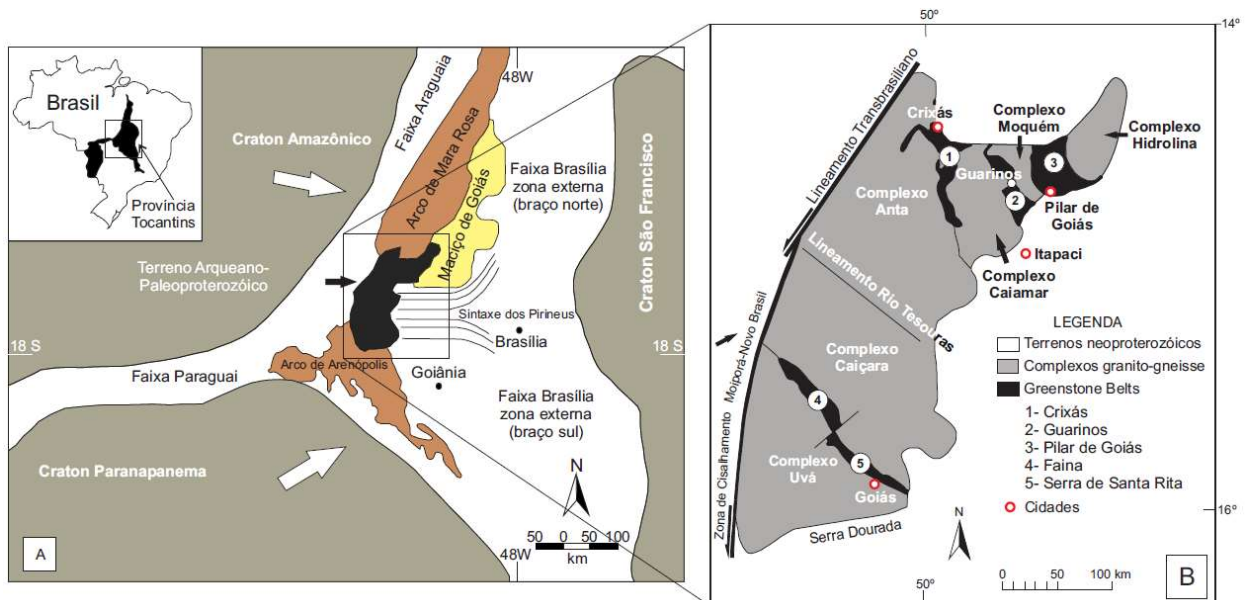

Figura 2. a) Geologia da área de estudo em escala continental. b) Localização dos terrenos arqueanos do Brasil central. Modificado de Pimentel *et al.* (2000).

Os terrenos granito-gnáissicos compreendem cerca de 80% do segmento crustal arqueano e são constituídos de gnaisses e intrusões de granitóides de composição tonalítica a granodiorítica, raramente granítica. Esses terrenos foram reunidos em cinco complexos: Anta (Vargas, 1992), Caiamar (Jost *et al.*, 1994a; Jost, 2001), Caiçara (Oliveira, 1983), Hidrolina e Uvá (Resende, 1999; Resende *et al.*, 1998) e o bloco Moquém (Dani & Ribeiro, 1978; Vargas, 1992; Jost *et al.*, 1994b).

Os terrenos *greenstone belts* compreendem 20% do segmento crustal arqueano e são subdivididos em cinco faixas de 6 km de largura e 40 a 100 km de comprimento cada. As faixas de Crixás (Sabóia & Teixeira, 1980), Guarinos (Jost & Oliveira, 1991) e Pilar de Goiás (Jost & Oliveira, 1991) situam-se no extremo norte enquanto que as faixas de Faina (Resende *et al.*, 1998) e Santa Rita (Resende *et al.*, 1998) situam-se no extremo sul (Figura 2). Queiroz (2000) criou um quadro comparativo (Quadro I) da estratigrafia dos *greenstone belts* de Crixás, Guarinos, Pilar de Goiás, Santa Rita e Faina.

Quadro I. Quadro comparativo da estratigrafia dos *greenstone belts* de Crixás, Guarinos, Pilar de Goiás, Santa Rita e Faina. Modificado de Queiroz (2000).

Greenstone belt (GB)		Litotipos			
		Vulcânicas Ultramáficas	Vulcânicas Máficas	Vulcânicas Félsicas	Sedimentar
Porção Norte	GB de Crixás	Formação Córrego Alagadinho	Formação Rio Vermelho		Formação Ribeirão das Antas
	GB de Guarinos	Formação Serra do Cotovelo	Formação Serra Azul		Formações São Patricinho, Aimbé e Cabaçal
	GB de Pilar de Goiás	Formação Córrego Fundo	Formação Credolina		Formações Boqueirão e Serra do Moinho
Porção Sul	GB de Santa Rita	Formação Manoel Leocádio	Formação Digo-Digo	Membro Superior	Formações Fazenda Limeira e Fazenda Cruzeiro
	GB de Faina	Formação Manoel Leocádio	Formação Digo-Digo		Formações Fazenda Tanque, Serra São José e Córrego Tatu

1.3.3. O *greenstone belt* de Crixás e seus depósitos auríferos

O *greenstone belt* de Crixás (Figura 3) caracteriza-se como uma sequência vulcano-sedimentar, denominada Grupo Crixás por Jost e Oliveira (1991), alongada segundo a direção N-NW e S-SE, limitado ao sul e ao leste pelo Complexo Caiamar,

a oeste pelo Complexo Anta e a norte por rochas da Sequência Mina Inglesa e metassedimentos do neoproterozoico da Sequência Santa Terezinha (Jost, 2001; Dantas *et al*., 2001). Constitui uma faixa alongada com aproximadamente 45 km de comprimento e 6 km de largura (Pimentel *et al*., 2000). O Grupo Crixás foi caracterizado por Sabóia *et al*. (1981), da base para o topo, por rochas ultramáficas komatiíticas (Formação Córrego Alagadinho), basaltos almofadados e vesiculados (Formação Rio Vermelho) e por uma sequência de sedimentos químicos e detríticos no topo (Formação Ribeirão das Antas). As espessuras aproximadas são de 500m, 350m e 700m, respectivamente. Theodoro (1995) subdividiu a Formação Ribeirão das Antas em Membro Vulcanossedimentar, Membro Carbonático e Membro Siliciclástico.
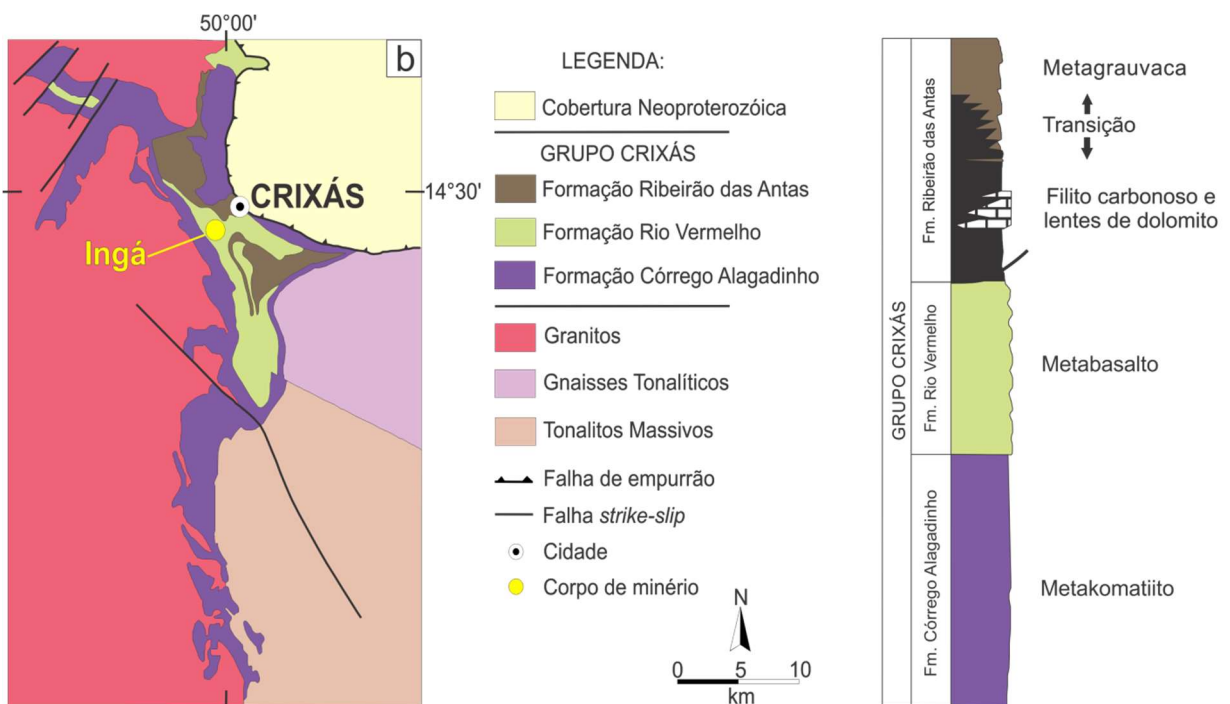
Figura 3. a) Esquema geológico simplificado do greenstone belt de Crixás. Modificado de Jost e Fortes (2001). b) Coluna estratigráfica do greenstone belt de Crixás. Modificado de Jost et al. (2010).

O *greenstone belt* de Crixás é caracterizado por grande complexidade estrutural como resultado de vários ciclos tecto-orogenéticos, sendo possível identificar uma fase de distensão durante a formação do *greenstone belt*, acompanhada de quatro eventos deformacionais posteriores, compressivos. A sequência de eventos compressivos, descrita por Massucato (2004) e Carvalho (2005), possui forte ligação com a mineralização aurífera. Carvalho (2005)

descreveu a existência de três eventos deformacionais (D1, D2 e D3) no *greenstone belt* de Crixás, assim como Massucato (2004), que levantou a hipótese de mais um evento (D4). Já Yamaoka e Araújo (1988) observaram a inversão estratigráfica das sequências na Mina III do greenstone belt de Crixás.

O metamorfismo é heterogêneo, assim como a deformação, desde condições de xisto verde até a fácies anfibolito inferior (Massucatto, 2004). O modelo epigenético, atribuído aos depósitos de ouro da região de Crixás, mostra-se consistente com as interpretações de depósitos de ouro de terrenos arqueanos (Jost, 2001), definidas por Phillips e Groves (1983) e aprimoradas por Foster *et al.* (1986), Groves *et al.* (1987), Colvine *et al.* (1988), Colvine (1989) e Groves e Foster (1991).

Os dados mais recentes de datação geocronológica (Jost *et al.,* 2010) têm apontado que a mineralização aurífera é restrita ao Rhyaciano (Paleoproterozoico), através de datação de zircões magmáticos de diques máficos pós-mineralização que indicaram idade U-Pb de 2170 ± 17 Ma (Jost *et al.*, 2010). Jost *et al.* (2010) também sugere que o estágio basinal, deformação, metamorfismo e mineralização ocorreram em um intervalo de tempo de 30-40 Ma restrito ao mesmo período (2,2 a 2,17 Ma). O mesmo trabalho ainda sugere que a carga sedimentar da área fonte para as metagrauvacas e filitos carbonosos da Formação Córrego Alagadinho possui idade (U-Pb de 3354 ± 40 Ma a 2209 ± 28 Ma) entre o arqueano e o paleoprotezoico (Rhyaciano) com idade deposicional máxima de 2,2 Ga. A idade dos metabasaltos da Fm. Rio Vermelho e metakomatiitos da Fm. Córrego Alagadinho são sugeridas como arqueanas por Arndt *et al.* (1989) e Fortes *et al.* (2003), mas Jost *et al.* (2010) indicou idade paleoproterozoica (idades modelo Nd 2,32 Ga e 2,24 Ga).

No *greenstone belt* de Crixás encontram-se as principais mineralizações auríferas da região (Tabela 1 e Figura 4), controladas por falhas transcorrentes e de empurrão (Jost & Fortes 2001), de modo que três tipos diferentes de mineralização foram reconhecidos: (1) Sulfeto maciço, (2) Veio de quartzo e (3) Sulfeto disseminado. Os corpos de minério podem ser divididos de acordo com a falha de empurrão principal que o controla, chamada de "estrutura": Estrutura Palmeiras (corpos Palmeiras e Baru), Estrutura IV (corpos Pequizão, Forquilha, Corpo IV, Corpo V e Sucupira), Zona Superior (Mina III e Ingá) e Estrutura III (Mina III, Mina Nova e Ingá).

Tabela 1. Principais estruturas (falhas de empurrão), corpos de minério e estilos de mineralização do depósito de ouro de Serra Grande.

Cor	Estrutura (falha de empurrão)	Corpos de minério	Estilos de mineralização
🟩	Palmeiras	Palmeiras, Baru	SM, SD, VQ
🟥	Estrutura IV	Corpo IV, Corpo V, Forquilha, Pequizão, Sucupira	SD, VQ
🟦	Estrutura III Zona Superior	Mina III, Ingá	SM
🟨	Estrutura III Zona Inferior	Mina III, Ingá, Mina Nova	VQ, SD

Obs: SD = Sulfeto disseminado, SM = Sulfeto maciço, VQ = Veio de quartzo.

1.3.4. A estrutura III e o corpo de minério Ingá

Na chamada "Estrutura III", ocorrem os corpos de minério Mina III, Mina Nova e Ingá. Yamaoka e Araújo (1988) dividiram o corpo de minério Mina III em quatro zonas: superior, intermediária, inferior e zona da granada. Na zona superior a mineralização ocorre na forma de lentes de sulfeto maciço hospedados em mármore dolomítico, quartzo-clorita-carbonato-sericita xistos, pirrotita-magnetita-biotita xistos, clorita-granada xistos, granaditos, muscovita xistos, muscovita-clorita xistos e biotita mármores (Jost & Fortes 2001). O ouro ocorre em associação com arsenopirita, pirrotita, calcopirita, carbonatos, quartzo, micas e óxidos. Na zona intermediária ocorre a zona da granada associada, além de um veio de quartzo concordante hospedado em quartzo-clorita-muscovita-granada xisto. O ouro ocorre em associação com quartzo, micas, arsenopirita, calcopirita e óxidos. A zona inferior da Mina III, similar à zona inferior do corpo de minério Ingá, possui veio de quartzo encaixado em filito carbonoso com arsenopirita e pirrotita disseminadas próximas ao veio (Jost & Fortes 2001). O ouro associa-se com quartzo, material carbonoso e arsenopirita. As rochas hospedeiras apresentam alteração hidrotermal do tipo silicificação, carbonatação, fílica e sulfetação e encontram-se deformadas e metamorfisadas na fácies epidoto-anfibolito (Fortes et al. 1997).

O corpo de minério Mina Nova está hospedado em filitos carbonosos deformados por cisalhamento e compreende três tipos de minério (Portocarrero, 1996): Tipo I, Tipo II, Tipo III. O tipo I consiste de filito carbonoso com disseminações de pirrotita, arsenopirita e calcopirita. O tipo II consiste de sericita carbonato xisto com arsenopirita, pirrotita e calcopirita e o tipo III possui arsenopirita disseminada em venulações de quartzo hospedadas em filito carbonoso. Além disso, a Mina Nova também apresenta as seguintes litologias: anfibólio xistos, mármores, quartzo-clorita-carbonato-sericita xistos, quartzo-clorita-sericita-granada xistos e xistos feldspáticos. A mineralização do tipo minério disseminado é a principal forma de ocorrência do ouro no corpo de minério Mina Nova.

O corpo de minério Ingá possui mergulho da mineralização para NW, contendo subcorpos com espessuras que variam de 1 a 3 metros e comprimento entre 350 e 900 metros ao longo do mergulho (Silva, 2014). O corpo Ingá é dividido em duas zonas mineralizadas distintas: Superior e Inferior. Na Zona Superior a mineralização ocorre na forma de lentes de sulfeto maciço hospedado em dolomitos e na Zona Inferior, objeto de estudo deste trabalho, a mineralização aurífera ocorre associada a um espesso veio de quartzo e ao filito carbonoso adjacente ao veio. A zona inferior do corpo de minério Ingá foi estudada em detalhe anteriormente pelo presente autor (Castoldi, 2015), cujos dados também são apresentados na presente dissertação e manuscrito submetido a periódico.

2. ARTIGO

Esta seção consiste do artigo científico produzido pelo autor durante o desenvolvimento de seu Mestrado, submetido à revista Economic Geology, com respectiva carta de submissão.

Geology and Geochemistry of the Ingá Orebody Lower Zone, Crixás Gold District, Goiás, Brazil: Implications for Genesis and Exploration

Marco A. S. Castoldi[1,2,†], José C. Frantz[2], Juliana C. Marques[2], Bruno A. dos Santos[3], Renan G. de Souza[2]

[1] *AngloGold Ashanti Córrego do Sítio Mineração, Nova Lima, MG Brazil, 34000-000*

[2] *Departament of Geology, Universidade Federal do Rio Grande do Sul, Porto Alegre, RS Brazil, 91501-970*

[3] *AngloGold Ashanti Mineração Serra Grande, Crixás, GO Brazil, 76510-000*

Abstract

The Ingá orebody was discovered in 2012 and is located in the world-class AngloGold Ashanti – Serra Grande Unit of the Crixás Gold District, Central Brazil. Located in the supracrustal rocks, Ingá is divided into Upper and Lower Zones. The Upper Zone contains massive sulfide lenses hosted in dolomites. The Lower Zone was systematically studied by XRD, XRF, ICP-MS, EMP and LA-ICP-MS. It is controlled by a major low angle thrust fault (Structure III) and lithologies include, from top to bottom: dolomites, carbonaceous phyllite (GXN), major quartz vein (VQZ), quartz-chlorite-sericite-garnet schist, and metagraywacke with two types of rare cross-cutting dikes. Hydrothermal alteration haloes developed outwards from Structure III: silicification, potassic, phyllic and carbonatic. Mineralization occurs in three different stages. Three types of arsenopyrite were identified: Aspy1 (early hydrothermal), Aspy2 (late hydrothermal, possibly invisible gold-rich) and Aspy3 (later hydrothermal, visible gold-rich as inclusions, filling fractures or along its margins). Visible gold also occurs as free crystals in the VQZ basal levels and in the GXN matrix. Possible remobilization of inferred invisible gold in Aspy2 to form visible gold in Aspy3 along late crystal fractures and selective alteration towards the margins occurred as consequence of F2 folding, increasing the orebody gold budget. The Bi ppm x Se ppm and S percent x Bi ppm plots and major gains in As, Ni and Co in the arsenopyrite rich GXN silicification zone could be used to identify potentially gold rich zones. Four prospective parameters were established: VQZ, Aspy2 and Aspy3, accommodation faults, and silicification zone.

Introduction

Correctly understanding mineral occurrence controls is a major concern for brownfields and greenfields exploration efforts worldwide. In the Crixás greenstone belt terrane (18.73 Moz Au), in the Goiás Massif (southern portion of Tocantins Province), gold orebodies are stacked in a metamorphosed volcano-sedimentary stratigraphic sequence. The three types of gold mineralization present in the world-class Crixás Gold District (quartz-vein, disseminated, and massive sulfide) have key microscale characteristics that have to be considered in exploration efforts: arsenopyrite with or without visible gold inclusions (with possible remobilization) and visible/invisible gold within bands

of the major quartz veins. Analytical interpretation at the microscale must then be completed to develop reliable macroscale prospective parameters for exploration teams.

World-class AngloGold Ashanti – Serra Grande Unit in the Crixás Gold District, part of the Crixás greenstone belt terrane, is the fourth largest gold deposit currently in operation in Brazil in regard to production. More than 23.2 Mt of ore at 5.97 g/t Au (4.19 Moz of Au) have already been extracted from the beginning of its production in 1986 to 2017. Reserves and global resources as of December 31th, 2017 were 6.68 Moz Au from more than 50.67 Mt at an average grade of 4.10 g/t Au. The gold distribution at the Crixás Gold District is controlled by thrust faults and spatially organized in many different orebodies. The Ingá orebody is divided into Upper and Lower Zones and contains 0.59 Moz Au from more than 3.14 Mt at an average grade of 5.91 g/t Au, as of December 31th, 2017. The present study focuses on the Lower Zone of the orebody. Ingá orebody is an important segment of the Crixás Gold District and its study presents an opportunity to contribute to exploration in the area.

Mapping, petrography, and whole rock analysis of wall rocks and hydrothermal zones provide the geochemical signature for major and trace elements within orebodies (Barrett et al., 1998; Dube et al., 2007; Wilkinson et al., 2015; Gregory et al., 2016; Lebrun et al., 2017). Furthermore, X-ray diffraction (XRD), scanning electron microscope (SEM) and electron microprobe (EMP) are used extensively to identify hydrothermal alteration haloes and minerals (e.g. Dube et al., 2007; Duuring et al., 2016; Lebrun et al., 2017). Backscattering imaging (BSE) in SEM, EMP, and LA-ICP-MS element mapping in Au bearing arsenopyrite may reveal crystal element zoning and gold remobilization (Large et al., 2007, 2009; Morey et al., 2008; Ciobanu et al., 2012; Cook et al., 2013; Hazarika et al., 2013; Lawley et al., 2015; Steadman and Large, 2016; Rottier et al., 2016). Through mapping, hand and drill hole sampling, petrographic microscope, XRD, whole rock geochemical analysis, SEM, EMP, LA-ICP-MS, and modelling, the main objectives of this paper are: (1) petrographic and geochemical characterization of the host rocks, hydrothermal alteration haloes and mineralization; (2) geochemical explanation of the arsenopyrite-gold bearing association; (3) explain the genesis of the Ingá orebody; (4) explain the concentration of gold in the major quartz vein; (5) establish prospective parameters for the industry.

Geologic Setting

Regional Geology

The Crixás Gold District (lat 14º34'25" S, long 49°58'04" W), in the Crixás greenstone belt terrane, is located in the Goiás Massif (Fig. 1A), in the southern portion of the Tocantins Province (Almeida et al., 1977; Fuck et al. 1993; Fuck, 1994), which is composed of archean-paleoproterozoic granite-gneiss and greenstone belt terranes, mafic-ultramafic complexes, and volcano-sedimentary sequences (Barbosa et al., 1969; Pimentel et al., 2000). The greenstone belts terrains are divided into five sub-terrains (Fig. 1B) of 6 km width and 40 to 100 km length: Crixás (Sabóia and Teixeira, 1980),

Guarinos, and Pilar de Goiás (Jost and Oliveira, 1991) to the north and Faina and Santa Rita to the south (Resende et al., 1998).

The Crixás greenstone belt is a volcano-sedimentary sequence (Jost and Oliveira, 1991) elongated in the N-NW and S-SE directions with 6 km width and 45 km in length and are composed, from base to top, (Sabóia et al., 1981) by: komatiitic ultramafic rocks (Córrego Alagadinho Formation), vesiculated and pillowed basalts (Rio Vermelho Formation) and a sequence of detrical and chemical sediments (Ribeirão das Antas Formation). The average thicknesses are 500 m, 350 m, and 700 m, respectively. The Ribeirão das Antas formation is subdivided into a volcano-sedimentary member, carbonatic member, and siliciclastic member (Theodoro et al., 1995). Structural complexity in the greenstone is inferrered to be the result of an extensional phase during its formation, followed by later compressive deformation (Carvalho, 2005). The Crixás greenstone belt is limited by two TTGs complexes: the Caiamar to the south and east, and the Anta to the west, and by the metasedimentary sequences of Mina Inglesa and Santa Terezinha to the north.
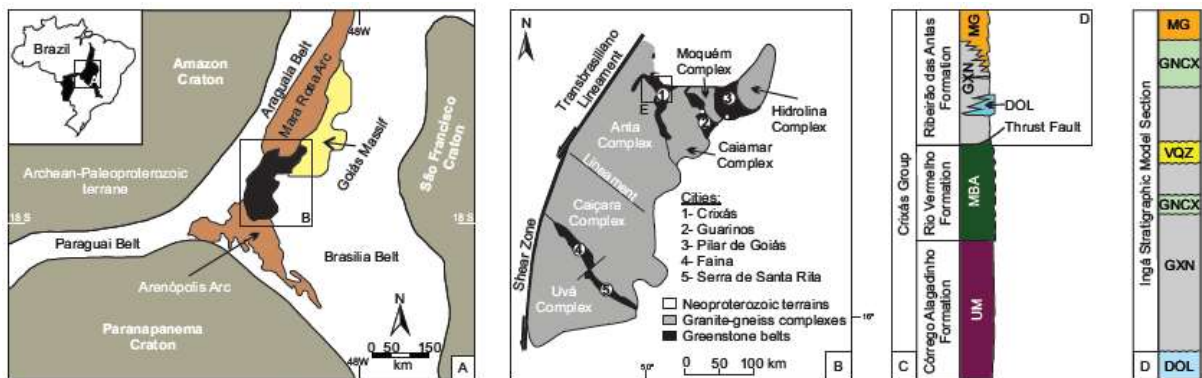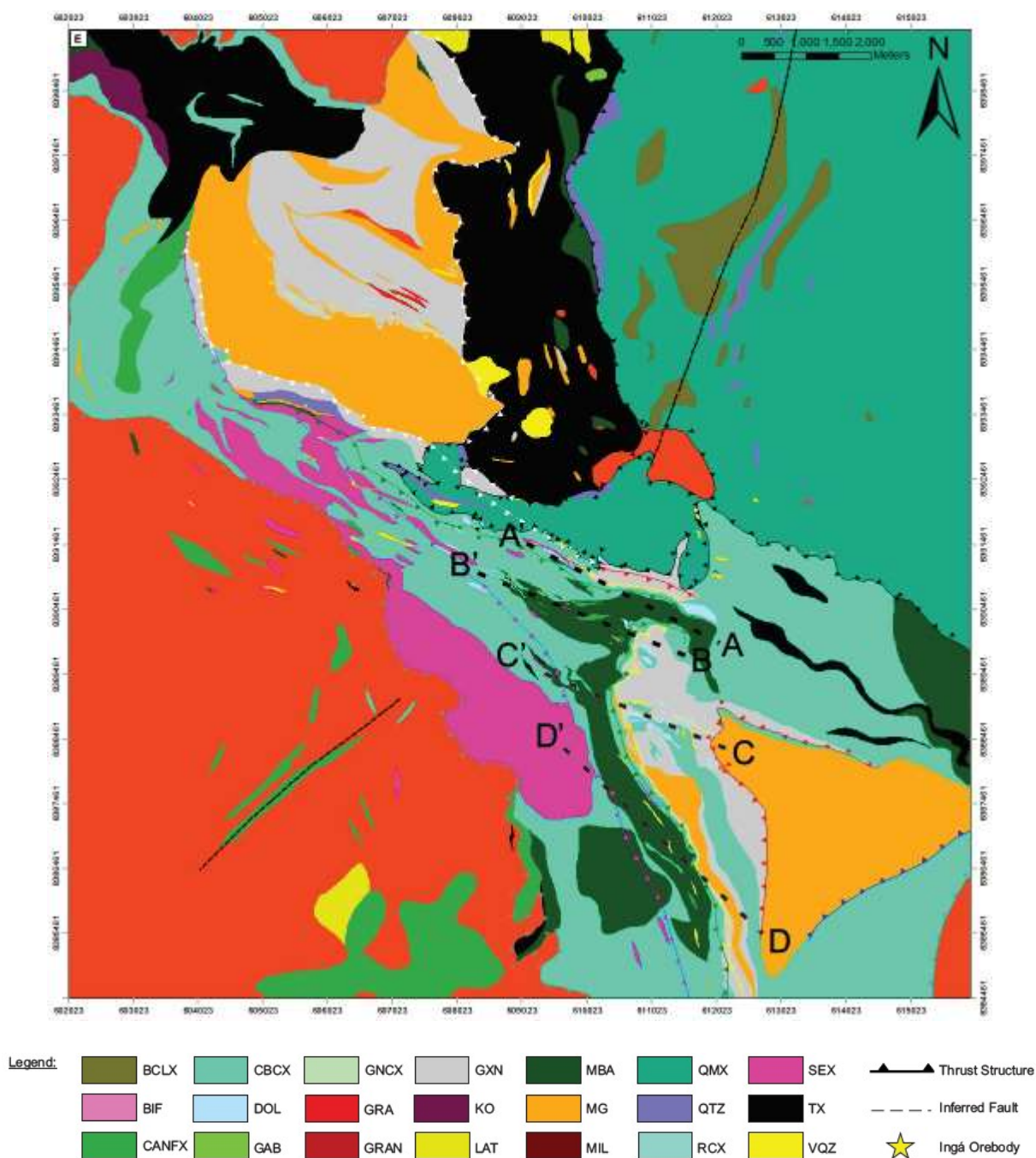
Fig. 1. A) Geology of the study area in continental scale with location. Grid coordinates: Lat/Long. Redrawn from Pimentel et al., 2000. B) Location of central Brazilian archean terranes. Grid coordinates: Lat/Long. Redrawn from Pimentel et al., 2000. C) Crixás greenstone belt stratigraphy. Redrawn from Jost and Oliveira, 1991 and Resende et al., 1998. D) Ingá orebody pre-stratigraphic overturning. E) Crixás greenstone belt geological map produced by the Serra Grande Exploration Team, scale 1:50,000 with location of sections related to Figure 2. Grid coordinates: UTM. Abbreviations: BCLX = Biotite-chlorite schist, BIF = Banded iron formation, CANFX = Amphibole schist, CBCX = Quartz-chlorite-carbonate-sericite schist, DOL = Dolomite, GAB = Gabbro Norite, GNCX = Quartz-chlorite-sericite-garnet schist, GRA = Granite, GRAN = Granatite, GXN = Carbonaceous phyllite, KO = Komatiite, LAT = Laterite, MBA = Metabasalt, MG = Metagraywacke, MIL = Mylonite, QMX = Quartz-mica schist, QTZ = Quartzite, RCX = Roscoelite schist, SEX = Sericite-chlorite schist, TX = Talc-schist, VQZ = Quartz vein.

The installation of the Crixás greenstone belt started with komatiite followed by toleiitic spills originating a flexural basin with deposition of carbonaceous phyllite and metagraywacke, characterizing a proximal shallow sea platform setting. The Córrego Alagadinho Formation is

composed of metakomatiites with spinifex texture, olivine cumulates, flux breccia, polyhedral disjunctions, and partial or total serpentinization (Sabóia 1979). The Rio Vermelho Formation is in abrupt contact with the Córrego Alagadinho Formation and has toleitic basalts, amphibolites, amphibole schists, and komatiitic metabasalts with primary features including: pillows, varioles, vesicles and orbicules locally preserved (Sabóia 1979). Banded iron formations, magnesiferous formations, and metachert occur as metasedimentary intercalations (Jost and Fortes 2001). The Ribeirão das Antas Formation occurs in transitional contact with the Rio Vermelho Formation and is composed of carbonaceous phyllite with lenses and beds of dolomites superimposed abruptly by siliciclastic metarritimites. Theodoro (1995) divided the Ribeirão das Antas Formation into three members: (1) volcano-sedimentary; (2) carbonatic; (3) siliciclastic.

Structural data obtained by Magalhães (1991), Queiroz (1995), and referred to in unpublished reports by the staff of the mining company attest that the supracrustal rocks of Crixás underwent four major deformational events: D1, D2, D3, and D4. An east-west compression with vergence to the east followed and formed a N-S low-angle thrust fault system, with geometry similar to a duplex. D1 is responsible for the formation of regional, tight to isoclinal, probably upright folds with an axial surface represented by a metamorphic foliation (S1) that is pervasive in the metasedimentary sequence. Thrust faults generated metric ruptile-ductile shear zones in which the hydrothermal fluids took advantage as preferential pathways. The main hydrothermal event occurred during D1 (syn-mineralization). Hydrothermal activity formed the major quartz-vein mineralization type observed in the Structure III Lower Zone orebodies, including Ingá.

The D2 event is N-S compressive, promoting the horsening of the Santa Teresinha Sequence above the Crixás group rocks (stratigraphic overturning), which generated F2 folds, S2 plan-axial cleavage, and L2 stretching lineation. Metakomatiites override metabasalts which are overridden by the metasedimentary section, during stratigraphic overturning in D2. Thin-skinned thrusting developed a steep ramp to the west and a duplex to the east. The gold mineralization and associated hydrothermal alteration haloes are hosted within the duplex, which indicates that it corresponds to several stacked dilation zones interpreted as second-order thrust faults related to a major, shallowly dipping, first-order detachment fault (Jost et al., 2010). The F2 folds, in general, structurally control the mineralization plunge in the district because of D2 compression on S1 foliation, which possibly promotes remobilization. Mineralization plunge is usually parallel to F2 fold axis. These folds are recumbent to semi-recumbent, dominantly south-vergent with south westerly dips and a weakly to moderately developed axial plane foliation. L2 stretching lineations that formed by intersection of S2 with S1 planes also mark the mineralization plunge. Thrust faulting due to F2 can be generated, being the cause for local gold remobilization.

The D3 event involved an E-W compression, which resulted in large scale N-S folding, promoting the formation of post-mineralization crenulation cleavage (S3). The D3 event formed the

Rio Vermelho Antiform (Magalhães, 1991), folding the duplex system that formed during D1 (Carvalho, 2005). Neoproterozoic Mara Rosa Magmatic Arc rocks override the northern limit of the greenstone belt. Minor structures of this event comprise SW-verging, semi-recumbent to recumbent folds. The D3 event is also responsible for gold remobilization and reshaping of the orebodies to an overall 25º/N65ºW plunge, as well as for partial recrystallization of the hydrothermal alteration envelopes of some of the orebodies (Jost et al., 2010). The post-mineralization D4 event was NNW-SSE to N-S compressive, forming kink bands, smooth folding, and crenulation cleavage (S4), without influencing the orebody geometry and gold distribution. Metamorphism of the rocks ranges from greenschist to lower amphibolite facies (Jost et al., 2010). The Crixás Gold District then comprises a thrust stack of seven or more major thrust sheets, separated by either discrete thrust planes or (more commonly), complex thrust zones comprising both locally imbricated thrusts and/or high strain zones including several primary and altered lithologies (L.R. Rankin, pers. commun., 2004).

Table 1. Summary of the Main Structural Fabrics Recognized in the Crixás Gold District.

Event	Elements	Description	Distribution	Kinematics (in respect to present coordinates)	Effects on the ore zones nature and geometry
NA	S0	Original bedding	Low strain zones	NA	None
D1	S1	Pervasive fabric (metamorphic schistosity)	Occur preferentially in ruptile-ductile shear zones related to low-angle thrust faults. Affects the metassedimentary sequence pervasively	E-W compression with vergence to E	Reorientation and generation of micas. Mimetized. Main hidrotermalization of the rocks. Main sulphidation event. Entrance of gold in the system.
D1	L1	Mineral and streching lineation	Locally	NW-SE plunging	Streching/growing/reorientation of quartz, arsenopyrite, amphiboles and ore minerals.
D2	S2	Plane-axial cleavage (pressure dissolution)	Throughout the deposit, affected all rocks	N-S compression, W dipping	Reorientation of micas, transposition of foliation S1 and/or S0. Horsening of Santa Teresinha sequence over Crixás GB. Overturning of the stratigraphic sequence.
D2	F2	Folding	Throughout the deposit, affected all rocks, mainly carbonaceous schist and metagraywacke	SW vergence, NW-SE trending	Reconcentration of gold in fold hinges, parallel to F2 axis, representing the mineralization plunge. Possible remobilization of gold in arsenopyrite. Folding of S1∥S0 parallel to mineralization.
D2	L2	Stretching lineation	Locally	NW plunging	Intersection of S2 with S1 giving the mineralization plunge.
D3	S3	Crenulation cleavage	Throughout the deposit, affected all rocks	E-W compression	Reorientation of micas, locally form chevron or kink folds. Arquing of Crixás GB, originating the Rio Vermelho Antiform. Gently rotate F2 axis. Possible gold remobilization and reshaping of the orebodies to a $25°/N65°W$ plunge. Partial recrystallization of the hydrothermal alteration envelopes of some orebodies.
D4	S4	Crenulation cleavage	Throughout the deposit, affected all rocks	NNW-SSE to N-S compression	Undulation of the greenstone belt. No influence on the orebodies.

Notes: NA = do not apply

Geochronological data suggest that gold mineralization is restricted to the Rhyacian (Paleoproterozoic). Magmatic zircons from post-mineralization mafic dikes dated by U-Pb indicate 2170 ± 17 Ma (Jost et al., 2010). The basinal stage, deformation, metamorphism, and mineralization, according to Jost et al. (2010), occurred in a 30-40 Ma range of time restricted to the Rhyacian 2.2 to 2.17 Ma. The source sediments that were metamorphosed to carbonaceous phyllite and metagraywacke have U-Pb dating of 3354 ± 40 Ma to 2209 ± 28 Ma, with a maximum depositional age of 2.2 Ga. The model ages of metabasalts of the Rio Vermelho Formation and metakomatiites of the Córrego Alagadinho Formation are Nd 2.32 Ga and 2.24 Ga, respectively (Jost et al., 2010; Fortes et al., 2003).

Deposit Geology

The main auriferous mineralizations of the region occur in the Crixás greenstone belt and are controlled by thrust and transcurrent faults (Jost and Fortes, 2001). The area is within the AngloGold Ashanti - Serra Grande Unit and the Cleveland Mining Company LTD - Premier Gold Project (Fig. 1E). Three different types of gold mineralization are known: (1) Massive sulfide; (2) Quartz-vein; (3) Disseminated sulfide (Table 2).

The massive type consists of lenses of massive sulfide concordant with S1 parallel to S2 and occurring near the contact between metabasalts and BIF of Rio Vermelho Formation or inside the dolomite layers crosscutting the stratigraphic sequence (Fortes, 1996). These lenses have 95% Po-Aspy, with subordinated magnetite, ilmenite, and chalcopyrite and are 0.5–2.5 m in width and 50-400 m in length. The gold occurs in the massive Aspy crystals.

Table 2. Main Thrust Fault Structures, Orebodies and Mineralization Styles.

Colors	Thrust Fault Structures	Orebodies	Mineralization Styles
(green)	Palmeiras	Palmeiras, Baru	MS, DS, QV
(red)	Structure IV	Corpo IV, Corpo V, Forquilha, Pequizão, Sucupira	DS, QV
(blue)	Structure III Upper Zone	Mina III, Ingá	MS
(yellow)	Structure III Lower Zone	Mina III, Ingá, Mina Nova	QV, DS

Notes: DS = Disseminated sulfide, MS = Massiva sulfide, QV = Quartz vein
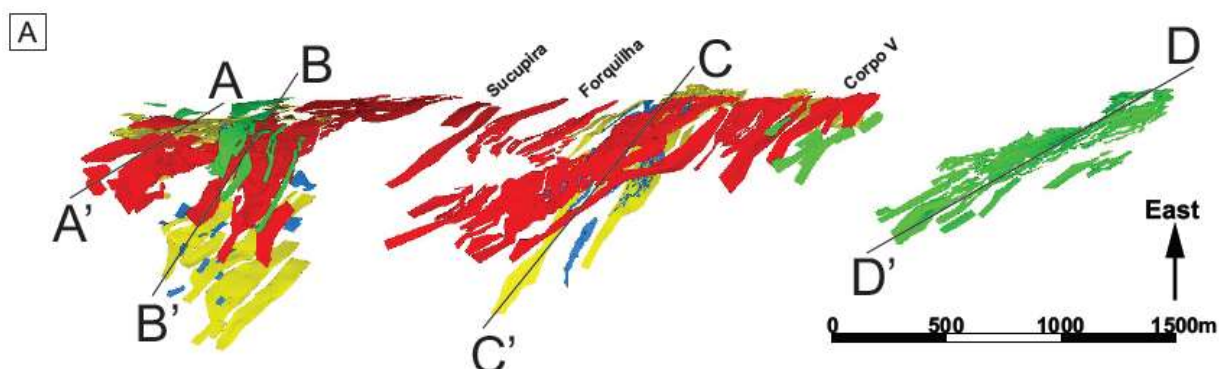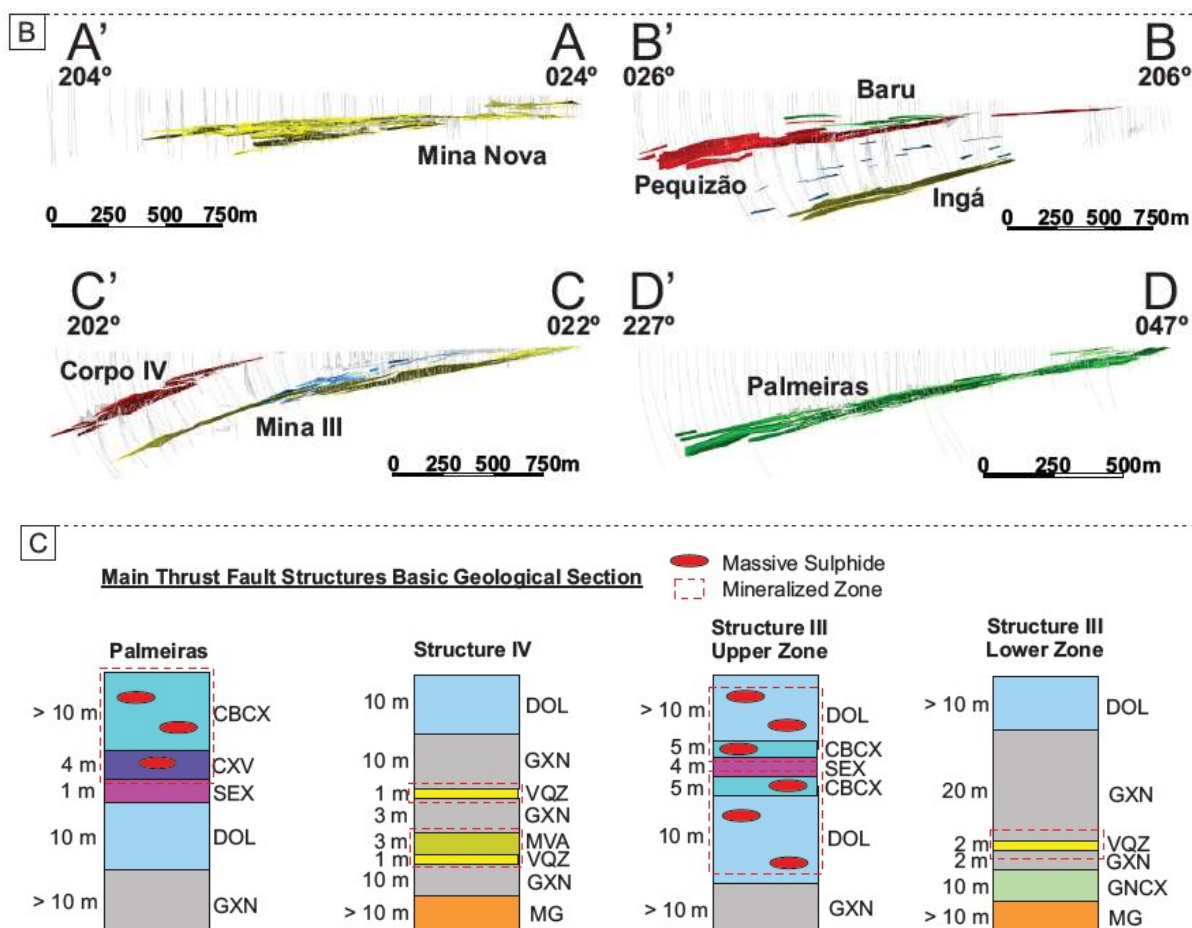
Fig. 2. A) Spatial distribution of the main orebodies from Crixás Gold District at AngloGold Ashanti – Serra Grande Unit. For section locations see Figure 1. Drill hole trace lines are in light gray. B) Cross sections showing approximately the position of the main orebodies in the area. See Ingá orebody at section B-B' along the Structure III Lower Zone. C) Basic geological section of main thrust fault structures. Legend of colors: green (Palmeiras Structure), red (Structure IV), blue (Structure III Upper Zone) and yellow (Structure III Lower Zone). Abbreviations: CBCX = Quartz-Chlorite-Carbonate-Sericite Schist; CXV = Chlorite-Anfibole-Carbonate Schist; DOL = Dolomite; GNCX = Quartz-Chlorite-Sericite-Garnet Schist; GXN = Carbonaceous Schist; MG = Metagraywacke; MVA = Acid Metavolcanic; SEX = Sericite-Chlorite Schist; VQZ = Quartz Vein. Lenses of the above lithologies may crosscut the sequences in different levels with variable thickness.

The quartz-vein type is discontinuous and concordant with the S1 parallel to S2, having 0.5-5.0 m width and 500-1500 m length. It occurs in the carbonaceous phyllite of the Ribeirão das Antas Formation. and has 98% recrystallized milk-quartz with disseminationed Po, Aspy, Mca, carbonaceous matter, plagioclase, carbonate, and chlorite. The gold occurs as free crystals in the quartz vein, with the highest concentrations occurring up to 1.5 m from the footwall of the vein, inwards. The disseminated sulfide mineralization type consists of zones with 1-5 m in width and 200-1000 m in length, in the Ribeirão das Antas Formation carbonaceous phyllite. The gold occurs in the carbonaceous phyllite Aspy, as free crystals in quartz-veining, or in the carbonaceous phyllite gangue minerals (i.e. titanite and biotite). Other sulfide minerals are Cpy, Py, Po, and Pentlandite. The orebodies at the Crixás Gold District are classified according to the main thrust fault that controls them, named "structures", which included, stacked from top to bottom (Table 2 and Fig. 2): Structure Palmeiras (Palmeiras and Baru orebodies), Structure IV (Pequizão, Forquilha, Corpo IV, Corpo V, and

Sucupira orebodies), Structure III Upper Zone (Mina III and Ingá orebodies) and Structure III Lower Zone (Mina III, Mina Nova, and Ingá orebodies).

The present study focus on the quartz-vein and disseminated mineralization in the Ingá orebody Lower Zone (Structure III). The Mina III Lower Zone and Mina Nova orebodies are hosted at the same stratigraphic level as the Ingá orebody Lower Zone in the Ribeirão das Antas Formation, showing similarities between them. This stratigraphic level has the highest gold grades in the district. The Mina III started production in 1986 and is the richest orebody in the region, with 1,0 Moz Au from more than 6,86 Mt at an average grade of 4.53 g/t Au as of December 31th, 2017. Yamaoka and Araújo (1988) divided the Mina III orebody into four zones: upper, intermediate, lower, and garnet zone. The Mina III Lower Zone has major quartz-veins crosscutting carbonaceous phyllite, with arsenopyrite and pyrite disseminated close to the vein (Jost and Fortes, 2001). Gold crystals are associated with quartz, carbonaceous matter, and arsenopyrite. The host rocks present carbonate, sericite, silicification, and sulfide haloes and are metamorphosed and deformed in the epidote-amphibolite facies (Fortes et al., 1997). The Mina Nova has 0.34 Moz Au from more than 6.52 Mt at an average grade of 3.26 g/t Au as of December 31, 2017. The orebody is hosted in carbonaceous phyllite and its mineralization includes: Po, Aspy, and Cpy disseminated in carbonaceous phyllite; Aspy, Po, and Cpy disseminated in sericite-carbonate schist; Aspy disseminated in quartz-veins crosscutting carbonaceous phyllite (Portocarrero, 1996).

The Ingá orebody is divided into Upper and Lower Zones regarding mineralization style. In the Upper Zone the mineralization occurs as massive sulfide lenses hosted in dolomites. In the Lower Zone, the object of this study, the mineralization occurs in association with a thick, discontinuous quartz vein and adjacent carbonaceous phyllite, associated with arsenopyrite, pyrrothite, and subordinated pyrite. The Lower Zone comprises the following host rocks, from top to bottom: brecciated dolomitic marbles, carbonaceous phyllite, quartz-chlorite-sericite-garnet schist, and metagraywackes. Hydrothermal alteration over carbonaceous phyllite adjacent to the thick quartz vein consists of: silicification, phyllic (muscovite) and carbonatic alteration outwards with pods of potassic alteration (biotite). No previous publications and few company reports are available for the Ingá orebody.

Sampling and Analytical Methods

The present contribution reports the study conducted between 2015 and 2018, with data collected in AngloGold Ashanti – Serra Grande Unit and the Universidade Federal do Rio Grande do Sul (UFRGS). Two hundred and eighty meters of four drill holes selected in a 203-023° section perpendicular to the Ingá orebody plunge were geologically described and eighty-two drill core samples were collected. Other fifty-one drill core samples from thirty five drill holes were collected in a 250 x 250 x 250 m grid through the Ingá orebody. Twenty-two hand samples were collected during underground mapping of 112 meters of the Ingá orebody´s 730N galleries with a 1:100 scale and 3 m

high projection. From the samples collected, sixty-one were selected for petrographic description of polished thin sections under a LEICA DM LP microscope. The sampling approach prioritized different lithotypes, hydrothermal alteration, gold grades, deformation, visual percentage of sulfides and/or visible gold. The drill core described in the study are totally assayed by 30g gold fire assay analysis done on 0.8 – 1.2m samples by AngloGold Ashanti – Serra Grande Unit industrial laboratory, with lower detection limit of 0.025 ppm. Samples for whole-rock analysis were also analyzed by ALS Minerals 30g fire assay with detection limit of 0.005 ppm. Leapfrog Geo 4.2, Reflex IoGAS 6.3.1, ArcGIS 10.1, and Datamine Studio 3 softwares were used for data analysis and modelling.

XRD and Whole-rock Analysis

Twenty samples from a vertical section of drill holes XIGE-0066 and XIGE-0023 were analyzed with XRD. Ten samples were analyzed for whole-rock and clay identification in Weatherford Laboratories (SIEMENS BRUKER AXS D4 Endeavor) in Rio de Janeiro, Brazil with softwares MDI Jade 9+ 2009 and PDF 4+ 2010. Ten samples were analyzed for clay identification in the Diffractometry Laboratory at UFRGS (SIEMENS BRUKER AXS DS5000) in Porto Alegre, Brazil with softwares DIFFRAC – PLUS-EVA and NEWMOD. The database utilized was the ICDD JCPDS. Scanning patterns for whole rock and clay analysis were Cu Kα (0,15406 nm), Kα 2 (0,1544390 nm), 40 Kv, 40 mA, goniometer diameter of 402 mm and variable divergent gap of 1,5 mm for whole rock and 0,75 mm for clay.

Sixty-one samples from thirty-nine drill holes were analyzed for whole rock major and trace element characterization. Fifty-one samples are spaced in a 250 x 250 x 250 grid and ten samples are in a vertical section of four drill holes - both sample sets located through the Ingá orebody. The sampling approach focused on the carbonaceous phyllite and quartz-chlorite-sericite-garnet schist lithologies with background, low, and high gold grades. Analyses were conducted by ALS Minerals in Goiânia and Vespasiano, Brazil (physical preparation) and Lima, Peru (chemical analysis). The physical preparation consisted of weighing, splitting, milling, pulverization to 70% less than 2 mm, splitting, and pulverization to 80% less than 75 μm. The chemical analysis consisted of whole rock analysis by fusion/x-ray fluorescence (XRF), loss on ignition by XRF-WST-SEQ, inductively coupled plasma – mass spectrometry (ICP-MS), total carbon and sulfur measurements by LECO, lithium borate fusion with ICP-MS and four acid digestion of base metals with inductively coupled plasma – atomic emission spectroscopy (ICP-AES).

SEM and EMP Analysis

Twelve thin sections were analyzed by the SEM facility in the UFRGS Isotopic Geology Laboratory equipped with a JEOL JSM-6610LV with energy dispersive spectrometry (EDS) Bruker 133 eV. The focus was the characterization of mineral phases, spot analysis and compositional mapping with semi-quantitative EDS, and textural analysis of gold crystals and sulfides by BSE

imaging. Five thin sections were analyzed for spot, line sections and element mapping with wavelength dispersion spectrometry (WDS) using EMP. Two thin sections had garnet, biotite and chlorite crystals analyzed at the UFRGS Electron Microprobe Laboratory equipped with a Cameca SXFive EMP with operation conditions of 15 keV, 20 nA, 1 μm for garnet, and 15 keV, 15 nA, 10 μm for biotite and chlorite. Four thin sections had arsenopyrite, biotite, muscovite and chlorite crystals analyzed at the Queen's University EMP Laboratory equipped with a JEOL JXA-8230 EMP with operation conditions of 20 keV, 50 nA, and focused beam for arsenopyrite, and 15 keV, 10 nA, and 7 μm for biotite, muscovite and chlorite.

LA-ICP-MS Analysis

One thin section was selected for chemical arsenopyrite analysis by LA-ICP-MS. Three element mapping zones and eighteen spot analyses were obtained on arsenopyrite crystals considering its core, margins, and fractures. Analyses were performed at Queen's University using a 193 nm ArF Excimer laser (Elemental Scientific Lasers NWR193) interfaced with a Thermo Scientific X-Series 2 Quadrupole ICPMS using He as a carrier gas. Laser diameter was set to 10 μm with a scan speed of 5 μm/s and a repetition rate of 30 Hz to ensure the best possible resolution for the maps. Ar (sample gas) and He (carrier gas) flows were optimised on a daily basis for best sensitivity (~10e5 counts/s on 238U for NIST 612 reference glass) while keeping the oxide level as low as possible (<1%). Gas blanks were measured before and after each line for a minimum of 20 seconds. A typical measurement sequence consisted of a block of NIST 614, 612, and 610 reference glasses used to generate individual linear calibrations for all elements, followed by certified reference basalt glass BCR-2G (USGS), the goal of which was to both validate the calibration generated by the NIST glasses and to extend the calibration for elements such as Fe or S (NIST glasses having very similar Fe and S contents). Sulphide pellet reference MASS-1 was run at the end of each set of calibrations to readjust the calibration generated on silicate reference glasses, in order to matrix match the samples. NIST glasses as well as BCR-2G and MASS-1 were run at regular time intervals during the sequences. At the end of each sequence, another complete set of calibrations were generated. Data reduction was performed on Iolite v3.63. The data reduction routine consisted of a gas blank subtraction for each individual line, as well as interpolation between calibrations to correct for any potential drift during the sequence (i.e. instrumental drift of the ICPMS, small variations in laser output, etc). Results files generated on the ICPMS were then combined with the laser logs to generate maps.

Results

Host Rocks and Hydrothermal Alteration

The host rocks at Ingá orebody Lower Zone are metamorphic assemblages with superimposed hydrothermal alteration (Fig. 3). Petrography, whole-rock geochemistry, SEM, and XRD were used to characterize alteration in terms of mineralogical assemblages and geochemistry. The host rock

stratigraphy is, from top-down: dolomite, carbonaceous phyllite (GXN), major quartz vein (VQZ), quartz-chlorite-sericite-garnet schist (GNCX), and metagraywacke (Fig. 1D, Fig. 4A-B). Rare dikes of biotite-chlorite schist (BCS) and quartz-garnet-sericite schist (QGSS) crosscut the sequence. A mafic dike is suggested as protolith for both dikes, which is intensely hydrothermally altered and with its matrix substituted. Lenses of GNCX inside carbonaceous phyllite and lenses of dolomite inside GNCX and carbonaceous phyllite are rare.
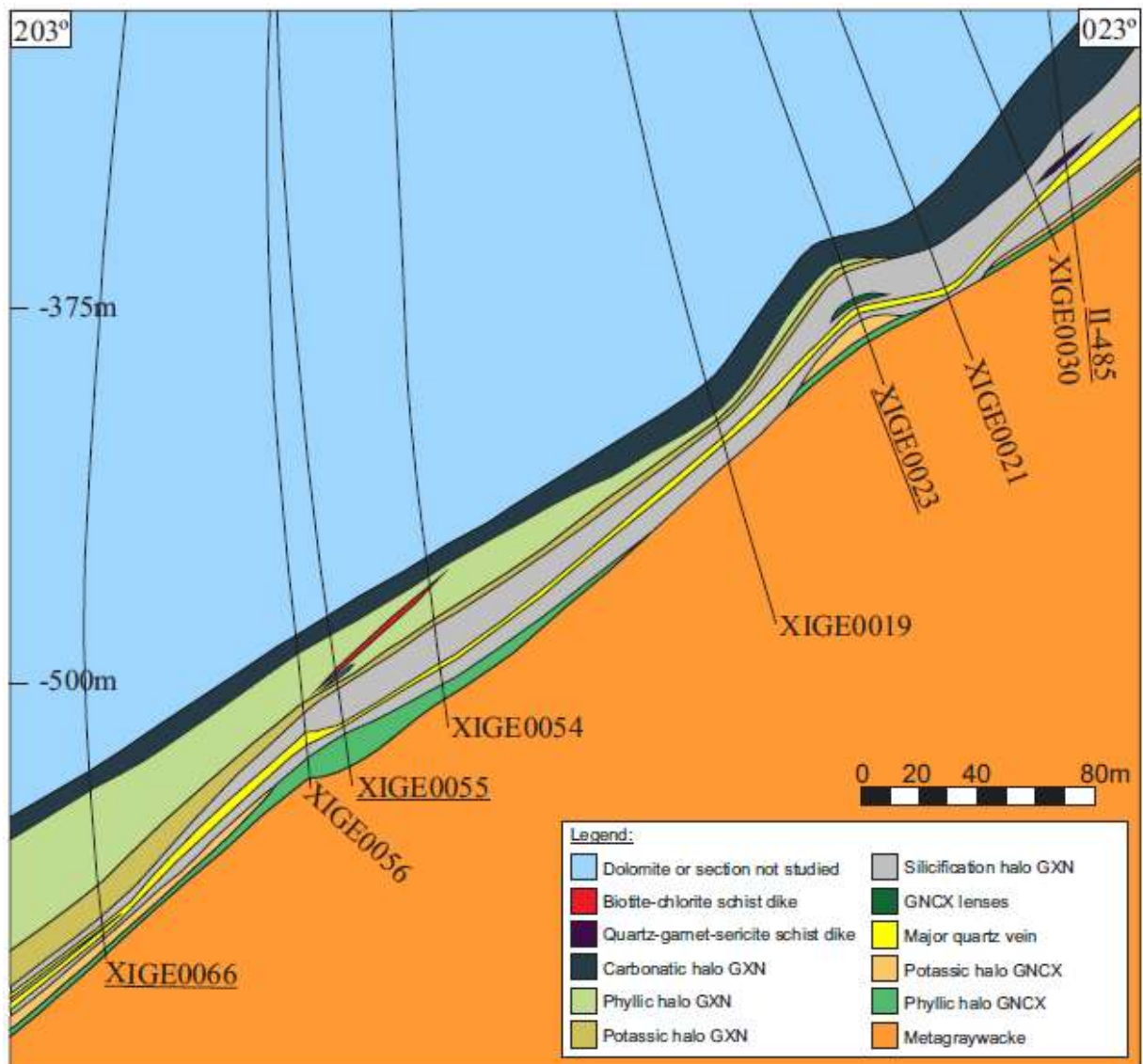
Fig. 3. Ingá orebody stratigraphic section. Drill holes studied have underlined names: II-485, XIGE0023, XIGE0055, and XIGE0066. Abbreviations: GNCX = Quartz-Chlorite-Sericite-Garnet Schist; GXN = Carbonaceous Schist.

The dolomite is > 9.4m thick and has a gradual-diffuse lower contact with the carbonaceous phyllite and a diffuse upper contact with the metabasalt or quartz-chlorite-carbonate-sericite schist. Three types of dolomite are identified based on texture: massive (Fig. 4C), brecciated (Fig. 4G), and laminated (Fig. 4H). The massive dolomite has uniform rounded carbonate-quartz-feldspar crystals, while the brecciated dolomite has large allotriomorphic carbonate-quartz-feldspar crystals, with quartz-plagioclase being more abundant. The laminated dolomite contain fine carbonate-quartz-

feldspar crystals oriented along S1 parallel to S2. The dolomite color varies from light gray to white, with green pockets mm to < 8 cm in thickness related to a high concentration of chlorite-biotite. It contains centimetric to decimetric carbonaceous phyllite lenses where quartz-carbonate millimeter-scale venulations may occur. Due to folding of the sequence, dolomite lenses occur in the GNCX. Mineral assemblage shows that dolomite and ankerite comprise 88 vol%, quartz 4 vol%, feldspar 2 vol%, biotite 2 vol%, pyrrothite 1.5 vol%, illite/muscovite/kaolinite 1 vol%, plagioclase < 1 vol%, zircon and titanite < 1 vol%, chalcopyrite < 1 vol%, and roscoelite < 1 vol%.
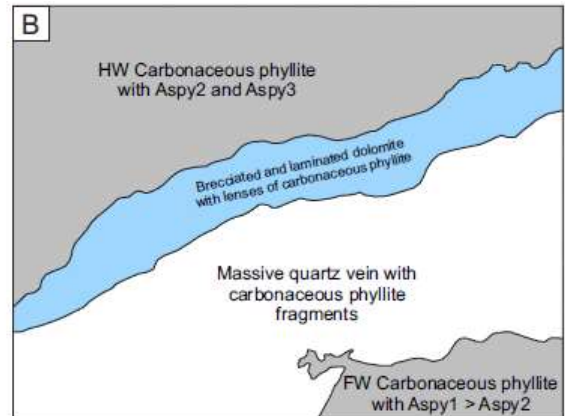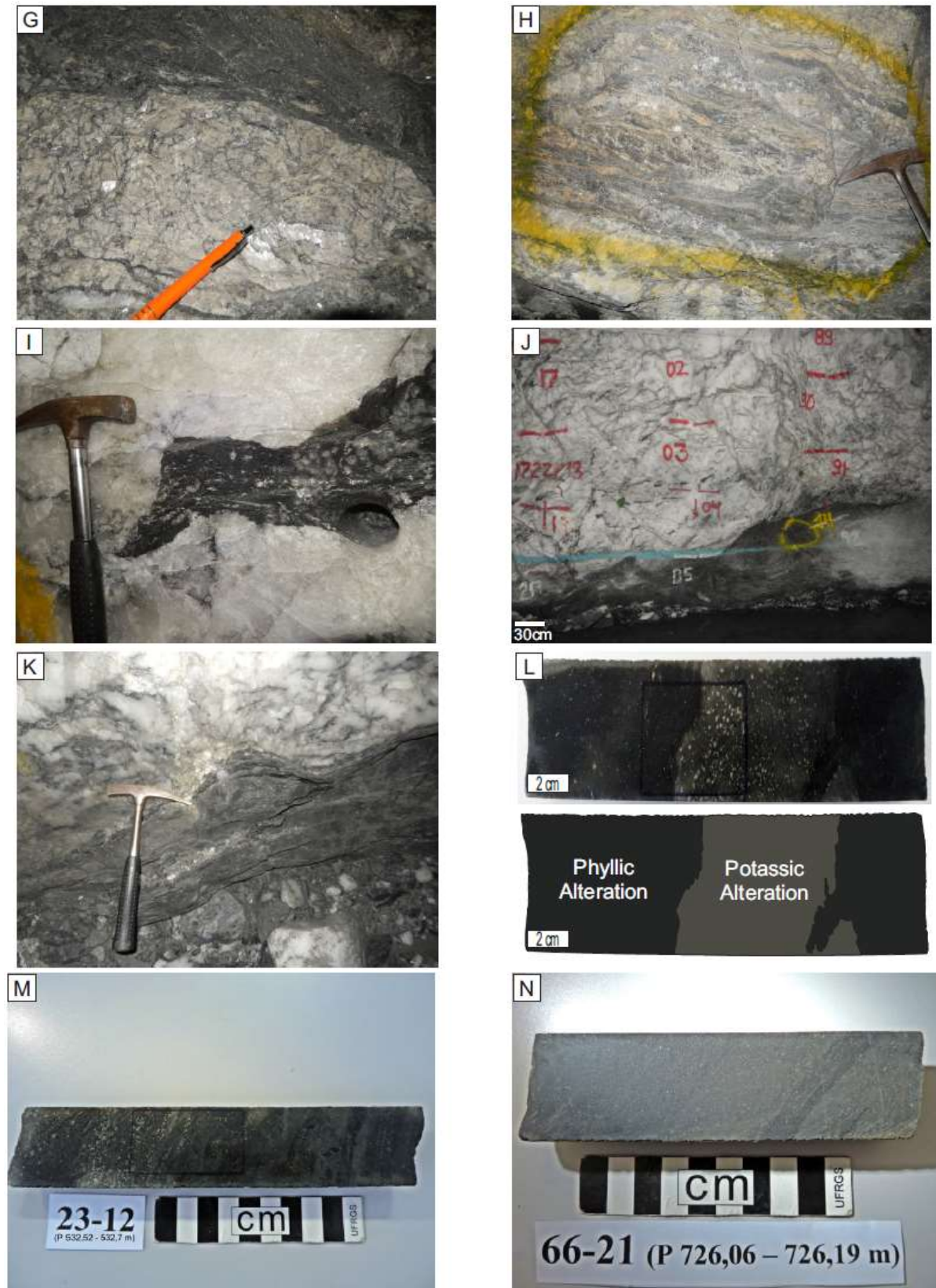
Fig. 4. Ingá orebody Lower Zone host rocks. (A) Host rocks in underground gallery. (B) Image A vectorized. (C) Massive dolomite. (D) Biotite-chlorite schist dike. (E) Quartz-garnet-sericite schist dike. (F) Hanging-wall carbonaceous phyllite. (G) Brecciated dolomite. (H) Laminated dolomite. (I) Carbonaceous phyllite lenses in major quartz vein. (J) Major quartz vein. (K) Footwall carbonaceous phyllite. (L) Phyllic to potassic alteration. (M) Quartz-chlorite-sericite-garnet schist. (N) Metagraywacke. Abbreviations: Aspy = arsenopyrite.

The biotite-chlorite schist (BCS) dike is < 2.54 m thick and has a diffuse upper contact with dolomite and an abrupt lower contact with the carbonaceous phyllite (Fig. 4D). The BCS dike color is dark green due to intense chloritization. Quartz-carbonate venulations and pockets, and punctuations of biotite and sericite are common. Mineral assemblage show quartz 38 vol%, chlorite 25 vol%, feldspar 19 vol%, biotite 10 vol%, carbonate 3 vol%, carbonaceous matter 3 vol%, sericite 1 vol%, plagioclase < 1 vol%, ilmenite < 1 vol%, and magnetite < 1 vol%.

The quartz-garnet-sericite schist (QGSS) dike is < 1.53 m thick and has abrupt lower and upper contact with carbonaceous phyllite (Fig. 4E). The QGSS color is greenish dark gray punctuated by light gray garnet crystals. Quartz-carbonate sub-mm to mm venulations are common. Mineral assemblage show quartz 20 vol%, white mica 28 vol%, garnet 13 vol%, carbonaceous matter 13 vol%, biotite 10 vol%, feldspar 5 vol%, ilmenite 3 vol%, hornblende 2 vol%, pyrrhotite < 1-4 vol%, chalcopyrite 1 vol%, carbonate < 1 vol%, chlorite < 1 vol%, Aspy1 < 1 vol%, magnetite and pentlandite < 1 vol%.

The major quartz-vein is 0.14 to 2.49 m thick and has abrupt upper and lower contact with carbonaceous phyllite (Fig. 4J). It generally crosscuts the carbonaceous phyllite near its lower contact with GNCX. It is mainly milky and commonly folded, with scarce glassy or smoky textured portions that are discontinuous. This vein commonly contains intensely foliated carbonaceous phyllite slivers, with irregular shapes, chlorite, and tourmaline (Fig. 4I). Centimetric irregular carbonate venulations are common. The VQZ is the main feature of the thrust structure III, parallel to oblique to it, and represents the main mining target of the Ingá orebody Lower Zone. The major quartz vein represents a set of crack and seal veining formed due to permeability anisotropy within the carbonaceous schist. It can be also classified as fault-fill veining according to Robert and Poulsen (2001).

The central part of the VQZ represents the merging and juxtaposition of numerous quartz veinlets. On its vertical terminations, the VQZ grades into metric-decimetric sheeted veinlet zone to centimentric isolated veinlets. Late steeply dipping, centimetric-decimetric quartz veins, with carbonaceous material and minimal wall rock displacement suggests emplacement along a tension fracture within the major quartz vein. Mesoscopically, the quartz is mainly laminated, commonly separated by slip surfaces enhanced by the presence of chlorite and tourmaline. Striations are present in these slip surfaces and are sub-parallel to the elongation lineation in the foliated carbonaceous phyllite. The individual laminae are parallel to subparallel to the vein margins. The free gold related to VQZ concentrates up to 0.9 m inwards from the footwall contact with the carbonaceous phyllite. In the carbonaceous phyllite slivers inside VQZ, commonly occurs two generations of arsenopyrite, in which the later contains gold as inclusions, filling fractures or in its margins. With increased F2 folding, gold grades become progressively higher towards F2 fold axis. The mineral assemblage is composed by quartz 95-97 vol%, chlorite 2 vol%, carbonate 1%, carbonaceous matter < 1 to 1 vol%, white mica < 1 to 1 vol%, biotite < 1 vol%, tourmaline < 1 vol%, and gold 0 to < 1 vol%.

The metagraywacke is > 13.73 m thick and has a diffuse and interdigitated upper contact with the GNCX (Fig. 4N). Its lower contact is unknown since no drill hole has ever crossed another lithology below the metagraywacke in the Ingá orebody due to drill hole depths and the lack of economic gold concentrations within the metagraywacke in this region. The metagraywacke is dark gray in color. Interdigitated lenses of GNCX are present and common with a 0.5 to < 5 cm size-range. The original rhythmic layering of the graywacke is preserved, with graded bedding, cross-lamination, cut and fill, and local intraformational breccias with irregular clasts of carbonaceous phyllite. Rare quartz-carbonate millimetric venulations occur. Mineral assemblage shows almost equal proportions of quartz, biotite and albite, oligoclase or andesine, locally muscovite, with minor zircon, magnetite, ilmenite, rutile and apatite, as well as millimetric sized rock fragments with quartz, plagioclase and biotite.

Hydrothermal Alteration Assemblage

The hydrothermal alteration zoning is characterized by four main haloes and respective assemblages that affect the carbonaceous phyllite and the quartz-chlorite-sericite-garnet schist (GNCX), in the following sequence: Carbonatic, Phyllic, Potassic, and Silicification haloes (Fig. 3, Table 3A and 3B). The haloes together sum 36 to 83 meters thick in the drill holes studied.
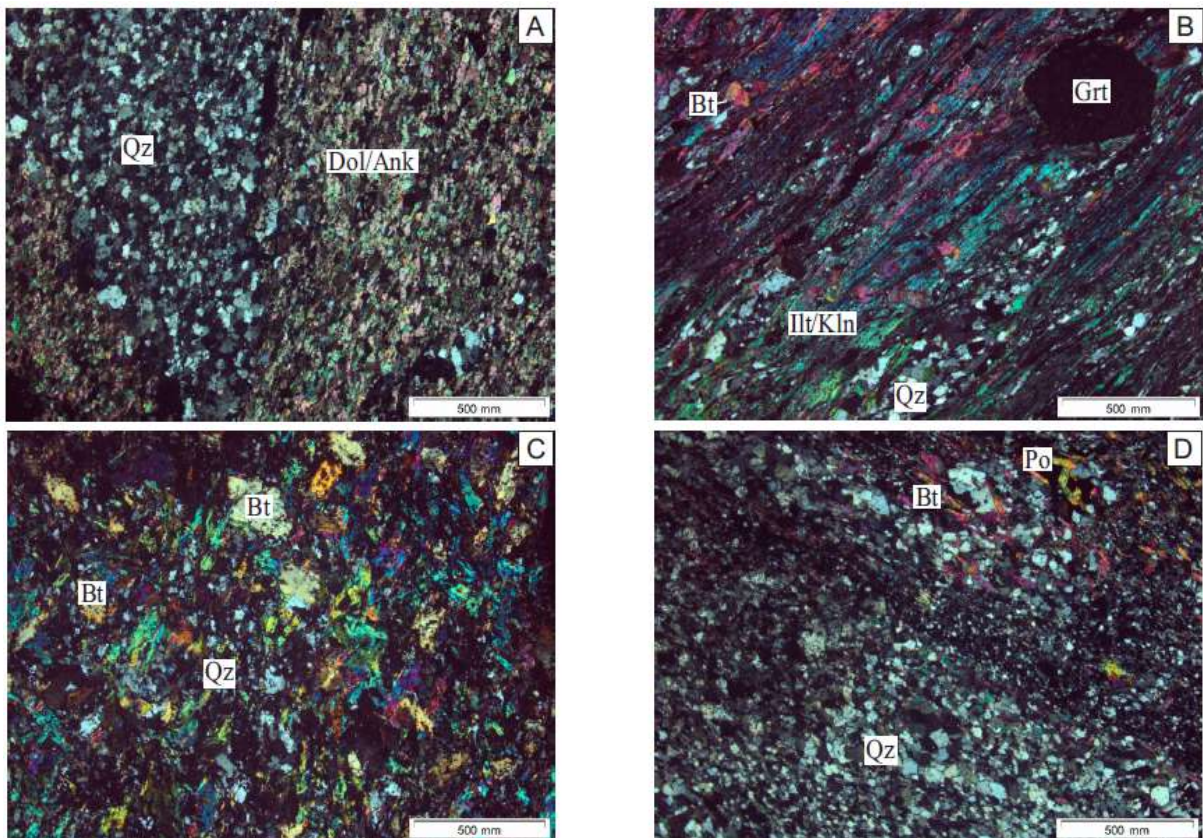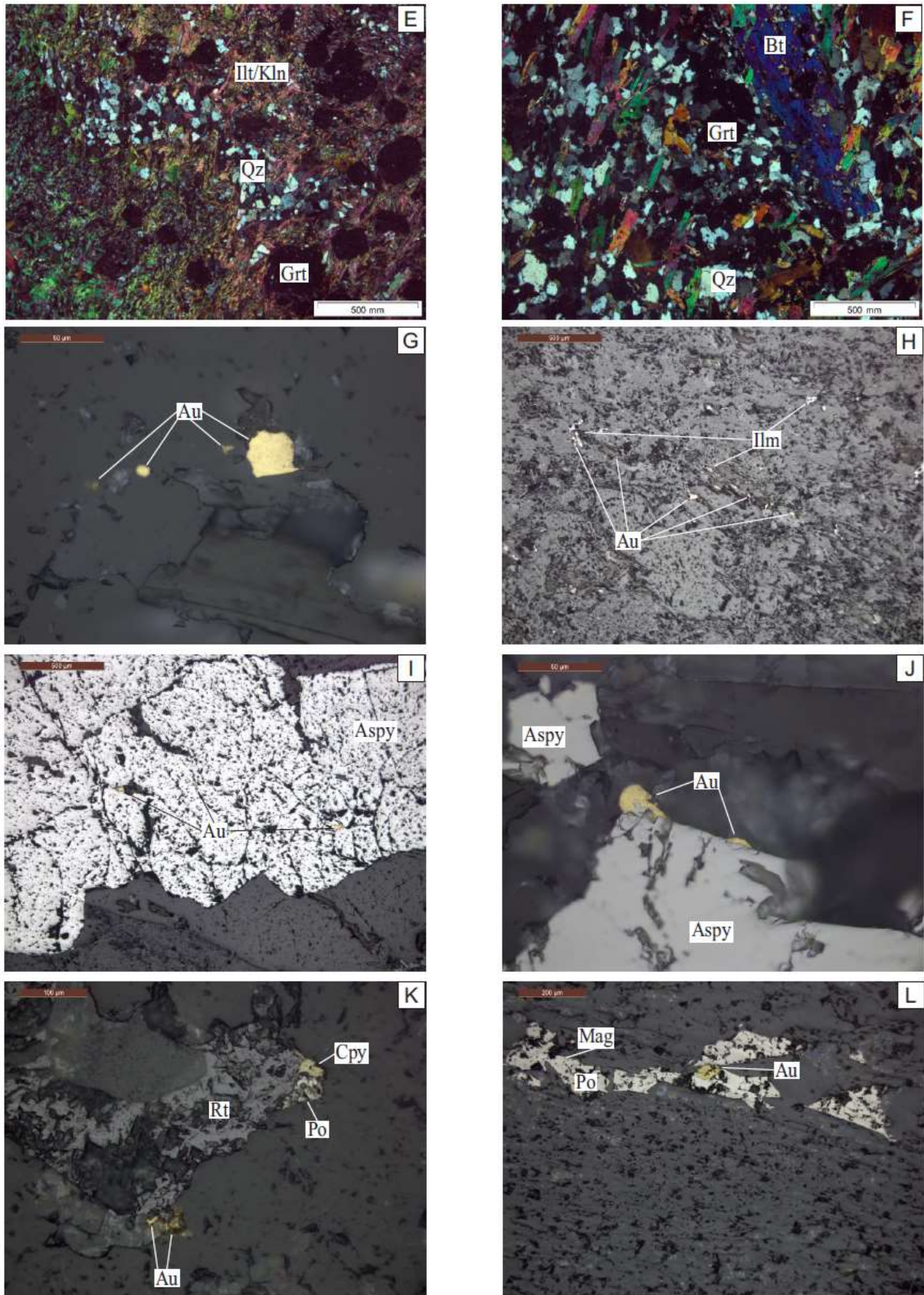
Fig. 5. Ingá orebody hydrothermal alteration zoning and gold mineralization. (A) Carbonatic zone GXN. (B) Phyllic zone GXN. (C) Potassic zone GXN. (D) Silicification zone GXN. (E) Phyllic zone GNCX. (F) Potassic zone GNCX. (G) Visible gold in quartz vein. (H) Visible gold in gangue. (I) Gold on Aspy3 borders, included and filling fractures in Aspy3. (J) Gold on Aspy3 borders. (K) Gold on rutile borders. (L) Gold on pyrrothite borders. Abbreviations: Ank = ankerite, Aspy = arsenopyrite, Au = gold, Bt = biotite, GXN = carbonaceous phyllite, Cpy

= chalcopyrite, Dol = dolomite, Grt = garnet, Ilm = ilmenite, Ilt = illite, Kln = kaolinite, Mag = magnetite, Po = pyrrothite, GNCX = quartz-chlorite-sericite-garnet schist, Qz = quartz, Rt = rutile.

The carbonatic halo affects the carbonaceous phyllite pervasively with thicknesses of 1.2 to 17.6 meters, which decrease progressively along the Ingá orebody plunge, reflecting the decrease in thickness of the adjacent dolomite up the stratigraphic sequence (Fig. 5A). It presents a diffuse gradual upper contact with the dolomites and a diffuse gradual lower contact with the phyllic zone carbonaceous phyllite. Carbonates in this halo were identified by SEM and XRD as mainly dolomite, with subordinated ankerite and calcite. The dolomite is suggested as the source of $CaCO_3$ for the carbonatic halo. Metric to decimetric intercalations of carbonaceous phyllite from carbonatic halo and the phyllic halo commonly occur due to deformation. Rare BCS dikes crosscut the carbonatic halo. The carbonaceous phyllite in this halo presents medium gray color, which varies in tone with more or less carbonaceous matter or carbonate abundance. It presents a fairly common brecciated aspect and also centimetric greenish zones due to chlorite alteration. Carbonate pockets and veins are common with millimeter to centimeter sizes. Hydrothermalized mafic pockets are common along all of the carbonatic halo and consist of a carbonate-sericite-biotite-chlorite-quartz assemblage.

General mineral assemblage of the carbonatic halo over the carbonaceous phyllite show dolomite/ankerite/calcite < 1 to 87 vol%, quartz 10-20 vol%, chlorite 0-15 vol%, carbonaceous matter 3-10 vol%, feldspar 3-5 vol%, illite/muscovite/kaolinite 0-5 vol%, biotite 0-2 vol%, plagioclase 0-1 vol%, clinozoisite < 1 vol%, titanite, and zircon < 1 vol%. Ore mineralogy includes: pyrrhotite 0-2 vol%, pentlandite < 1 vol%, ilmenite < 1 vol%, chalcopyrite < 1 vol%, Aspy1 < 1 vol%, rutile 0-1 vol%, and magnetite < 1 vol%.

Table 3a. Paragenetic Sequence of Ore and Gangue Minerals of the Inga Orebody Lower Zone Bearing Gold GXN.

Carbonaceous Schist (GXN) Minerals		Hydrothermal alteration haloes (outer-inner)				
		Pre-hydrothermal	Carbonatic	Phyllic	Potassic	Silicification
Gangue minerals	Ankerite	····	····	····	····	····
	Apatite	····	····	····	····	····
	Barite	····	····	····	····	····
	Biotite 1 and 2 (Ferri-biotite)			█	█	█
	Calcite	····	····	█		█
	Carbonaceous material	█	····	█		█
	Chlorite 1 and 2 (Ripidolite)	····	····	····	····	····
	Clinozoisite	····	····	····	····	····
	Dolomite	····	█	····	····	····
	Garnet 1 and 2 (Almandine)	····	····	····	····	····
	Hornblende	····	····	····	····	····
	K-feldspar	····	····	····	····	····
	Plagioclase	····	····	····	····	····
	Quartz	█	█	█	█	█
	Roscoelite	····	····	····	····	····
	Sericite	····	····	█	█	█
	Titanite	····	····	····	····	····
	Tourmaline	····	····	····	····	····
	White mica 1 and 2 (Phengitic muscovite)	····	····	█	█	█
	Zircon	····	····	····	····	····
Ore minerals	Arsenopyrite 1	····	····	····	····	····
	Arsenopyrite 2 and 3	····	····	····	····	█
	Chalcopyrite	····	····	····	····	····
	Gold	····	····	····	····	····
	Ilmenite	····	····	····	····	····
	Magnetite	····	····	····	····	····
	Pentlandite (Stage I and III)	····	····	····	····	····
	Pyrrhotite (Stage I and III)	····	····	····	····	····
	Rutile	····	····	····	····	····

Table 3b. Paragenetic Sequence of Ore and Gangue Minerals of the Ingá Orebody Lower Zone Bearing Gold GNCX.

Quartz-chlorite-sericite-garnet schist (GNCX) Minerals		Hydrothermal alteration haloes (outer-inner)		
		Pre-hydrothermal	Phyllic	Potassic
Gangue minerals	Ankerite		....	....
	Barite		....	....
	Biotite 1 and 2 (Ferri-biotite)		████████████	████████████
	Calcite	....	....	....
	Carbonaceous material	████████████	████████████	████████████
	Chlorite 1 and 2 (Ripidolite)		------------	------------
	Clinozoisite		....	....
	Dolomite	....	....	
	Garnet 1 and 2 (Almandine)	------------	------------	------------
	Hornblende		....	------------
	K-feldspar	------------	------------	------------
	Plagioclase	....	....	....
	Quartz	------------	████████████	████████████
	Sericite		████████████	------------
	White mica 1 and 2 (Phengitic muscovite)		████████████	------------
	Zircon			....
Ore minerals	Arsenopyrite 1			....
	Chalcopyrite		....	....
	Gold			....
	Ilmenite		------------	....
	Magnetite		....	....
	Pentlandite (Stage I and III)		....	....
	Pyrrhotite (Stage I and III)		....	....

Main	██████████████
Minor	------------------
Locally occurrir	....

The Phyllic halo pervasively selective affects the carbonaceous phyllite and the GNCX, with thicknesses of 1.7 to 14.2 m, thickening progressively along the Ingá orebody plunge (Fig. 4L and 4M, Fig. 5B and 5E). The carbonaceous phyllite has a diffuse gradational upper contact with the carbonatic halo and a diffuse gradational lower contact with the potassic halo. For the GNCX, it has a diffuse gradational upper contact with the potassic halo and a diffuse interdigitated lower contact with the metagraywacke. White mica in this halo was identified by SEM, XRD, and EMP as being mainly phengitic muscovite, with subordinated illite and kaolinite. Millimeter to centimeter-scale quartz veins are common, with assimilated host rock fragments. Sub-millimetric carbonate veining is rare. Centimeter to meter-scale light gray levels present subordinated potassic alteration pervasively selective overprinting the phyllic alteration. The phyllic halo on carbonaceous phyllite rarely present disperse carbonaceous matter clasts concentrated in centimetric levels. This is common in the GNCX, which indicates metagraywacke contribution. Late subordinated chloritization is common. QGSS dikes rarely crosscut the phyllic halo carbonaceous phyllite. Dolomite lenses rarely crosscut the GNCX.

The general mineral assemblage of the phyllic halo over the carbonaceous phyllite includes: quartz 20-40 vol%, white mica 8-30 vol%, carbonaceous matter 4-30 vol%, biotite 5-20 vol%, garnet 0-12 vol%, carbonate 0-13 vol%, k-feldspar 4-8 vol%, chlorite 1-6 vol%, clinozoisite 0-3 vol%,

plagioclase 0-1 vol%, titanite < 1 vol%, zircon < 1 vol%. Ore mineralogy includes: pyrrothite 1-4 vol%, chalcopyrite 1 vol%, ilmenite <1 to 2.5 vol%, Aspy1 < 1 vol%, rutile < 1 vol%, magnetite < 1 vol%, and pentlandite < 1 vol%. General mineral assemblage of the phyllic halo over the quartz-chlorite-sericite-garnet schist include: quartz 20-40 vol%, white mica 15-35 vol%, carbonaceous matter 5-25 vol%, biotite 6-15 vol%, garnet 4-13 vol%, k-feldspar 4-8 vol%, chlorite 1-4 vol%, hornblende 0-4 vol%, clinozoisite 0-5 vol%, carbonate <1 vol%, and plagioclase < 1 vol%. Ore mineralogy includes: pyrrhotite < 1 to 3 vol%, chalcopyrite < 1 vol%, ilmenite < 1 to 1 vol%, magnetite < 1 vol%, and pentlandite < 1 vol%.

The potassic halo affects the carbonaceous phyllite and the GNCX pervasively-selective with thickness of 1.6 to 17.3 meters, increasing progressively along the Ingá orebody plunge (Fig. 4L, Fig. 5C and 5F). It presents a gradational and diffuse contact with the phyllic and silicification halo in both carbonaceous phyllite and GNCX. The ferri-biotite was identified as characteristic of this halo by SEM, XRD, and EMP and it occurs as an abrupt overprinting of the phyllic alteration, giving a yellowish dark gray coloration to the host rock. Garnets become light gray due to this overprint. Posterior decimetric quartz-carbonate venulations are common, containing carbonaceous phyllite or GNCX fragments. Late rare subordinated pervasive silicification occurs related to this veining, increasing abundance towards the major quartz vein. It presents disperse carbonaceous matter clasts concentrated in some centimetric levels indicating metagraywacke contribution.

General mineral assemblage of the potassic halo over the carbonaceous phyllite includes: quartz 20-40 vol%, carbonaceous matter 1-23 vol%, biotite 15-20 vol%, garnet 0-12 vol%, apatite 0-11 vol%, k-feldspar 4-8%, white mica 0-4 vol%, chlorite 0-3 vol%, carbonate < 1 vol%, titanite < 1 vol%, plagioclase < 1 vol%, zircon < 1 vol%. Ore mineralogy includes: pyrrhotite 0-3 vol%, ilmenite 0-2 vol%, chalcopyrite < 1 vol%, Aspy1 < 1 vol%, magnetite < 1 vol%, and pentlandite < 1 vol%. General mineral assemblage of the potassic halo over the GNCX includes: quartz 20-40 vol%, biotite 17-25 vol%, carbonaceous matter 2-25 vol%, white mica 0-20 vol%, hornblende 0-23 vol%, garnet 4-13 vol%, chlorite 1-10 vol%, k-feldspar 4-8 vol%, carbonate < 1 vol%, zircon < 1 vol%. Ore mineralogy includes: pyrrothite <1-1.5 vol%, chalcopyrite < 1 vol%, ilmenite < 1 vol%, Aspy1 < 1 vol%, magnetite < 1 vol%, and pentlandite < 1 vol%.

The silicification halo (Fig. 4F and 4K, Fig. 5D) affects the carbonaceous phyllite pervasively with thickness of 0.8 to 17.7 meters outwards from the major quartz vein (VQZ). Its thickness has a positive correlation with the thickness of the major quartz vein, decreasing progressively along the Ingá orebody plunge. The silicification intensity is determined by the abundance of quartz crystals and increases towards the thrust structure III and VQZ. Its upper and lower limits are in gradational, diffuse contact with the potassic halo, overprinting it. It presents dark gray color varying to lighter tones due to silicification intensity. Carbonaceous phyllite and milky quartz veins occur interdigitated in decimetric intervals due to the assimilation of quartz veins. In intervals of very high silicification,

garnet disappears. When the silicification halo reaches the GNCX, the silicification almost ceases due to the reactivity differences between silicification and the host rock, marking the lower limit of the silicification halo. QGCS dikes rarely crosscut this halo and do so with abrupt contacts. In the silicification halo, particularly in the venulations, millimetric chlorite occurs disseminated over the quartz with 1-5 vol%. Free gold and gold in the Aspy3 concentrates in the carbonaceous phyllite mainly in the hanging-wall of the major quartz vein. The carbonaceous phyllite in the footwall of the VQZ, which contains Aspy1, rarely contains gold as free crystals within the matrix.

Measured foliation data (n=58) in the Ingá carbonaceous schist (Fig. 6) show an average azimuth value of 229° (200-300°) and an average dip value of 39° (25-66°). Measured L2 stretching lineation data (n=50), that marks the mineralization plunge, show an average trend value of 275° (260-315°) and an average plunge value of 27° (20-57°). S0 was not observed in Ingá orebody due to the penetrative character of the S1 foliation. S0 and S1 foliation in the Ingá orebody are assumed to be parallel to sub-parallel to S2. The axial surface of F2 folds are rarely physically present, marked by the rotation of mica flakes formed during D1, thus statistically few F2 fold axis measurements were collected. S3 and S4 foliations were not observed at Ingá orebody gallery. S3 foliation was observed in Ingá exploration drill holes, but as the drill holes were not oriented, it was not possible to get absolute measurements.
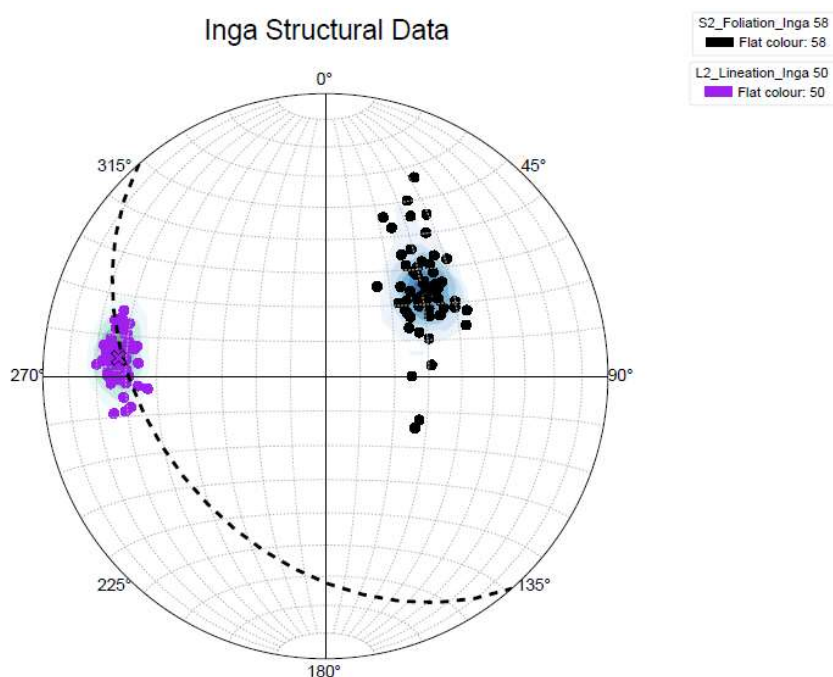
Fig. 6. Carbonaceous phyllite S2 foliation (n = 58) and L2 lineation (n = 50) stereonets. Equal-area Schmidt projection.

General mineral assemblage of the silicification halo over the carbonaceous phyllite includes: quartz 25-60 vol%, biotite 2-30 vol%, white mica 0-32 vol%, garnet 0-25 vol%, carbonaceous matter 0-30 vol%, carbonate 0-15 vol%, clinozoisite 0-10 vol%, k-feldspar 4-7 vol%, hornblende 0-7 vol%, chlorite 0-5 vol%, apatite 0-5 vol%, tourmaline 0-4 vol%, plagioclase 0-2 vol%, roscoelite < 1 vol%,

titatine < 1 vol%, and zircon < 1 vol%. Ore mineralogy includes: Aspy2 and Aspy3 0-15 vol%, pyrrhothite < 1-8 vol%, ilmenite 0-5 vol%, chalcopyrite 0-1 vol%, Aspy1 < 1 vol%, magnetite < 1 vol%, pentlandite < 1 vol%, rutile < 1 vol%, and gold < 1 vol%.

Hydrothermal Alteration Geochemistry

The main hydrothermal minerals in the area were analysed in detail, including: carbonates, white mica, biotite, quartz, chlorite, and garnet. The carbonate (0-87 vol%), in the alteration haloes was analyzed by SEM and quantitative analysis in XRD (n=20) with carbonaceous phyllite and quartz-chlorite-sericite-garnet schist as host rocks. Carbonate crystals are < 0.003 to 2.4 mm in size and occur in three ways: (1) crystalline aggregates in venulations and pockets, (2) crystalline aggregates in the matrix, and (3) amorphous tardi disseminated aggregates on other crystals in the matrix. Type three rarely occurs in Aspy2 and Aspy3 fractures and margins. Carbonate crystals acquire a strained shape when oriented along S2 foliation, but mainly are rounded with no preferred orientation. Carbonate crystals are pointed by submillimetric carbonaceous matter with a quartz and illite/kaolinite overprint, lending a dirty aspect to the crystal. Carbonate1 and Carbonate2 composition is mainly ankerite with subordinated calcite and very rare dolomite in the phyllic and potassic zones over GXN and GNCX and in the silicification zone over GXN. In the carbonatic zone, the Carbonate1 and Carbonate2 composition is mainly dolomite with rare calcite. Carbonate3 composition is calcite in all hydrothermal alteration haloes.

White mica in the alteration haloes (0-35 vol%) was analyzed by SEM, quantitative analysis in EMP (n=48) and in XRD (n=20) with carbonaceous phyllite and quartz-chlorite-sericite-garnet schist as host rocks (Table 5). White mica crystals are < 0.003 to 0.25 mm in size and occurs as aggregates in two ways: (1) disseminated in the matrix or (2) in quartz-carbonate microvenulations. White mica1 occurs mainly along S2 foliation but also is common oblique/perpendicular to S2 foliation. White mica1 has weak to regular cleavage while White mica2 has good cleavage. White mica1 and 2 show partial to total alteration to chlorite. White mica1 and 2 compositions are the same (Fig. 8G), classified as phengitic muscovite: Fe+Mg (0.27-0.49; Avg 0.36), K (1.66-1.78; Avg 1.73), Al iv (1.70-1.97; Avg 1.86), Al vi (3.54-3.78; Avg 3.67), and Al total (5.24-5.75; Avg 5.53). Fine-grained white mica < 0.003 mm that forms argilominerals is classified as kaolinite and illite by XRD analysis. Particularly in the carbonatic zone, the phengitic muscovite occurs in mafic hydrothermalized pockets.

Table 4. Average Compositions of Garnet, Chlorite, Sericite and Biotite from Hydrothermally Altered Host Rocks of the Ingá Orebody Lower Zone, Crixás Gold District.

Oxide (%)	Garnet (n = 139)		Chlorite (n = 43)		Sericite (n = 48)		Biotite (n = 48)	
	Average	STD	Average	STD	Average	STD	Average	STD
SiO2	36.10452	1.671145	25.09186	0.401825	46.15125	0.536171	36.57292	0.527834
TiO2	0.069629	0.033522	0.078898	0.021216	0.383017	0.069867	1.445715	0.283338
Al2O3	21.07166	0.809119	22.47907	0.576293	35.25479	0.636694	18.98938	0.400119
FeO	33.25377	1.134456	25.48698	0.814381	1.340575	0.162312	17.96104	1.592014
MnO	1.736141	1.258095	0.094128	0.074279	0.008546	0.011412	0.069127	0.032588
MgO	1.377603	0.316785	14.95256	0.549732	1.043979	0.201679	10.90292	1.017826
CaO	6.165911	0.794266	0.015228	0.017289	0.008042	0.009909	0.00945	0.010222
Na2O	0.010803	0.015963	0.00754	0.011482	0.663467	0.07171	0.147258	0.029825
K2O	-0.00531	0.007073	0.014181	0.035232	10.20979	0.201595	9.27125	0.144776
BaO	0	0	0.014881	0.018831	0.699567	0.258951	0.281708	0.070735
Rb2O	0	0	0	0	0	0	0	0
Cs2O	0	0	0	0	0	0	0	0
ZnO	0	0	0	0	0	0	0	0
F	0	0	0.06953	0.11714	0.1368	0.128857	0.432846	0.168442
Cl	0	0	0.014835	0.017584	0.003731	0.004377	0.0192	0.011634
Cr2O3	0.045817	0.023992	0	0	0	0	0	0
NiO	0	0	0	0	0	0	0	0
SrO	NA	NA	NA	NA	0	0	0	0
SnO2	NA	NA	NA	NA	0	0	0	0
Ga2O3	NA	NA	NA	NA	0	0	0	0
CuO	NA	NA	NA	NA	0	0	0	0
Li2O*	NA	NA	NA	NA	0	0	0	0
H2O*	NA	NA	11.38609	0.125909	4.440516	0.064163	3.780289	0.090976
Total (%)	99.83054	2.545576	99.70779	0.543176	100.2856	0.359281	99.69652	0.505383
No. of oxygens	12	0	28	0	24	0	24	0
Si	2.930134	0.053805	5.236498	0.07958	6.141032	0.057699	5.495591	0.037695
Al iv	0.069866	0.053805	2.763502	0.07958	1.858968	0.057699	2.504409	0.037695
Total	3	0	8	0	8	0	8	0
Al vi	1.949854	0.047639	2.777319	0.064826	3.670639	0.049157	0.859023	0.062942
Ti	0.004254	0.002079	0.012372	0.003292	0.038328	0.006979	0.163554	0.032665
Cr	0.002942	0.001534	0	0	0	0	0	0
Fe3+	0.038199	0.042141	0.054163	0.038855	NA	NA	NA	NA
Fe2+	2.221988	0.08051	4.397154	0.187093	NA	NA	NA	NA
Fe	NA	NA	NA	NA	0.149202	0.018159	2.258818	0.217276
Sn	NA	NA	NA	NA	0	0	0	0
Ga	NA	NA	NA	NA	0	0	0	0
Cu	NA	NA	NA	NA	0	0	0	0
Li*	NA	NA	NA	NA	0	0	0	0
Mn	0.119426	0.086164	0.016572	0.013024	0.000963	0.001285	0.008787	0.004133
Mg	0.166694	0.037832	4.65101	0.148593	0.207036	0.039707	2.44088	0.210809
Ni	0	0	0	0	0	0	0	0
Zn	0	0	0	0	0	0	0	0
Ca	0.536619	0.068706	0.00342	0.00394	0.001145	0.00141	0.001523	0.001647
Na	NA	NA	0.006092	0.009272	0.171208	0.018717	0.042871	0.008502
K	NA	NA	0.007545	0.018748	1.732829	0.030327	1.777055	0.0233
Ba	NA	NA	0.002429	0.003071	0.036505	0.013602	0.01659	0.004195
Rb	NA	NA	0	0	0	0	0	0
Sr	NA	NA	NA	NA	0	0	0	0
Cs	NA	NA	NA	NA	0	0	0	0
F	NA	NA	0.091138	0.15271	0.057575	0.054273	0.205781	0.080238
Cl	NA	NA	0.01047	0.012376	0.000842	0.000988	0.004901	0.002978
OH*	NA	NA	15.89839	0.154073	3.941583	0.054069	3.789317	0.080567
Total	5.039976	0.03263	43.92808	0.07149	26.00785	0.016393	27.5691	0.035763
Fe/Fe+Mg	NA	NA	0.488992	0.016709	0.422074	0.047997	0.480562	0.044018

Notes: NA = do not apply

Biotite in the alteration haloes (0-30 vol%) was analyzed by SEM and quantitative analysis in EMP (n=48), with carbonaceous phyllite and quartz-chlorite-sericite-garnet schist as host rocks (Table 5). Biotite crystals are < 0.003 to 0.3 mm in size, commonly fragmented, and display light to dark-orange pleochroism. Biotite occurs in two ways: (1) disseminated in the matrix along the S2 foliation and (2) oblique/perpendicular to S2 foliation forming crystal aggregates without preferred orientation and with variable sizes. The Biotite1 is interpreted to be of metamorphic origin and Biotite2 is interpreted to be hydrothermal. Biotite1 crystals are allotriomorphic to hipidiomorphic in shape, showing weak to regular cleavage. Biotite2 crystals are hipidiomorphic to idiomorphic in shape showing regular to good cleavage and darker orange tones in pleochroism. Biotite1 and 2 show partial to total alteration to late chlorite. Biotite1 and Biotite2 compositions are approximately the same (Fig. 8E), classified as ferri-biotite according to the classification diagram by Speer (1981) and Deer et al. (1986): $Fe/(Fe+Mg)$ (0.43-0.57; Avg 0.48), Al iv (2.43-2.58; Avg 2.50) and Al (total) (3.22-3.48; Avg 3.36). Particularly in the carbonatic zone, the Biotite2 occurs in mafic hydrothermalized pockets.

Chlorite in the alteration haloes (0-15 vol%) was analyzed by element mapping in SEM and quantitative analysis in EMP (n=41) and XRD (n=20), with carbonaceous phyllite and quartz-chlorite-sericite-garnet schist as host rocks (Table 5). Chlorite is < 0.003 to 0.23 mm in size and has good cleavage. Chlorite occurs in two ways: (1) disseminated crystals in the matrix, the product of selective alteration of phyllosilicates, and (2) disseminated non-oriented aggregates in quartz-carbonate venulations. Chlorite1 and Chlorite2 compositions are approximately the same (Fig. 8F), classified as Ripidolite, according to the classification of Hey (1954): $Fe/(Fe+Mg)$ (0.45-0.51; Avg 0.49) and Si_{28} (5.06-5.38; Avg 5.24). Quartz in the alteration haloes (10-60 vol%) as well as in the major quartz vein was microstructurally analysed and is almost entirely recrystallized probably due to subgrain rotation and recrystallization during crystal-plastic deformation (Passchier and Trouw, 2005).

Garnet in the alteration haloes (0-25 vol%) was analyzed by element mapping in SEM and quantitative analysis in EMP (n=139), with carbonaceous phyllite and quartz-chlorite-sericite-garnet schist as host rocks (Table 5). Garnet crystals have 0.016 to 4.5 mm in size and hipidiomorphic-idiomorphic shape. They have a whitish to light pink color and are mainly zoned. The zonation is concentric and marked by the inclusion of fine carbonaceous matter in the garnet core. Garnet crystals are commonly associated with a greater concentration of mafic minerals and often form aggregates with ore minerals (ilmenite and chalcopyrite) and quartz inclusions. The carbonaceous matter mark the margins of the garnet crystals, which are moderately to highly fractured, with rare fractures filled by chalcopyrite. Two types of garnet were interpreted: (1) zoned garnet with calcic margin and (2) garnet without zonation or with incipient zonation. Both are predominantly composed of almandine and have a manganese core. The zoned garnet contains $Alm_{68,08-77,85}$ $Grs_{10,97-22,22}$ $Pyp_{3,47-8,01}$ $Sps_{0,93-11,38}$ $Andr_{0,07-1,77}$ $Uv_{0,00-0,43}$, a calcic margin, and a manganese core. The second type contains $Alm_{64,12-73,82}$ $Grs_{16,88-22,78}$ $Pyp_{3,53-7,68}$ $Sps_{0,89-12,15}$ $Andr_{0,00-1,42}$ $Uv_{0,00-0,24}$ and a manganese core. Both have higher concentrations of espessartite (Mn) in their cores and the Garnet1 show grossular and andradite

contribution (Ca) more significant in the margins (Fig. 8A-D). Garnet1 and Garnet2 are mostly metamorphic and pre-kinematics, with rare rotated crystals, but the crystals containing ilmenite and chalcopyrite as aggregates and in fractures underwent later deformation and hydrothermal alteration.
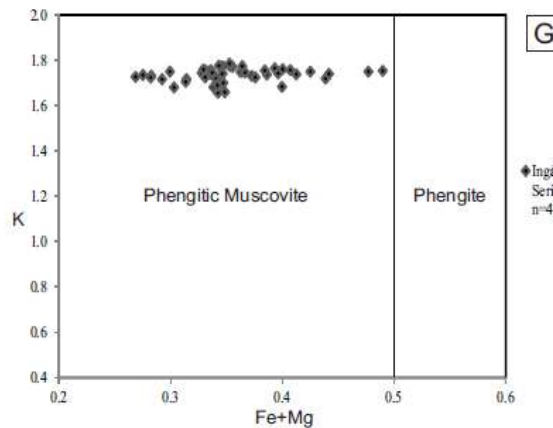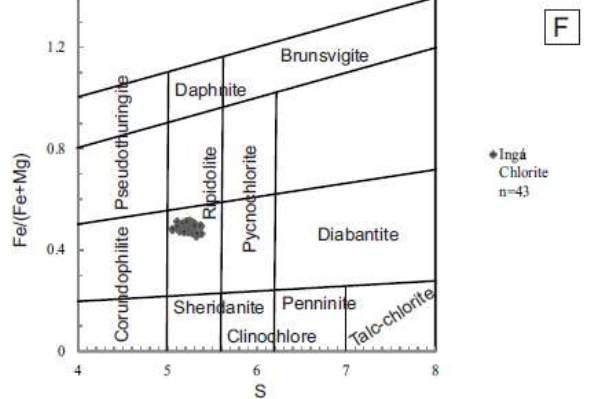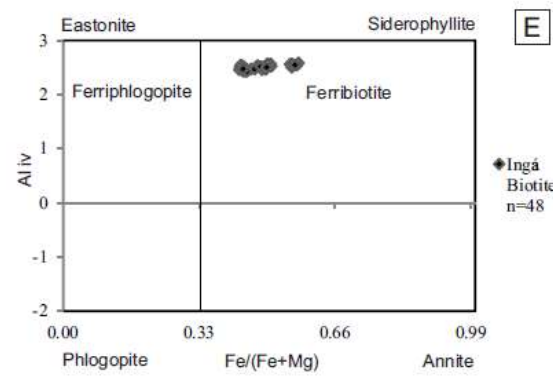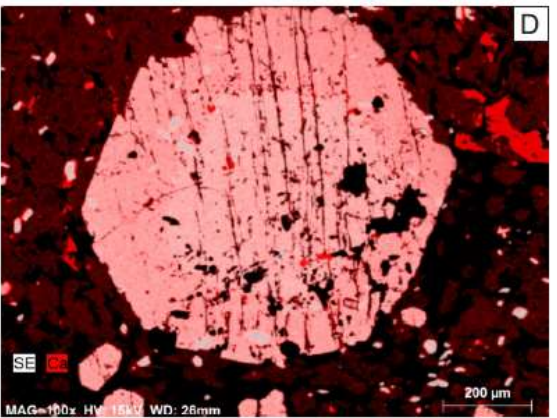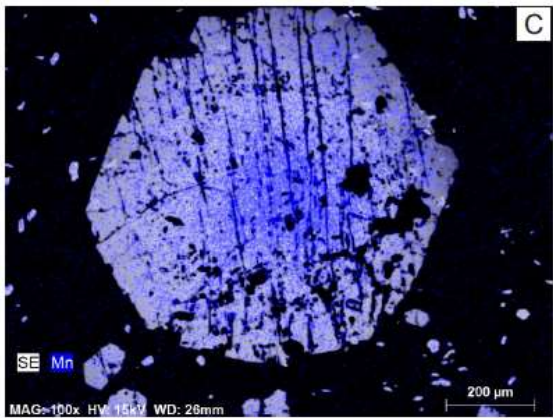
Fig. 7. A) Garnet BSE image with EMP points in line selected in red. B) EMP analysis of red points on garnet crystal in image A. C) Mn-rich garnet core in EDS-BSE image in SEM. D) Ca-rich garnet margins in EDS-BSE image in SEM. E) Biotite classification diagram af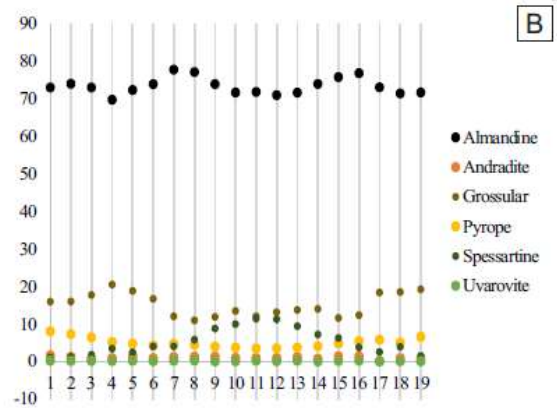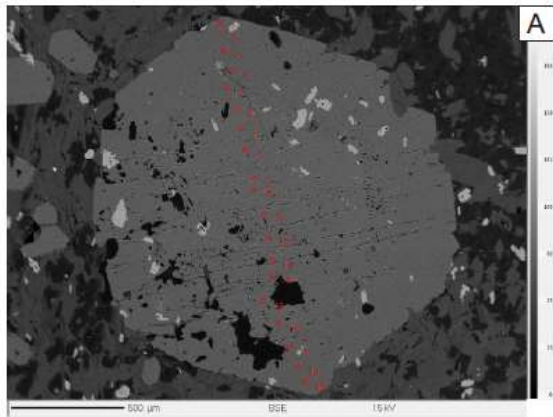ter Speer (1981) and Deer et al. (1986). F) Chlorite classification diagram after Hey (1954). G) Muscovite classification diagram.

A rigorous analysis of the volume and component concentration changes in the altered rocks (Table 4) was performed using the best-fit isocon method (Grant, 1986). This method quantifies the geochemical differences between altered and unaltered lithologies. When coupled with mineralogy it allows for the understanding of the migration of hydrothermal alteration along stratigraphy. Based on drill core logging, petrography, and whole-rock geochemical analysis, samples were selected to define the average composition of the least altered carbonaceous phyllite and quartz-chlorite-sericite-garnet schist. These samples were collected in lenses within the metagraywacke sequence that were not subjected to hydrothermal alteration. Al_2O_3 and or TiO_2 were used as the least mobile elements to define the best-fit isocon, based on the average cluster of slopes for these elements. Selenium was used as the least mobile element for the carbonatic zone altered carbonaceous phyllite, specifically. The isocon is a reference line passing through the origin, which correspond to zero concentration change, in a plot of the least altered sample versus the most altered sample. Elements data should be analyzed carefully due to hampering by the upper detection limit (As) and lower detection limit (SrO, Ge, Ag, Cd, Mo, Hg and Sb).

Table 5. Summary of the Host Rock, Alteration Facies, Mass Changes and Metal Associations of the Ingá Orebody Lower Zone.

Host Rock	Alteration Facies	Chemical Changes Gains wt% or ppm				Chemical Changes Losses wt% or ppm			
		>100%	>10%	>1%	0-1%	0-1%	>1%	>10%	>100%
Carbonaceous Phyllite	Carbonatic		CaO, MgO		Cd, Sb, P2O5, MnO, Hg, Se	Eu, Ho, Tb, Ta, TiO2, Lu, Tl, Tm, Bi, Ge, S, In, Re	Pb, Sc, Th, Pr, Hf, Fe2O3, Sm, Gd, Dy, Cs, Na2O, Yb, U, Er, Sn, K2O, W	Ni, Ce, Zr, V, Rb, SiO2, Li, La, Nd, Cu, As, Ga, Co, Y, Al2O3, Nb	Ba, Cr, Zr, Sr
Carbonaceous Phyllite	Phyllic	Ba, Cu	As, V	Zn, Nd, Se, La, Sm, Ce, K2O, Sc, Eu, Bi, Tb, Ho, Sb, P2O5, Tm, Re, Hg	Y, Pr, Dy, U, S, CaO, Gd	MgO, Fe2O3, Th, W, Na2O, Yb, Pb, Ge, TiO2, Er, Tl, MnO, Lu, In, Ta, Cd, Al2O3	Rb, Nb, Co, SiO2, Ga, Hf, Cs, Sn	Sr, Zr, Ni, Li	Cr
Carbonaceous Phyllite	Potassic	Ba, As	Cu, Zn, V	Y, Co, Pb, Rb, CaO, Dy, Gd, Sc	Se, Er, Sm, Fe2O3, S, Yb, Al2O3, Ho, U, Tb, Tl, Cd, Eu, Na2O, Bi, K2O, Tm, Sb, Lu, MnO, P2O5, In, Re, Hg	Sn, MgO, Ge, Th, Nd, Cs, Pr, Ta, TiO2	Li, Ce, Nb, W, Ga, La, Hf	Zr, Sr, Ni, SiO2	Cr
Carbonaceous Phyllite	Silicification	Ba, As	V, Cu, Zn, Ni, Rb, Sc, Co	W, Se, Cr, CaO, Fe2O3, Sb, Y, Te, S, Ga	Bi, K2O, Dy, Yb, Tl, Er, TiO2, Ho, Tm, Tb, In, MnO, Cd, Re, Lu	Sm, MgO, Cs, Ge, Ta, Sn, Gd, U, Eu, P2O5, Hg, Al2O3	Nd, Li, Nb, Th, Pr, Hf, Pb, Na2O	Zr, Sr, Ce, SiO2, La	
Quartz-chlorite-sericite-garnet schist	Potassic	As, Sr, Cu	Ba, Zr, Ce, Rb, La, Nd, Y	Ni, Pb, Li, Th, Pr, CaO, Nb, Se, W, Co, Ga, Sm, Gd, Sn, Hf, U, Dy, Eu, Cs	SiO2, Er, S, Yb, Tb, Ho, Bi, Tl, Ta, Sb, Ge, Tm, Lu, K2O, P2O5, Cd, MnO, In, Re, Hg, Al2O3	MgO, TiO2, Na2O	Cr, Fe2O3	V, Zn, Sc	
Quartz-chlorite-sericite-garnet schist	Phyllic	Ba, Cu	Cr, Rb, Zn, Zr, Ni, Li, Ce	La, Nd, Th, Pb, Nb, Cs, K2O, Se, Pr, Sm	Y, Sn, Hf, Gd, U, Ga, Dy, S, Tl, Ta, Tm, Ho, Lu, Tb, Bi, Yb, P2O5, MnO, Re, Al2O3	CaO, W, Ge, TiO2, Na2O, MgO, Cd, In, Er, Eu, Sb, Hg	Co, Sc, SiO2, Fe2O3	As, V, Sr	

The results (wt% or ppm) for the carbonatic alteration zone of the carbonaceous phyllite (Fig. 7E) indicates major gains in > 10% of CaO and MgO and major losses in > 100% of Ba, Cr, Zr, and Sr, > 10% of Ni, Ce, Zr, V, Rb, SiO2, Li, La, Nd, Cu, As, Ga, Co, Y, Al2O3, and Nb, and > 1% of Pb, Sc, Th, Pr, Hf, Fe2O3, Sm, Gd, Dy, Cs, Na2O, Yb, U, Er, Sn, K2O, and W. The results (wt% or ppm) for the phyllic alteration zone of the carbonaceous phyllite (Fig. 7F) show major gains in > 100% of Ba and Cu, > 10% of As and V, > 1% of Z, Nd, Se, La, Sm, and Gd, and major losses in > 100% of Cr, > 10% of Sr, Zr, Ni, and Li, and > 1% of Rb, Nb, Co, SiO2, Ga, Hf, Cs, and Sn. The results (wt% or ppm) for the potassic zone of the carbonaceous phyllite (Fig. 7G) present major gains in > 100% of Ba and As, > 10% of Cu, Zn, and V and > 1% of Y, Co, Pb, Rb, CaO, Dy, Gd, and Sc and major losses in > 100% of Cr, > 10% of Zr, Sr, Ni, and SiO2 and > 1% of Li, Ce, Nb, W, Ga, La, and Hf. The results (wt% or ppm) for the silicification zone of the carbonaceous phyllite (Fig. 7H) indicates major gains in > 100% of Ba and As, > 10% of V, Cu, Zn, Ni, Rb, Sc, and Co and > 1% of W, Se, Cr, CaO, Fe2O3, Sb, Y, Te, S, and Ga, and major losses in > 10% of Zr, Sr, Ce, SiO2, and La, and > 1% of Nd, Li, Nb, Th, Pr, Hf, Pb and Na2O. The results (wt% or ppm) for the potassic zone of the GNCX (Fig. 7I) show major gains in > 100% of As, Sr, and Cu, > 10% of Ba, Zr, Ce, Rb, La, Nd, and Y, and > 1% of Ni, Pb, Li, Th, Pr, CaO, Nb, Se, W, Co, Ga, Sm, Gd, Sn, Hf, U, Dy, Eu, and Cs, and major losses in > 10% of V, Zn, Sc, and > 1% of Cr and Fe2O3. The results (wt% or ppm) for the phyllic zone of the GNCX (Fig. 7J) present major gains in > 100% of Ba and Cu, > 10% of Cr, Rb, Zn, Zr, Ni, Li, and Ce, > 1% of La, Nd, Th, Pb, Nb, Cs, K2O, Se, Pr, and Sm, and major losses in > 10% of As, V, and Sr, and > 1% of Co, Sc, SiO2, and Fe2O3.
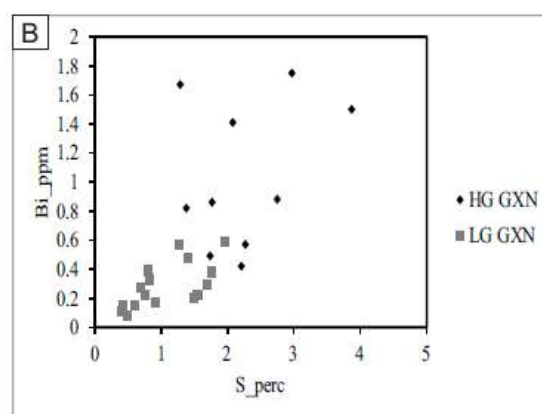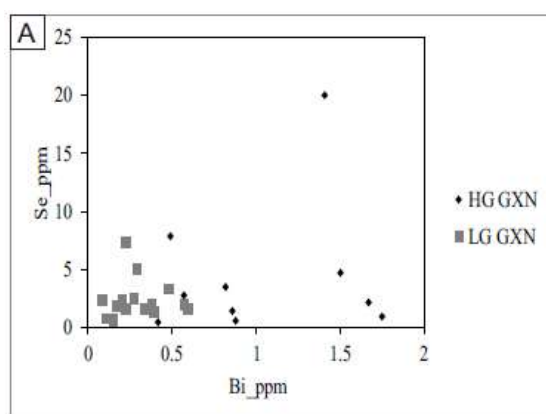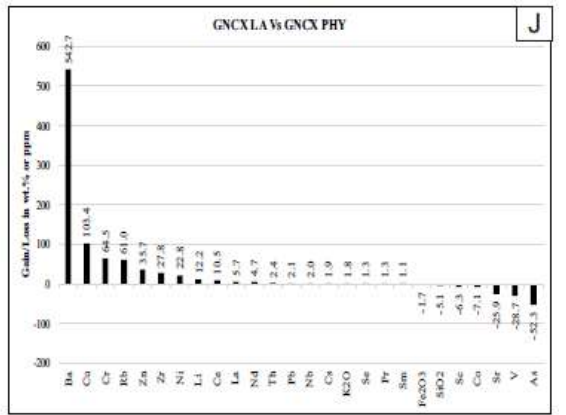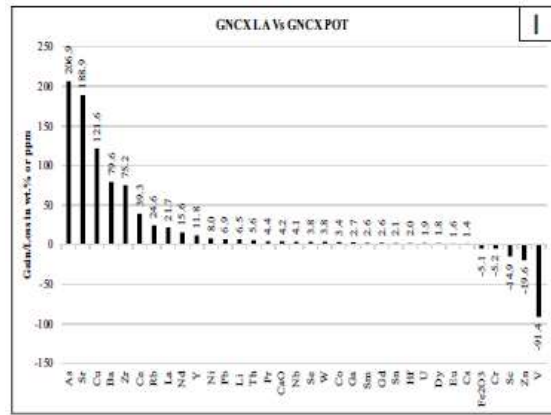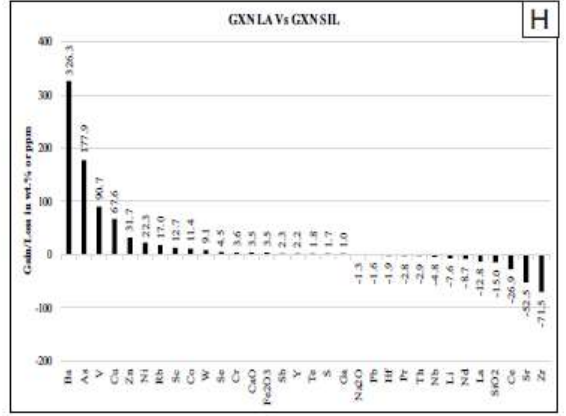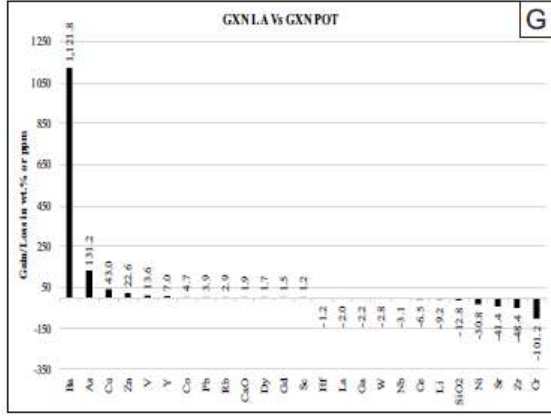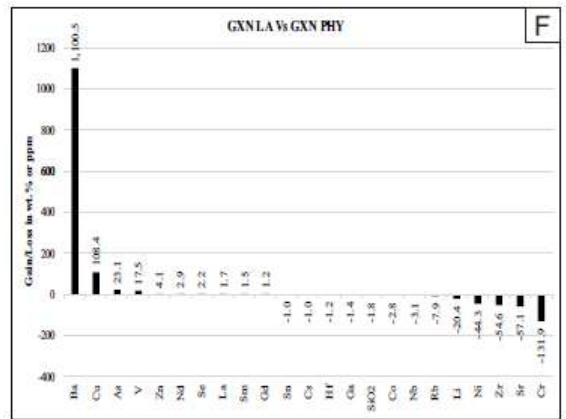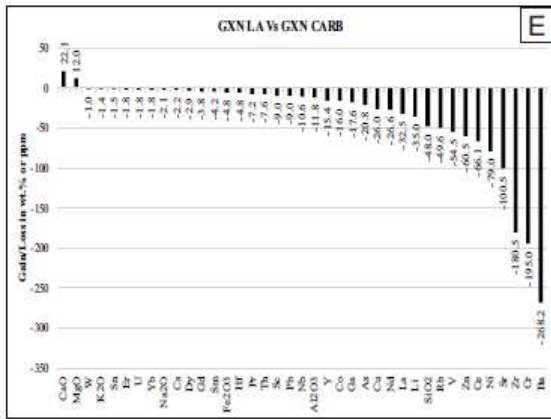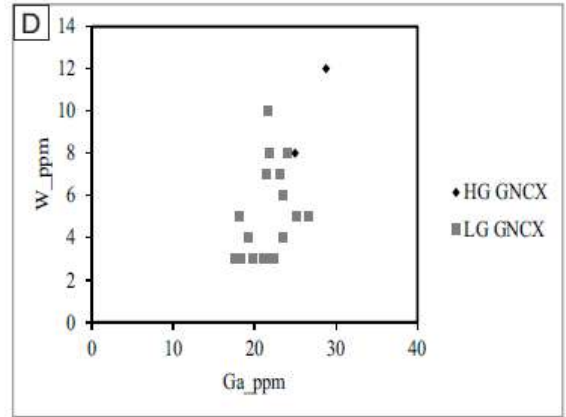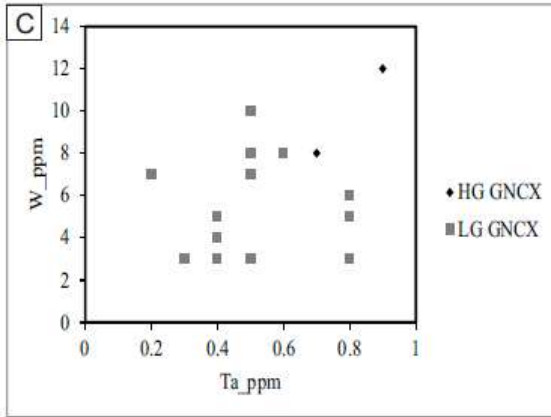
Fig. 8. A) Bi ppm vs. Se ppm and B) S percent vs. Bi ppm plots to discriminate high grade (HG) from no to low grade (LG) carbonaceous phyllite. C) Ta ppm vs. W ppm and D) Ga ppm vs. W ppm plots to discriminate high grade (HG) from no to low grade (LG) quartz-chlorite-sericite-garnet schist (GNCX). E) Gain/loss in wt.% or ppm for GXN Carbonatic halo vs. least altered GXN. F) Gain/loss in wt.% or ppm for GXN Phyllic halo vs. least altered GXN. G) Gain/loss in wt.% or ppm for GXN Potassic halo vs. least altered GXN. H) Gain/loss in wt.% or ppm for GXN Silicification halo vs. least altered GXN. I) Gain/loss in wt.% or ppm for GNCX Potassic halo vs, least altered GNCX. J) Gain/loss in wt.% or ppm for GNCX Phyllic halo vs. least altered GNCX. Abbreviations: CARB = carbonatic halo, GXN = carbonaceous phyllite, LA = least altered, PHY = phyllic halo, POT = potassic halo, GNCX = quartz-chlorite-sericite-garnet schist, SIL = silicification halo.

Major gains in CaO and MgO, minor gains in MnO, and major losses in almost all other bulk oxides in carbonatic zone GXN show the pervasive carbonate alteration over the carbonaceous phyllite. Minor to major gains in K2O in altered GXN and GNCX reflect phyllic (muscovite) and potassic (ferri-biotite) alteration of the least altered host rock. Al2O3 is immobile and therefore does not manifest any notable change due to phyllic or potassic alteration. Major to minor losses and minor gains of SiO2 in altered GXN and GNCX reflect the relative increase in Fe2O3 due to sulfidation and CaO due to carbonate in quartz-carbonate hydrothermal veining and pods, compared to silicification effects. The least altered GXN and GNCX has a quartz-feldspatic matrix which masks the subsequent increase in SiO2 content along hydrothermal alteration zones. Major to minor gains in CaO and MnO in the silification zone of GXN, and the phyllic and potassic zones of GNCX may reflect an increase in almandine garnet, with Ca-rich margins and Mn-rich cores. Overall LOI% increase in all altered GXN and GNCX compared to the least altered samples is related to an increase in micas (bound water OH+), carbonate minerals (CO2), and carbonaceous matter. Overall carbon increase in all altered GXN and GNCX compared to the least altered samples is related to an increase in carbonaceous material contribution by the host rock and also related to pervasive carbonate mineral enrichment (carbonatic zone GXN) or quartz-carbonate hydrothermal veining.

Major gains of Ba in all altered GXN and GNCX may be related to millimeter to centimeter scale quartz-carbonate hydrothermal veins that contain barite. Major to minor gains in S and major gains in Cu in altered GXN (except carbonatic zone GXN) and GNCX reflect an increase in sulfide minerals: arsenopyrite, chalcopyrite, ilmenite, magnetite, pentlandite, and pyrrhotite. Carbonatic, phyllic, potassic and silicification zones of GXN and potassic zones of GNCX show major gains in As due to increase in Aspy content. Major to minor gains in Fe in potassic and silicification zones of GXN reflect an increase in sulfide minerals. Minor gains in TiO2 in silicification zones of GXN may be related to a relative increase in ilmenite and rutile abundance. Major gains of As, Ni, and Co in silicification zones of GXN may account for As-Ni-Co zonations within Aspy3. Spearman rank correlation matrix (Spearman, 1904) of gold with various elements revealed reasonable positive and negative gold correlation values: Bi (0.71), LOI (0.69), Te (0.69), S (0.64), Se (0.61), W (0.6), Cr (0.57), Ga (0.56), CaO (0.54), P2O5 (0.52), TiO2 (0.52), V (0.51), SiO2 (-0.7) for GXN and W (0.75), Sn (0.62), BaO (0.59), Ga (0.58), and Sb (0.52) for GNCX. Minor to major gains in Bi, Se, and Te in the altered GXN samples, especially in the silicification zone of GXN, reflects the good positive

correlation between these elements and gold abundance. Major to minor gains in Ba, W, Ga, and Sn in the potassic GNCX reflects the good positive correlation between these elements and gold abundance.

The least altered Ingá carbonaceous phyllite and its different hydrothermal alteration haloes were normalized to the following worldwide shale references: Average Mud from Queensland (MUQ by Kamber et al., 2005), North American Shale Composite (NASC by Haskin et al., 1968), Post Archean Australian Shale (PAAS by Taylor and McLennan, 1985), Average Shales (AS by Piper, 1974), and European Shales (ES by Haskin and Haskin, 1966). This method allowed for geochemical comparisons between different Ingá carbonaceous phyllites and worldwide known shales. The carbonate alteration zone of GXN is more depleted in REE than worldwide alteration zones and has a different overall character, mainly in regard to major oxides, probably due to the influence of dolomite. The phyllic and potassic alteration zones are enriched in LREE in comparison with worldwide alteration zones, followed by the least altered GXN and then by the silicified GXN. The potassic alteration zone is enriched in HREE in comparison with the other alteration zones, followed by the silicification GXN and then the least altered and phyllic GXN. There is a positive europium anomaly for all carbonaceous phyllites. Compared to all reference shales cited, the Ingá shales have strong enrichment in MgO, CaO, Cr, Ba, and W and strong depletion in TiO_2 and most REE.

Samples of different gold grades were collected in the idiomorphic-arsenopyrite rich carbonaceous phyllite and GNCX and compared in order to understand geochemical controls on gold in the sulfide rich host rock close to the major quartz vein and thrust fault. The high grade GXN was defined as > 5g/t Au and the low to no grade GXN was defined as < 2 g/t Au. The high grade GNCX was defined as > 1 g/t Au and the low to no grade GNCX was defined as < 1 g/t Au. These grades were statistically defined considering all GXN and GNCX Ingá drill core samples analysed for gold by fire assay by the geology and exploration department at the AngloGold Ashanti - Serra Grande Unit. High gold grade GXN samples are very enriched in Au, CaO, LOI, Sn, Sr, Bi, Se, Te, and S in comparison to low or no gold grade samples. High gold grade GNCX samples are very enriched in Au, Ba, Tm, Ni, and S and very depleted in SiO_2 in comparison to low to no gold grade samples. This possibly indicates that there is no direct relation between gold and overall arsenopyrite abundance, with the exception of Arsenopyrite3 (explained in the next section). Binary and ternary plots with a variety of elements and ratios were attempted in order to differentiate the high gold grade from the low to no gold grade in the host rocks. For the carbonaceous phyllite, the most informative plots are the Bi ppm x Se pmm, S percent x Bi ppm, and S percent x P_2O_5 percent (Fig. 7A-B). For the GNCX the most informative plots are the Ta ppm x W ppm and Ga ppm x W ppm (Fig. 7C-D).

Ore Mineralogy and Paragenesis

With regards to ore mineralogy, the paragenetic sequence is composed of Pyrrhotite ± Pentlandite ± Arsenopyrite1 (Stage 1), Arsenopyrite2 (Stage II), Arsenopyrite3 ± Pyrrothite ± Chalcopyrite ± Ilmenite ± Rutile ± Magnetite ± Pentlandite ± visible Au (Stage III). The pyrrhotite

(Stages I and III) has allotriomorphic intrafoliar shape oriented along S2 foliation. Pyrrhotite is <0.003 to 1.32 mm in size, with abundances varying from < 1% to 8%. Pyrrothite (Po) commonly occurs as inclusions, filling fractures, or along Aspy3 margins. Po rarely occurs as inclusions in garnet, where it fills fractures or marks crystal margins. Po commonly presents chalcopyrite and rarely presents ilmenite along crystal margins and as inclusions. Magnetite inclusions and pentlandite flames commonly occur in Po.

Ilmenite is oriented along S2 foliation, has an idiomorphic rod shape, and is commonly disseminated as free crystals that are <0.003 to 0.173 mm in size, with abundances varying from < 1% to 2%. Ilmenite rarely occurs as inclusions or along the margins of pyrrhotite (Stages I and III) and as inclusions in zoned garnet and Aspy2 and Aspy3. Rarely contain magnetite inclusions. Rarely present partial alteration to rutile. The chalcopyrite has allotriomorphic shape and is randomly oriented. It is < 0.003 to 0.233 mm in size, with abundances varying from < 1% to 1%. It occurs along crystal margins and as inclusions in pyrrhotite (Stages I and III) and in margins, filling fractures and as inclusions in Aspy2 and Aspy3. Rarely occurs as free crystals, along ilmenite margins, in association with rutile, in hornblende fractures, or as inclusions in zoned garnet and in zoned garnet fractures.

The rutile is randomly oriented, has an idiomorphic shape, and is 0.1 to 3 mm in size, with abundances varying from <1% to 1%. Rutile occurs as free crystals in quartz-carbonate venulations associated with Aspy2, Aspy3, and visible gold. Where altered from ilmenite, it has allotriomorphic shape and sub-millimeter size with an abundance of < 1%. Magnetite occurs as sub-millimeter rounded inclusions in Aspy2 and Aspy3, Po (Stages I and III), and ilmenite crystals, with an abundance of < 1%. Pentlandite occurs as sub-millimeter irregular flames in pyrrhotite crystals (Stages I and III), with abundance of < 1%.

Visible gold is randomly oriented, has an allotriomorphic shape, and is > 0.001 to 0.825 mm in size. It occurs in the mineralized zone mainly as free crystals in the basal level of the major quartz vein (Fig. 5G). In the carbonaceous phyllite, visible gold occurs mainly in the VQZ hanging-wall and rarely in the footwall. Gold occurs as free crystals in the matrix near the contact with biotite, sericite and carbonaceous matter (Fig. 5H) and rarely on rutile and pyrrhotite (Stage III) margins (Fig. 5K and 5L). Visible gold commonly occurs as inclusions, filling fractures or in margins of Aspy3 in the carbonaceous phyllite (Fig. 5I and 5J). Visible gold rarely occurs as free crystals in the GNCX in the footwall of the VQZ or as inclusions, filling fractures or in margins of Aspy3 associated with secondary quartz veins that crosscut GXN and GNCX.

Arsenopyrite Characterization

Three main arsenopyrite types have been defined at Ingá orebody in paragenetic sequence from arsenopyrite 1 (Aspy1) to arsenopyrite 3 (Apsy3):

Aspy1 occurs in the carbonaceous phyllite and GNCX, oriented along S2 foliation. It has allotriomorphic shape, is porous, and is 0.004 m to 19 mm in size. Aspy1 is commonly associated with symmetric to asymmetric strain shadows. Aspy1 is rarely associated with pyrrothite (Stage I) margins. No SEM, EMP, and LA-ICP-MS analysis were done in this type of arsenopyrite for the present work because its zones of occurrence have no relevant grade. Further studies shall consider the geochemistry of Aspy1 for comparison with Aspy2 and Aspy3.

Aspy2 and Aspy3 (Fig 9A-J) occur until three meters adjacent to VQZ, crosscutting the silicification halo of the carbonaceous phyllite, and until within one meter of secondary quartz veins, crosscutting GXN and GNCX. In gallery scale the Aspy2 and Aspy3 were only observed in the host rock in the hanging-wall of the major quartz vein. It is impossible to separate both by naked eye, so microanalysis is necessary (i.e. SEM, EMP, LA-ICP-MS). It is randomly oriented, has a zonated idiomorphic shape, and is 15 mm to 5 cm in size. Cruciform twins are common. It is associated with pyrrothite (Stage III) and chalcopyrite on or near margins, in fractures, or as inclusions. Magnetite (common) and ilmenite (rare) occur as inclusions. It is rarely associated with rutile. Amorphous ankerite rarely occurs in Aspy2 and Aspy3 fractures and margins. The differences between Aspy2 and Aspy3 include textures and chemical zonation. Aspy2 makes up the core of the idiomorphic Aspy crystal and is richer in S. Aspy3 occurs along the margins and fractures of Aspy2 crystals, forming irregular inclusion-rich margins with a sieve texture. Aspy3 presents higher concentrations of As-Ni-Co than Aspy2, with random Ni-Co zonations as attested by EMP (Fig. 9G-H). Visible gold concentrates only in Aspy3, along its margins, fractures (two sets), or as inclusions (Fig. 5I and 5J, Fig. 8I). Table 6A shows that Aspy2 (n=65) is EMP geochemically characterized by wt% S (19.02-22.98; Avg 21.29), As (42.18-46.63; Avg 44.26), Ni (0.05-0.62; Avg 0.17), Co (0.03-0.78; Avg 0.11), and Fe (32.61-35.24 wt%; Avg 34.56). Aspy3 (n=48) is EMP geochemically characterized by wt% S (18.7-20.73; Avg 19.62), As (45.41-47.47; Avg 46.47), Ni (0.05-3.97; Avg 0.51), Co (0.02-0.48; Avg 0.17), and Fe (29.76-34.78; Avg 33.52). Two arsenopyrite types have been reported by Fortes (1996) in the Mina III orebody at the same stratigraphic level, after observations in SEM of S and As geochemistry, which approximately correspond to Aspy2 and Aspy3 of the present paper.

Table 6a. Element weight (%) by EMP and Percent Change of Median
Major Elements Values for Idiomorphic Arsenopyrites from Ingá
orebody Lower Zone.

Arsenopyrite type		Fe	Co	Ni	As	S
Average detection limit		0.04	0.01	0.01	0.12	0.02
Aspy2	Mean	34.56	0.11	0.17	44.26	21.30
n = 65	Median	34.69	0.06	0.12	44.20	21.45
	Sd	0.37	0.08	0.10	0.72	0.59
	Min	32.61	0.03	0.06	42.18	19.02
	Max	35.24	0.78	0.63	46.63	22.98
Aspy3	Mean	33.52	0.18	0.52	46.48	19.63
n = 48	Median	33.72	0.12	0.35	46.55	19.59
	Sd	0.53	0.11	0.38	0.39	0.25
	Min	29.76	0.03	0.06	45.41	18.70
	Max	34.78	0.49	3.97	47.47	20.73
Mean (R-C)/C (%)		-3.01	60.79	201.65	5.01	-7.85
Median (R-C)/C (%)		-2.80	116.52	199.53	5.31	-8.69

Table 6b. Trace Element Concentrations (ppm) by LA-ICP-MS and Percent Change of Median Trace Elements Values for Idiomorphic Arsenopyrites from Ingá Orebody Lower Zone.

Arsenopyrite type		Au	Re	Cr	Bi	Te	Sb	Se	Co	Ni	Ag	Mo	Pb	Zn	Cu	V	Cd	W	Sn	In	Pr	Pd	S	Fe	As
Average detection limit		0.50	0.50	0.50	0.50	0.50	0.50	0.50	0.50	0.50	0.50	0.50	0.50	0.50	0.50	0.50	0.50	0.50	0.50	0.50	0.50	0.50	0.50	0.50	0.50
Aspy2	Mean	0.97	0.67	4.54	0.35	165.47	56.71	39.33	616.89	856.98	0.03	1.33	1.53	4895.18	110.99	2.47	12.21	0.75	0.32	0.10	0.00	0.08	85979.17	168786.80	5539.61
n = 9	Median	0.42	0.69	4.46	0.38	170.10	45.90	35.33	472.69	724.85	0.02	0.86	1.16	120.82	71.52	2.41	0.05	0.23	0.32	0.08	0.01	0.06	72894.37	135277.65	4167.74
	Sd	0.76	0.15	0.43	0.20	53.78	27.34	12.15	234.70	297.56	0.02	0.89	0.84	8279.11	81.27	0.27	21.62	0.78	0.04	0.05	0.00	0.08	19855.16	63354.15	2434.90
	Min	0.16	0.47	3.54	0.06	36.27	19.63	24.56	384.94	517.07	0.00	0.05	0.35	26.63	38.30	2.11	0.00	0.12	0.23	0.05	0.00	0.00	64253.61	106614.63	2793.98
	Max	2.31	1.04	5.36	0.92	287.60	112.87	62.29	1003.06	1389.09	0.06	3.33	4.45	42151.16	476.70	3.40	109.51	2.69	0.41	0.24	0.01	0.34	123214.09	280129.34	9628.71
Aspy3	Mean	1.01	0.58	22.11	21.54	166.97	93.55	219.78	1005.35	2232.27	0.14	0.22	33.48	55.85	11.93	18.14	0.34	0.91	1.83	0.38	14.38	0.20	22638.01	236491.63	29944.06
n = 9	Median	0.83	0.23	22.72	15.63	139.80	86.50	218.00	702.80	1594.00	0.16	0.14	7.72	32.74	5.53	7.58	0.18	0.66	1.03	0.34	0.01	0.17	9958.00	188100.00	26210.00
	Sd	0.65	0.48	8.72	17.44	48.35	47.87	62.61	399.55	1054.87	0.08	0.19	40.16	48.87	9.53	17.83	0.28	0.64	1.24	0.19	22.35	0.15	22350.24	79403.72	11686.19
	Min	0.06	0.09	3.41	0.20	119.30	15.66	34.95	552.80	934.50	0.00	0.00	0.58	2.87	4.60	2.21	0.00	0.17	0.33	0.05	0.00	0.00	6442.00	113824.71	4096.50
	Max	2.18	1.75	44.35	63.32	323.00	191.00	383.10	1986.00	4537.00	0.28	0.87	161.90	165.80	51.41	73.57	0.90	2.69	6.92	0.78	101.50	0.44	123214.09	427100.00	56490.00
Mean (R-C)/C (%)		3.23	-13.65	387.63	6054.19	0.90	64.96	458.84	62.97	160.48	na	-83.49	2094.73	-98.86	-89.25	634.12	-97.24	20.64	473.82	276.71	308059.52	na	-73.67	40.11	440.54
Median (R-C)/C (%)		99.94	-67.10	409.15	4051.48	-17.81	88.44	517.03	48.68	119.91	na	-83.63	566.43	-72.90	-92.27	214.72	278.23	187.83	217.47	301.85	50.00	na	-86.34	39.05	528.88

Abbreviations: sd = standard deviation; na = do not apply; C = Aspy2; R = Aspy3

LA-ICP-MS spot analysis and element mapping were performed on Aspy2 and Aspy3 with a focus on their cores, margins, and fractures. Spatial decoupling between elements reflects, in part, geochemically distinct arsenopyrite domains. Table 6B show that, overall, Aspy2 has (median) > 100 ppm of Fe, S, As, Ni, Co, Te, and Zn, > 10 ppm of Cu, Sb, and Se, > 1 ppm of Cr, V, and Pb, and < 1 ppm of Mo, Re, Au, Bi, Sn, W, and Cd, while Aspy3 has overall > 100 ppm of Fe, As, S, Ni, Co, Se, and Te, > 10 ppm of Sb, Zn, Cr, and Bi, > 1 ppm of Pb, V, Cu, and Sn, and < 1 ppm of Au, W, Re, Cd, and Mo. Elements Pd and Ag all had analysis below the detection limit, Pr and In had only two analyses above the detection limit and Au, Bi, Mo, Cd, W, and Sn had significant data below the detection limit. Table 6B compares the median and geometric mean trace element concentrations of Aspy3 compared to Aspy2. Aspy3 has > 200% positive change (median) of Bi, Pb, As, Se, Cr, Cd, Sn, and V, > 100% of W and Ni, > 30% of Au, Sb, Co, and Fe and < 10-100% negative change (median) of Cu, S, Mo, Zn, Re, and Te compared to Aspy2. Box plot analysis (Fig. 10) show marked low S, Cu, and Mo concentrations and marked high As, Cr, Bi, Se, Co, Ni, Pb, V, and Sn concentrations in Aspy3 compared to Aspy2. Probability plots, split probability plots, scaled coordinates (minimum zero to maximum one), and spider plot (Aspy3 compared to Aspy2), indicate relative high concentrations of As, Bi, Cr, Se, Ni, and Sn in Aspy3 compared to Aspy2 and relative high concentrations of S, Cu, and Mo in Aspy2 compared to Aspy3.
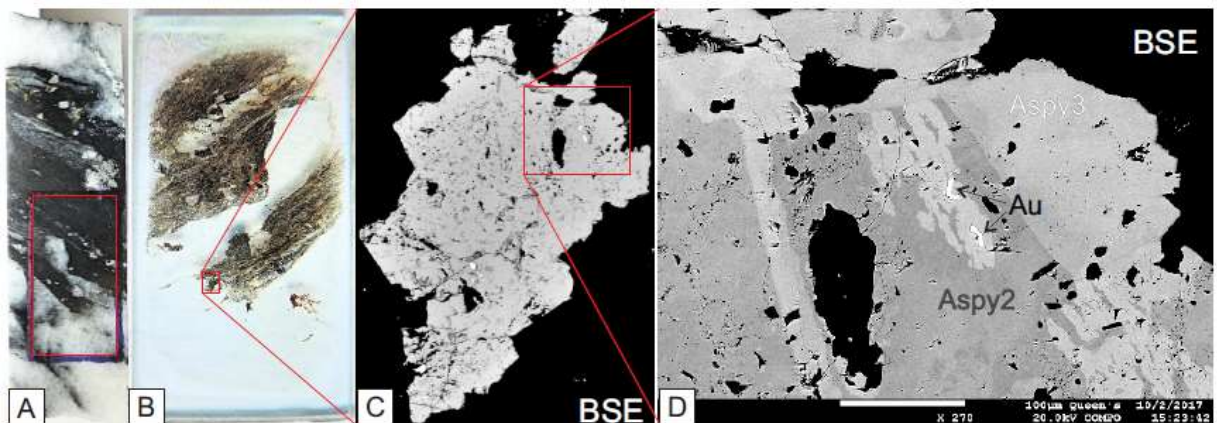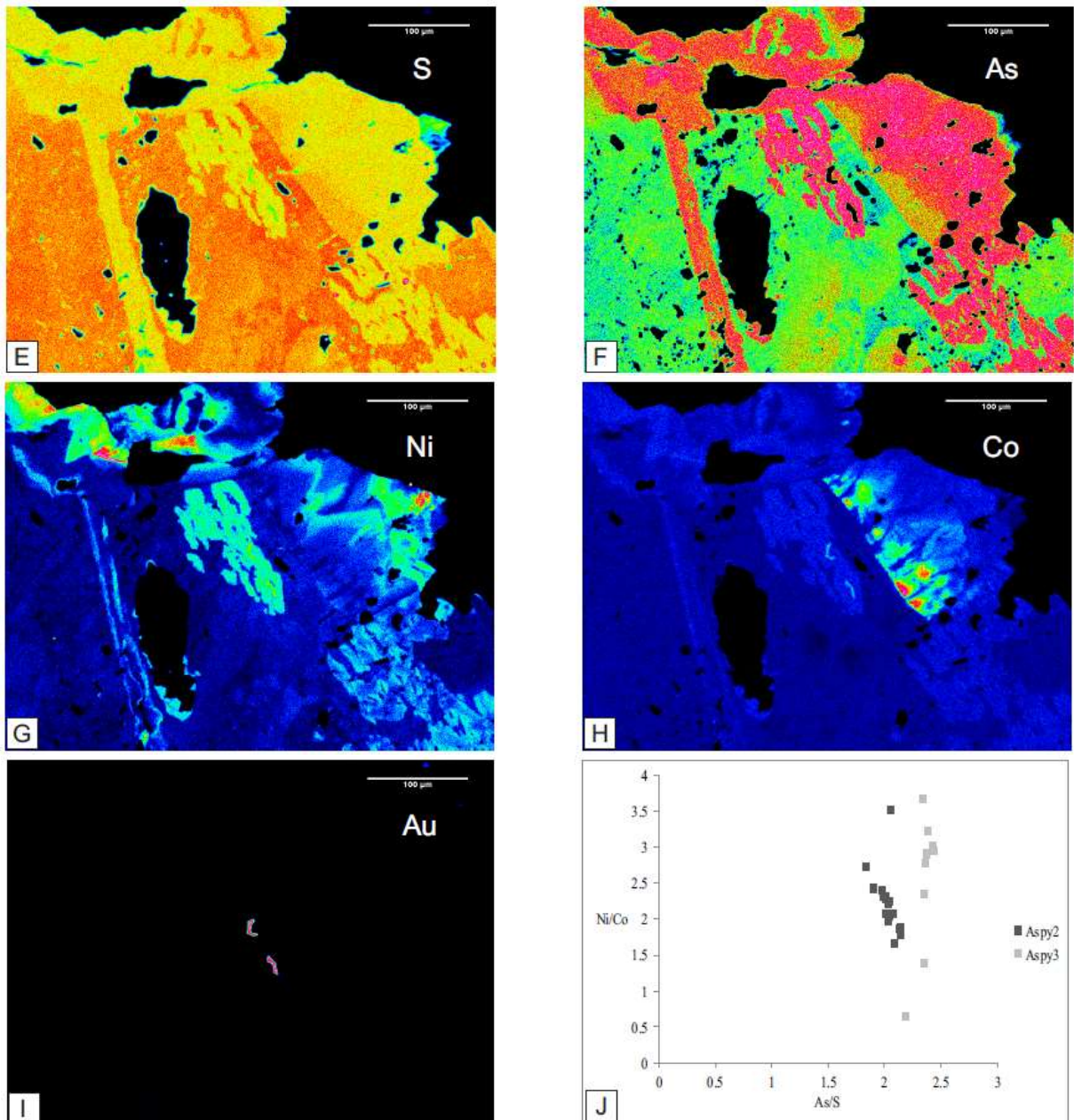
Fig. 9. A) Aspy-rich carbonaceous phyllite in the hanging-wall of the major quartz vein. B) Thin section of A highlighted area. C) BSE image zoom on Aspy crystal of thin section in B. D) BSE image zoom on Aspy crystal in C. Light gray color is Aspy3 and dark gray color is Aspy2. See visible gold crystal in Aspy3. E) S element mapping. F) As element mapping. G) Ni element mapping. H) Co element mapping. I) Au element mapping. J) As/S vs. Ni/Co differentiation plot in element weight percent for arsenopyrite. Abbreviations: Aspy = arsenopyrite, Au = gold.

Arsenium, bulk element for Aspy3 recognition in margins and fracture zones, show marked positive Pearson correlation with Se, Ni, Fe, Cr, Sb, Co, Bi, Te, Sn, and V. Elements As, Fe, Co, and Ni show a similar behavior, as detected by the EMP analysis. Sulfur, bulk element for Aspy2 recognition in core zones, shows marked positive Pearson correlation with Cu, Re, W, Mo, Zn, and Cd. Aspy2 is then relatively depleted in most trace elements and base metals, while Aspy3 is relatively enriched uniformly in some and erratic in others, showing systematic variations in selected trace elements. This variability may indicate that these elements occur, at least in part, as nanoparticles. Due

to its nugget effect, both Aspy2 and Aspy3 show weak positive Pearson correlation gold values, with Aspy3 values (<0.5 – 2.18 ppm) 43% higher than Aspy2 values (<0.5 – 2.31 ppm). Of the nine spot analyses in Aspy2, four (44%) have gold concentrations above the detection limit (> 0.5 ppm), showing that invisible gold could exist as submicroscopic particles or could be present non-uniformly as a solid solution within the host arsenopyrite lattice. Aspy crystals possess then a complex reworking story characterized by variable precious and base metal enrichment. Outliers concentrations observed in the data and the box plot analyses indicate the presence of micro-inclusions in the host arsenopyrite containing Pb (galena), Zn (sphalerite), Cu (chalcopyrite), S (sulfides), V, Cd, Te, Mo, and Sn. Cadmium shows a strong relationship with Zn in PCA plot analysis (PC3, 2.8 eigenvalue, 0.66 scaled coordinates), indicating possible high Cd content in sphalerite micro-inclusions as described by Berner et al. (2013). Tellurim could be related to the presence of Au-Bi-Mo telluride micro-inclusions. Element mapping was done on three arsenopyrite crystals of thin section 55-16. Figure 11 shows an example from Aspy3, which has marked high concentrations of Au, Ag, Bi, and Ni and slightly marked high concentrations of Pb, Co, Te, Se, and Re, while Aspy2 shows marked high concentrations of Mo and Sb and slightly marked high concentrations of Zn and W. There are two distinct fracture sets in arsenopyrite, in which a later, more developed set crosscut a previous, less developed set. Both are gold rich and contain the same elemental assemblage as Aspy3, making it impossible to identify any difference regarding mineralogy and geochemistry. There are elevated concentrations of trace elements in the fractures (Aspy3) compared to the inclusion-free undeformed arsenopyrite zones (Aspy2).
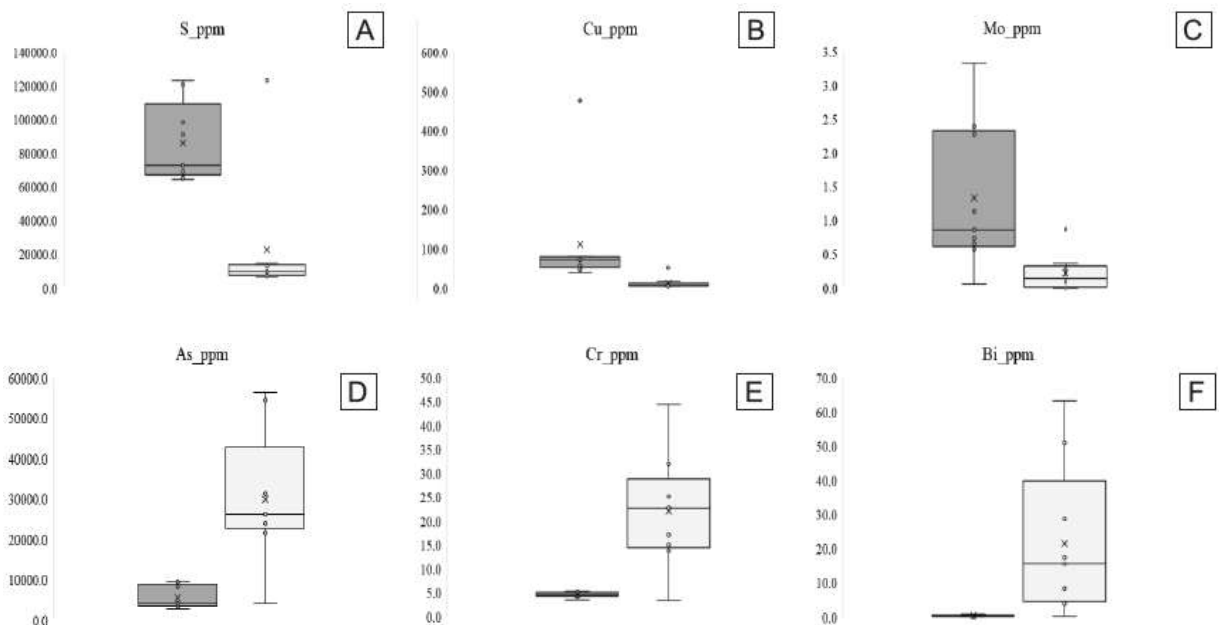
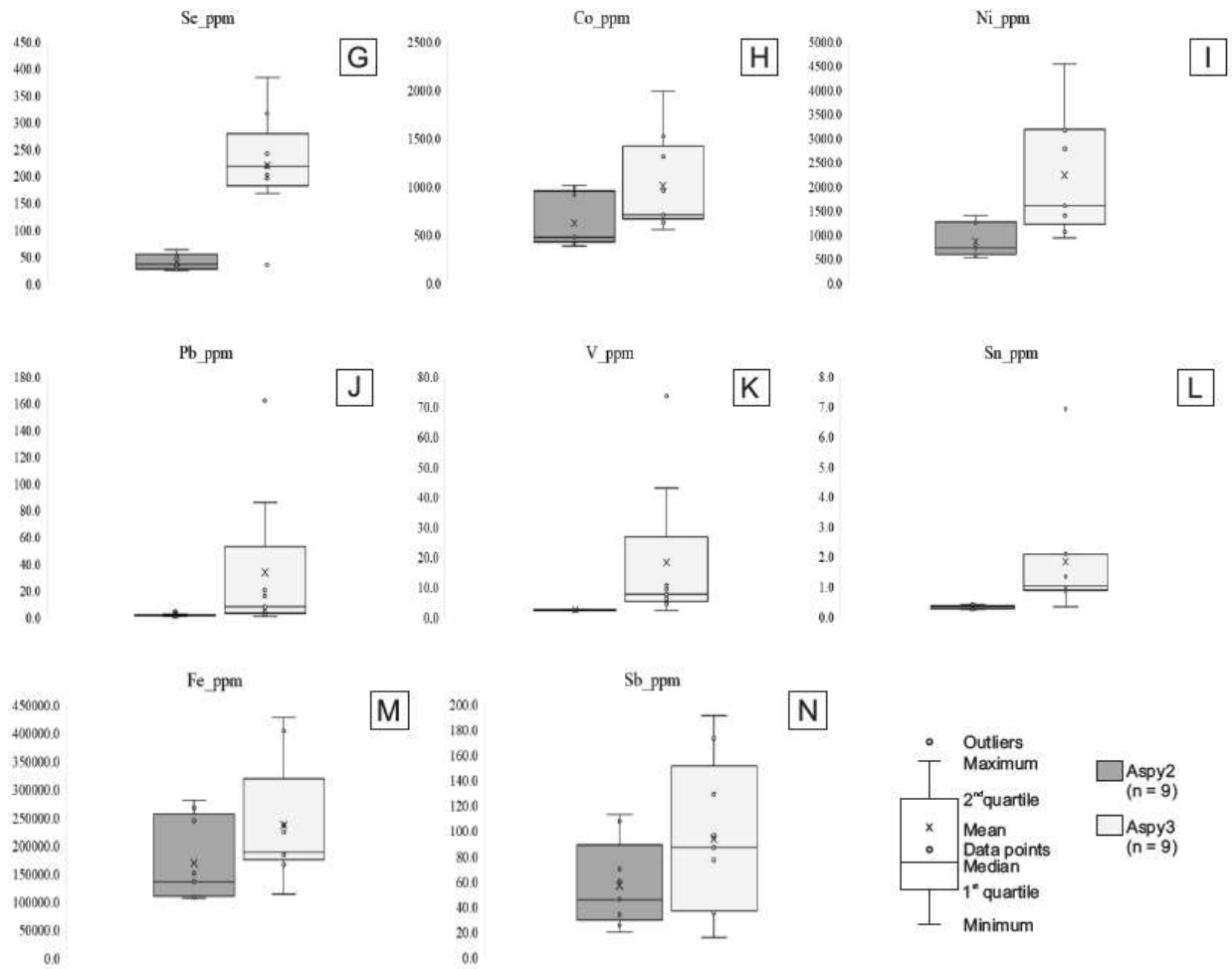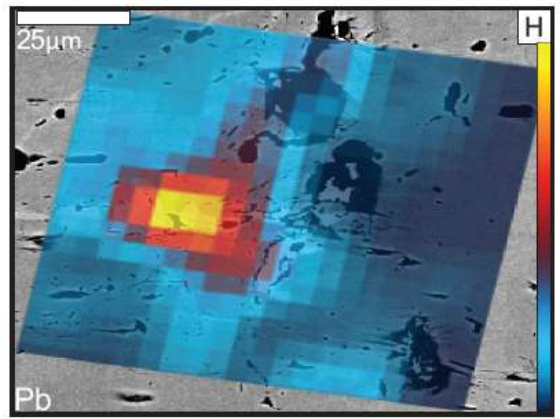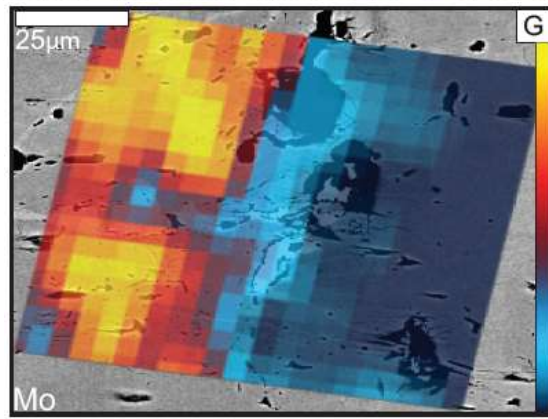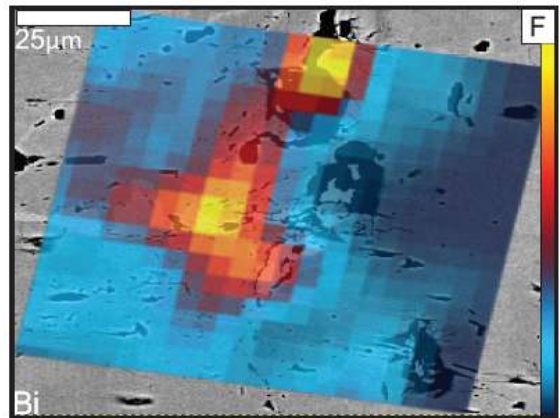Fig. 10. LA-ICP-MS box plot spot analysis. Consider 0.5 ppm as detection limit for all elements. A) S ppm. B) Cu ppm. C) Mo ppm. D) As ppm. E) Cr ppm. F) Bi ppm. G) Se ppm. H) Co ppm. I) Ni ppm. J) Pb ppm. K) V ppm. L) Sn ppm. M) Fe ppm. N) Sb ppm.
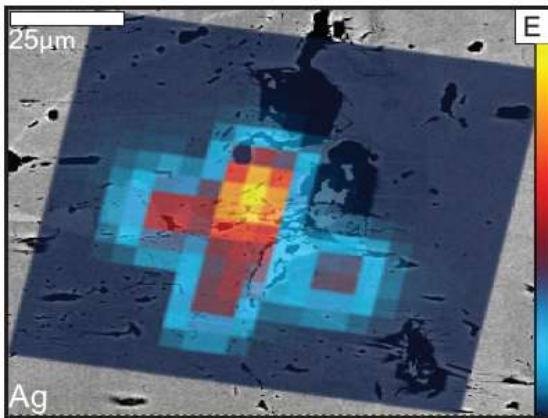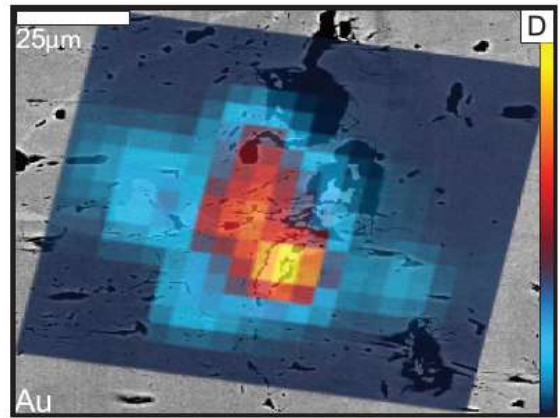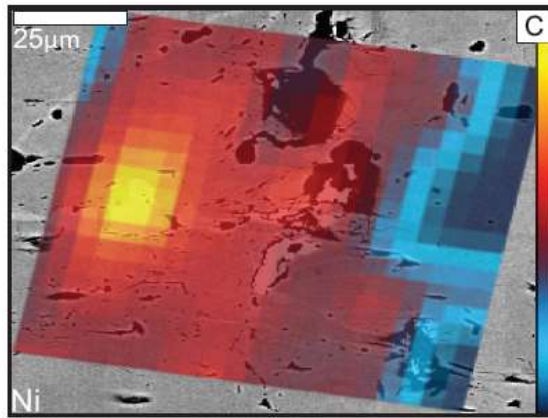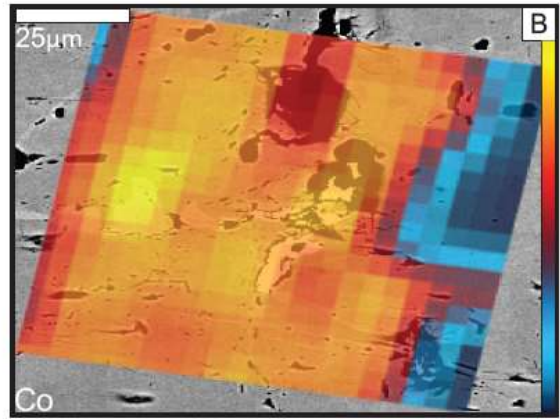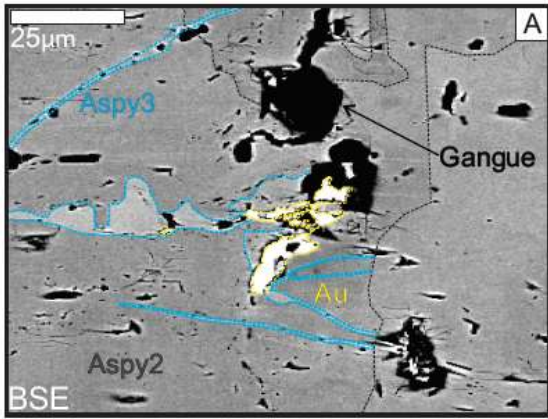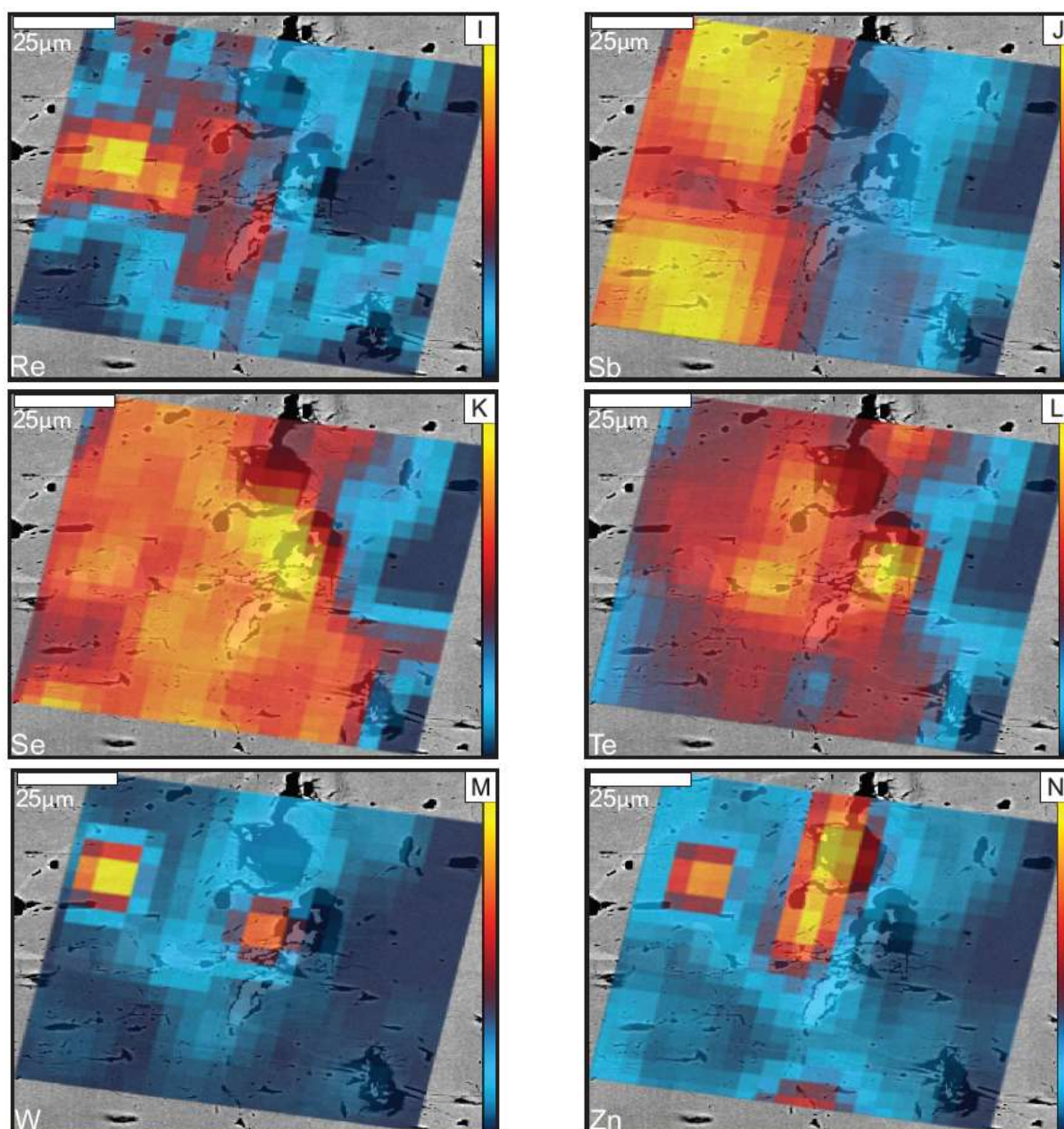
Fig. 11. LA-ICP-MS element mapping images with minimum and maximum cps represented in the colored scale. A) BSE image with indication of mineralogy. B) Co element mapping $(0 – 320 \times 10^3$ cps). C) Ni element mapping $(0 – 180 \times 10^3$ cps). D) Au element mapping $(0 – 2.2 \times 10^6$ cps). E) Ag element mapping $(0 – 1.0 \times 10^6$ cps). F) Bi element mapping $(0 – 140 \times 10^3$ cps). G) Mo element mapping $(0 – 800$ cps). H) Pb element mapping $(0 – 70 \times 10^3$ cps). I) Re element mapping $(0 – 320$ cps). J) Sb element mapping $(0 – 120 \times 10^3$ cps). K) Se element mapping $(0 – 4500$ cps). L) Te element mapping $(0 – 18 \times 10^3$ cps). M) W element mapping $(0 – 3200$ cps). N) Zn element mapping $(0 – 5500$ cps). Abbreviations: cps = counts per second.

Discussion

Arsenopyrite and possible gold remobilization

The arsenopyrite texture and geochemical zonation is directly linked to the gold abundance in the carbonaceous phyllite and GNCX adjacent to the major quartz vein, as well as the gold-rich major quartz vein emplacement. Archean basins, once formed, represent zones of long-lived structural weakness and remain favorable settings for gold mineralization and/or remobilization during

subsequent reworking (Lawley et al., 2015). Gold, if present within Aspy, is often heterogeneously distributed within compositionally zoned grains (Morey et al., 2008). Gold poor cores and enrichment along growth zones toward grain margins were documented by Johan et al. (1989), Fleet et al. (1989), Mumin et al. (1994), Oberthur et al. (1997), Fleet and Mumin (1997), Genkin et al. (1998), and Cook et al. (2013). Gold redistribution by remobilization from the sulfide lattice and reconcentration (as inclusions of gold or electrum) within or near the parent mineral is recognized as an important process (e.g., Larocque et al., 1995). Remobilization may be recognized in gold ores, which have developed during a sequence of fluid inputs and prolonged fluid infiltration at temperatures consistent with greenschist facies metamorphism or above or below, generally under oriented strain (Cook et al., 2013). Oscillatory zoning with respect to the essential elements (Fe, As, and S) and with respect to Co and Ni, common minor constituents in arsenopyrite, has been previously reported (Cathelineau et al., 1989; Morey et al., 2008, Cook et al., 2013).

The Aspy2 and Aspy3 crystals are concentrated within the selvages of the major quartz vein, showing its late hydrothermal character, in comparison to the early Aspy1 that is wrapped by the S2 foliation commonly showing strain shadows. In gallery scale, only the major quartz vein hanging-wall contains carbonaceous phyllite rich in Aspy2 and Aspy3. Gold-rich Aspy3 concentrated on late arsenopyrite crystal fractures and inclusion-rich sieve-textured boundaries are in contrast with gold-poor Aspy2 concentrated in the arsenopyrite interior. This contrast is possibly related to post crystallization gold enrichment along late crystal fractures and selective alteration toward the margins, forming Aspy3. This post crystallization fluid-assisted remobilization of precious and base metals possibly occurred during successive deformation events (Tomkins and Mavrogenes, 2001; Wagner et al., 2007; Morey et al., 2008; Thomas et al., 2011; Cook et al., 2013; Lawley et al., 2015; Fougerouse et al., 2017; Gourcerol et al., 2018). Inclusion-rich sieve-textured Aspy3 domains and fracture networks are possibly enriched in precious and base metals and contain clusters of native gold, pyrrhotite (Stage III), chalcopyrite, magnetite, and ilmenite inclusions. Geochemically anomalous domains are demarcated by trails of mineral inclusions and/or embayed crystal boundaries. These textures suggest that Aspy2 and Aspy3 crystals possess complex reworking histories characterized by variable precious and base metal enrichment. This grain boundary-fracture association suggests an external influence and given the lack of other mineral phases containing arsenium and sulphur, introduction of a late hydrothermal fluid is thought to be responsible for this association (Morey et al., 2008). This fluid would penetrate along grain borders, possibly promoting fracturing and facilitating reaction progress. The resulting Aspy3 rims are thus considered to be alteration rims.

Zoning patterns and intermediate compositions between Aspy2 and Aspy3 suggests constant changes in fluid pressure and fluid flow regime. The intermediate compositions are attested by the gray shading in BSE imaging in SEM and EMP. This gray shading has previously been attributed to Aspy growth zoning and the substitution of As for S within Aspy crystals in response to changing conditions, as attested by experimental studies (Kretschmar and Scott, 1976; Sharp et al., 1985;

Carpenter, 2003; Lawley et al., 2015). Typical Aspy2 and Aspy3 are the end members of intermediate compositions. Progressive mineral precipitation during wall-rock alteration by hydrothermal fluid would result in a gradual compositional change of precipitating minerals. These observations support a model for Au distribution in Ingá arsenopyrite involving possible grain-scale remobilization during deformation and subsequent Au reconcentration at or close to grain margins and within intragranular microfractures. Possibly remobilized gold must have originally been incorporated within sulfides and was later released, rather than being supplied at the time of brittle-ductile fracture. Release of gold possibly took place in response to deformation. Some remobilization of gold from sulfides to free gold accumulations might occur during F2 folding in the Crixás greenstone belt (S. Ulrich, pers. commun., 2014). Such a major event in its late brittle-ductile stages was probably responsible for the possible remobilization of an inferred invisible gold from Aspy2 to form visible gold in Aspy3.

It can be difficult to resolve the timing of gold incorporation in sulfides of the Ingá with a single orogenic gold deposit model, because superimposed, later stages of deformation cause Au to be released from arsenian pyrite or arsenopyrite (Large et al., 2011). Gold was released either into the ore fluid or, more likely, was concentrated at or close to grain boundaries. Sulfide crystallization could have occurred before veining and the main phase of Au deposition, during the same stage but later, or after vein formation. Sulfides may also have been formed throughout (i.e., at multiple different stages) the mineralization event. The variation in grain size, morphology and geochemistry of arsenopyrite crystals at Ingá indicates at least three stages of arsenopyrite deposition: Aspy1 (early hydrothermal), Aspy2 (late hydrothermal) and Aspy3 (later hydrothermal-remobilization). Considering that hydrothermal sulfides occur at the margin of reworked veins and also disseminated in wall rock, it is most likely that they formed at the end of a mineralization event after the fluid became supersaturated and precipitated the majority of gold. Fluids were, nevertheless, Au-bearing at the time of sulfide formation and available Au was scavenged by, and possibly preferentially partitioned into Aspy2. Subsequent deformation possibly released Au, giving rise to a population of visible gold grains in the sulfides and adjacent areas, contributing to the overall Au budget. The observed Au enrichment toward the grain margins and, critically, the presence of nano to micro-pores in the same parts of the grain, indicate that Au release could have been assisted by late percolating fluids via reactions between preexisting arsenopyrite, leading to partial dissolution. This reinforces the idea that Au release is activated by infiltration under deformation (Pokrovski et al., 2002; Cook et al., 2009; Sung et al., 2009; Ciobanu et al., 2012) and not solid state diffusion as explained by Tomkins and Mavrogenes (2002). In the Ingá orebody, fluid infiltration along fractures was probably critical for Au remobilization.

There is a general consensus that indicates a positive correlation between Au and As in arsenian pyrite (Cook and Chrysssoulis, 1990; Simon et al., 1999b; Large et al., 2009), which may be applied to arsenopyrite. As and Co composition show an inverse relation with Fe, indicating the replacement of Fe by Co in the Aspy structure. A number of studies show that Au in solid solution

exchanges for Fe sites within arsenopyrite and pyrite (Wu and Delbove, 1989; Fleet and Mumin, 1997; Tarnocai et al., 1997), promoting an inverse correlation. Aspy EMP and LA-ICP-MS element maps and spot analyses reported herein provide possible evidence for relatively late gold enrichment that is, in part, linked to the post crystallization history of early sulfides. Fluid assisted and/or deformation driven sulfide dissolution likely mobilized these elements from older sulfide minerals. Recrystallized arsenopyrite domains (i.e. sieve-textured crystal boundary Aspy and domains adjacent to fractures) are enriched in precious and base metals as attested by LA-ICP-MS analysis on Aspy3. Trace elements in arsenopyrite occurs as (1) lattice substitution (i.e. in solid solution) or (2) inclusions of nanoparticles or visible inclusions (Huston et al., 1995; Deditius et al., 2011). The presence of As in arsenopyrite, in substitution for As in the S site, distorts the arsenopyrite lattice, making it easier for large cations (i.e. Au, Pb, Bi) to be incorporated into the arsenopyrite, and at higher concentrations, these elements are incorporated in micro-inclusions of Bi-Pb-Au that contain tellurides, selenides, or galena enriched in Bi, Au, Se, and Te or Au-Sb-Te phases (Gregory et al., 2016). These micro-inclusions occur at low-strain micro-textural sites and/or are present as clusters. Mineral inclusion clusters (e.g., sieve-textured Aspy) and variably replaced early sulfide phases are microtextures typical of metamorphosed deposits (Tomkins and Mavrogenes, 2001 and Lawley et al., 2015). We interpret that the two distinct set of fractures observed, with the same geochemical and mineralogical assemblage, actually belong to one conjugated fracture set, with the same importance regarding gold remobilization and mineralization, both considered Aspy3 zones. Our observations are consistent with and complement those of Morey et al. (2008) and Cook et al. (2013), who also considered textural and grain-scale geochemical evidence in arsenopyrite for cycles of hydrothermal infiltration, alteration, and remobilization during evolution of a gold ore. Two combined processes could explain the overall lower trace element content of Aspy2 compared to Aspy3: (1) trace elements were depleted in the early hydrothermal fluids compared to the evolved, (2) trace elements were present in the early fluids but incorporated into other minerals (such as chalcopyrite or pyrrhotite) or formed accessory phases (e.g. such as Au tellurides, As-bearing minerals).

Aylmore and Graham (1992) concluded that a high percentage of the gold occurs either as fine inclusions or is located in a lattice defect or interstitial site of arsenopyrite. Previous studies concluded that invisible gold can occur in solid solution within the host crystal lattice or exist as < 1 μm, submicroscopic particles (Cabri et al., 1989; Cabri et al., 2000; Genkin et al., 1998; Simon et al., 1999a; Palenik et al., 2004; Morey et al., 2008). In ores subjected to deformation and/or hydrothermal alteration after formation, the greater part of the invisible gold incorporated in sulfides at the time of initial precipitation, if any, will be expelled from the sulfide lattice (e.g. Mumin et al., 1994; Large et al., 2007, 2009, Cook et al., 2013). The chemical state of gold in solid solution is complex, with studies suggesting an oxidation state of Au^{3+} (e.g., Arehart et al., 1993) or a combination of Au^0 and Au^{1+} (e.g., Simon et al., 1999a and Cabri et al., 2000). Thus the speciation of gold in arsenopyrite is not well understood, in spite of intense studies over the last years (Cabri et al., 2000). In orogenic

systems, gold commonly has a bimodal distribution in which invisible gold within arsenopyrite is overprinted by later visible gold (Coleman, 1957; Mumin et al., 1994; Oberthür et al., 1997; Genkin et al., 1998). The formation of visible gold in Aspy3 is thought to be related to the post-crystallization fracturing and alteration. It is suggested that the submicron lattice bound gold that was probably exsolved from the Aspy2 crystal structure during renewed F2 folding, was then remobilized along secondary fractures and crystal margins characterized by the Aspy3 domain (Morey et al., 2008 and Sayab et al., 2016). The no to low gold grade contents of some idiomorphic arsenopyrite-rich carbonaceous phyllites close to the major quartz vein (e.g. drill hole II-485) is probably related to weak development of Aspy3 due to locally weak post crystallization remobilization and alteration during D2 deformation and overprint.

It is unknown whether an increase in sulfur fugacity (fS2) alone can cause exsolution of possible invisible gold from arsenopyrite. An overall increase in temperature and sulfur fugacity (fS2) due to increase in the amount of S within the hydrothermal phase occurred. The excess S produced by the formation of As-rich alteration rims was responsible for this increase. These relationships are consistent with the observed gold-arsenopyrite textures and the notion that the solubility of gold in arsenopyrite decreases with increasing temperature (Barton, 1969; Kretschmar and Scott, 1976; Sharp et al., 1985). The observed gold-arsenopyrite relationships are best explained by a continuously evolving hydrothermal system, which is expected to preserve gradual changes in mineral chemistry. Furthermore, the higher-temperature event responsible for the Aspy3 rims may have involved only low fluid influx: complete alteration of the Aspy2 grains is more likely during a pervasive high fluid flux event. The lack of major arsenopyrite dissolution suggests that fO2 changes likely played a minimal role during arsenopyrite alteration (Heinrich and Eadington, 1986, Morey et al., 2008). If this secondary hot fluid was significantly undersaturated in gold, it would have possibly removed inferred invisible gold as it replaced the Aspy2. However, since abundant visible gold may have been formed during this stage, this secondary fluid was likely close to saturation and also could have deposited new metal. Fortes (1996) observations in Mina III, that indicate that gold is related to late Aspy3 phases, could therefore be correct, in part.

Proposed formation model

The Ingá orebody formed during successive events of deformation, metamorphism and hydrothermal alteration. The tholeiitic spills overloaded over the komatiitic spills formed a shallow flexural basin with deposition of pelitic-psamitic to chemical sediments when the stratigraphic sequence of the Ingá orebody was deposited, including: dolomites, carbonaceous phyllite and pelites. Over the carbonaceous phyllites and pelites the graywacke was deposited, indicating an increase in sedimentary load (Fig. 12A). The primary features and the petrographic and geochemical properties of the graywackes (Jost et al., 1996) suggest that their clastic load derived from a source area that contained felsic to intermediate igneous and metamorphic rocks that were deposited by turbidity

currents with increasing energy towards the top (Jost et al., 2010). During the deposition of the sediments, forming S0, a distensive event simultaneously occurred, which thickened the graywacke layers and thinned the volcanic strata. This is evidenced by syn-depositional low angle normal faults. This sedimentary basin evolution is correlated to a shallow sea platform environment with proximity to the continental coast (A.J. Massucatto, pers. Commun., 2004). S0 in Ingá is not locally visible, neither in gallery, nor in drill holes, due to the proximity of the orebody to the thrust fault III, where S1 locally transpose S0 at a low angle.
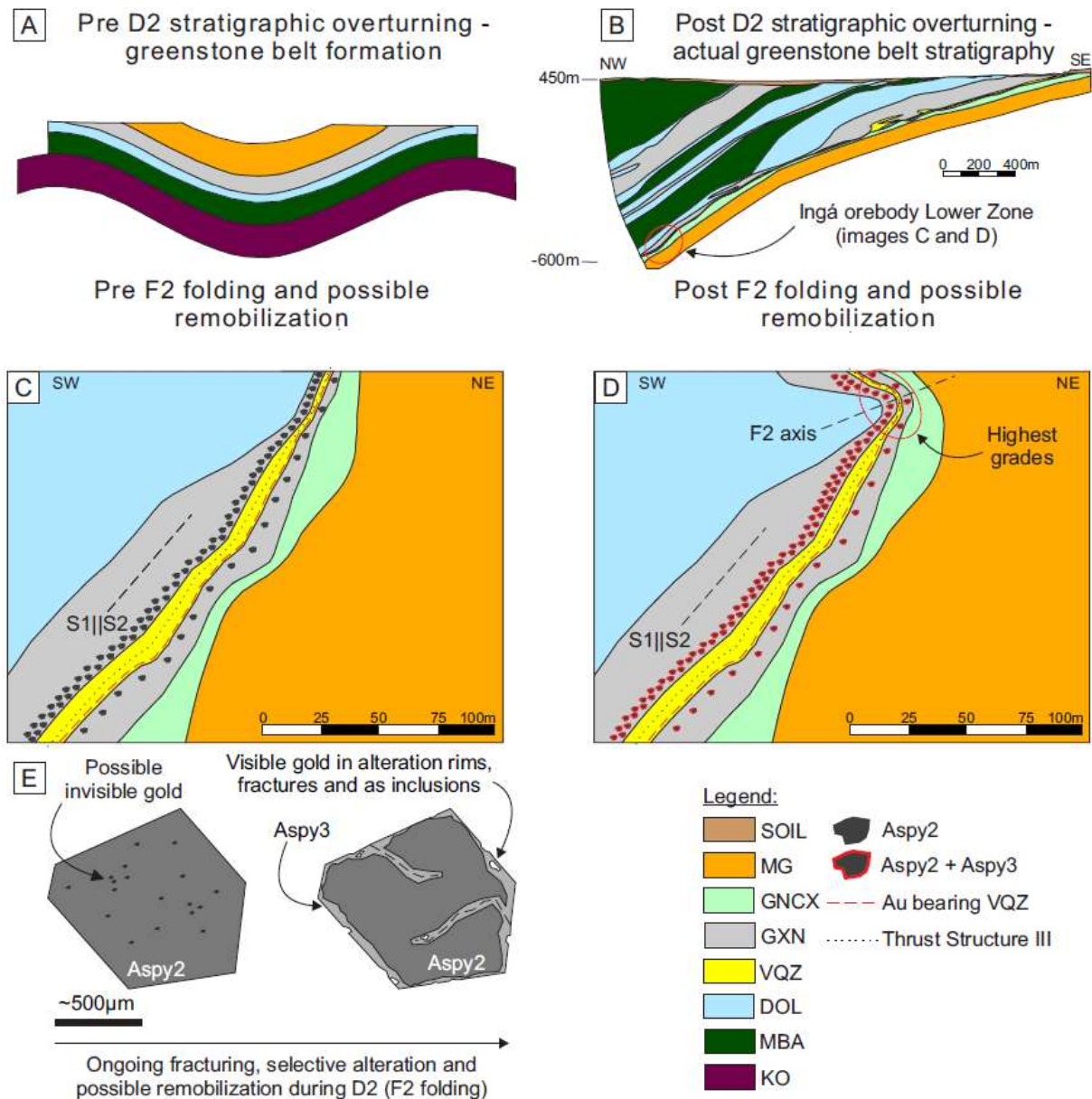
Fig. 12. A) Greenstone belt formation, pre D2 stratigraphic overturning (not to scale). B) Actual greenstone belt stratigraphy, post D2 stratigraphic overturning. C) Studied Ingá cross-section, pre F2 folding and possible remobilization. D) Studied Ingá cross-section, post F2 folding and possible remobilization. E) Ongoing fracturing, selective alteration, and possible remobilization during D2 (F2 folding), affecting arsenopyrite. Abbreviations: Aspy = arsenopyrite, Au = gold, DOL = dolomite, GNCX = quartz-chlorite-sericite-garnet schist, GXN = carbonaceous phyllite, MBA = metabasalt, MG = metagraywacke, KO = komatiite, VQZ = major quartz vein.

The prograde metamorphic path is characterized by the greenschist facies garnet zone, forming the pre-hydrothermal assemblages of the Ingá orebody. During the prograde metamorphic path, isoclinal folding (F1) of bedding and early quartz veins occurred, developing dominant metamorphic schistosity S1 that reoriented crystals. The regional structure of the D1 thrust and thrust ramps suggests that the orebodies lie within an early, regional E-W to NNW-oriented basement-basin fault bend. This zone would have acted as an early zone of maximum extension during basin development with focusing of basin fluids into this area. This pre-dates mineralization, but may have set the architecture for later deep-seated fluid conduits. These block faults would allow enhanced upward migration of fluids into the thrust stack, as well as along thrust structures (T. Coughlin, pers. Commun., 2002). Fortes (1996) suggests the metasediments as the gold source for the hydrothermal fluids. During the retrograde metamorphic path, S1 reactivation and posterior sulphidation-mineralization occurred. Fluids migrated along S0 parallel to S1, facilitated by the low angle thrust fault III and related strain zones that acted as conduits allowing hydrothermal fluids percolation. Sulfide mineralization was then developed pre F2 folding, very likely during the reactivation of S1 schistosity at early stages of exhumation along the retrograde metamorphic path.

Hydrothermal alteration of the peak metamorphic assemblage occurred mainly outwards from the low angle thrust fault III along S0 parallel to S1, forming the silicification, potassic, phyllic and carbonatic haloes within the carbonaceous phyllite and the potassic and phyllic haloes within the GNCX. The newly formed hydrothermal minerals (e.g. biotite and sericite) mimetize the S1 foliation. Possibly gold-poor Aspy1 was formed during the initial stages of hydrothermal alteration and is wrapped by the S1 foliation that was reactivated, also forming strain shadows. Possibly randomly oriented, invisible gold-rich Aspy2 (Fig. 12C) formed during the late stages of D1, accounting for part of the gold budget, occurring in the carbonaceous phyllite close to the low angle thrust fault III and related strain zones, under high fluid-flux conditions. The carbonaceous phyllite and its reduced characteristics acted as a chemical buffer for sulfide precipitation.

During the late stages of D1, building of crack and seal veins (e.g. major quartz vein) parallel to S1 occurred during S1 reactivation, from fluid percolation due to permeability anisotropy within the carbonaceous phyllite. The major quartz vein tends to be emplaced following the floor thrust of the thrust fault III, which sits close to the contact of the carbonaceous phyllite with the GNCX, but may also follow weak zones within the host rock due to hydraulic fracturing, sometimes distant from this contact. Hydraulic fracturing is attested by deformed arsenopyrite-rich carbonaceous phyllite fragments in VQZ interior. Later folding of S1 with NW plunging F2 fold axes and strong NW-SE L2 stretching, also forming boudinage, affected the VQZ. The VQZ core is, in general, massive, but increasingly sheared towards the walls, which indicates that it formed under extension, synchronously with penetrative fabrics in the host rock. These fabrics were later overprinted by continued shear zone movement (Platt, 1983) or from shear zone reactivation, part of subsequent generations of deformation. The competency difference between the major quartz vein and the carbonaceous phyllite,

indicates that the quartz vein concentrates stress, increasing the deformation magnitude in its surroundings, allowing an increase in the carbonaceous phyllite folding, originating strain features in contact with the VQZ.

The common distribution of Au mineralization along the base of D1 quartz veins suggests that part of Au mineralization post-dated the quartz veins, and was commonly deposited by damming of mineralizing fluids during upward migration (L.R. Rankin, pers. Commun., 2004). Aspy2 and Aspy3 inside the carbonaceous phyllite fragments could indicate pre-vein sulfide formation. The gold-rich fluids migrated upwards, mainly through the thrust fault III and related shear zones and precipitated the gold in the present Aspy2 and Aspy3-rich hanging-wall carbonaceous phyllite and in the basal level of the major quartz vein by damming, rarely passing through this basal level to the present footwall host rocks (pre D2 stratigraphic overturning).

The D2 event is responsible for the stratigraphic overturning of the sequence (Fig. 12B), as evidenced by the common facing-down of volcanic and sedimentary primary structures and by the overriding of the metakomatiites onto the metabasalts, which in turn overrides the metasedimentary section (Jost et al., 2010). This D2 stratigraphic overturning formed the present configuration of the Ingá orebody stratigraphy. Later folding of S1 and S1 parallel to mineralization with NW plunging F2 fold axes and strong L2 stretching occurred. NW-SE stretching and boudinage and N-S trending veins also formed. The F2 folding over the major quartz vein and host rocks possibly reconcentrated the gold parallel to F2 axis, locally increasing gold grades. F2 folding locally controls the Ingá ore shoot geometry along with NW-SE stretching, forming the Ingá orebody orientation that varies between 260-315º trend and 20-57º plunge. There is a natural variability in F2 fold axis distribution due to strain heterogeneity or refraction due to F2 folding. During D2, a plane-axial cleavage (S2) was generated by pressure dissolution, causing the transposition of S0 and/or S1 and reorientation of minerals, mainly phyllosilicates.

Possible remobilization of inferred invisible gold in Aspy2 to form visible gold in Aspy3 along late crystal fractures and selective alteration toward the margins occurred because of F2 folding, substantially increasing the orebody gold budget under low fluid-flux conditions (Fig. 12D and 12E). Possible remobilization of inferred invisible gold from Aspy2 to the major quartz vein and host rock gangue occurred as a consequence of F2 folding, as well as the possible new deposition of visible gold during subsequent mineralization events, forming visible gold concentrated in the base of the major quartz vein and disseminated in the carbonaceous phyllite gangue, mainly in the hanging-wall. The weak competency of the quartz vein in relation to F2 folding, causes disruptions in the folded zones, generating E-W accommodation faults. Small brittle-ductile strain zones developed in the planes of these accommodation faults and released the gold from the quartz vein, allowing gold concentration in the gangue of the adjacent carbonaceous phyllite, mainly in the hanging-wall. The F2 folding over the major quartz vein more greatly affected its basal contact in relation to post D2 overturning. This basal

contact is highly folded compared to its upper contact. S2 foliation is also more penetrative in the carbonaceous phyllite in the footwall of the major quartz vein. Gold mineralization therefore pre-dates D2, and is likely D1 or post D1, but has been significantly remobilized and enriched by F2 folding of D1 veins and host rock. D3 N-S compression generates the crenulation cleavage S3, which was identified only in drill holes at Ingá. The S3 crenulation cleavage partially rotates the F2 axis, producing microfolds that reorient mainly phyllosilicates. Apparently D3 did not affect the gold mineralization in the Ingá orebody, there is no evidence for gold related remobilization in the area/samples studied. The D4 event was not recognized at the Ingá orebody.

The lack of structural evidence for deformation events that predate D1 in both the volcanic and sedimentary sections leads to the conclusion that D1 and D2 events occurred during the Paleoproterozoic (Rhyacian) 2170 ± 17 Ma (Jost et al., 2010). Hydrothermal fluids passing through the hanging-wall of the Ingá orebody, along S0 parallel to S1 in the dolomite sequence, leached and carried C, CaO, MgO, and MnO from the dolomites, whose subsequent precipitation pervasively altered the carbonaceous phyllite, originating the carbonatic alteration halo. This is confirmed by the major gains of C, CaO, MgO, and MnO and major losses in almost all other bulk oxides in the carbonatic zone of the carbonaceous phyllite. The diffuse contact between the dolomite sequence and the carbonaceous phyllite also provides strong evidence for this hydrothermal alteration event. This pervasive carbonatic alteration suggests a fluid of relative low temperature and alkaline pH due to the stability of carbonates.

The selective phyllic halo occurs adjacent to the carbonatic zone. The halo originated from fluids with low to moderate temperatures and acidic character, with the potential to leach the host rock (Pirajno, 2009). Alteration substituted feldspars, micas, and mafic minerals to form phengitic muscovite and sericite along S1 foliation, sometimes forming locally massive concentrations. The ferri-biotite which characterizes the pervasive-selective potassic alteration always occurs over the phengitic muscovite in textural relations. Its occurrence is normally related to macroscopically gray-yellow levels abruptly crosscutting the host rock. These level contacts are rarely diffuse. The potassic alteration, that occurs adjacent to the silicification halo, promoted the gain in K_2O in the rock and loss of Fe and Mg from mafic minerals, assisted by fluids that usually have neutral to alkaline pH and elevated temperatures (Pirajno, 2009). Minor to major gains in K_2O in altered GXN and GNCX reflect phyllic (phengitic muscovite and sericite) and potassic (ferri-biotite) alteration over the least altered host rock.

Silicification, in particular, occurred during many events of fluid influx into the carbonaceous phyllite, from pre phyllic alteration to post-potassic alteration. However, a main post-potassic alteration event accounts for the bulk of silicification of the carbonaceous phyllite silicification halo. The least altered GXN and GNCX have a quartz-feldspatic matrix which, along with increase in FeO related to sulfides and CaO related to carbonate-rich venulations, mask the subsequent increase in

SiO2 content along the silicification alteration front. The silicification halo is formed from fluids with high temperatures that promote lixiviation of alkalis from the system (Pirajno, 2009). Due to the difference in pH and temperature conditions in the fluids, and paragenetic variations regarding mineralogy, it is attested that the participation of multiple fluids (at least two) was necessary in the gradative heterogenous hydrothermal system that formed the Ingá orebody. The Ingá orebody is therefore not a typical orogenic gold deposit, suggesting an external influence that is not totally understood. Two main fluids were important in the system, one with an acid pH and low to intermediate temperature and another with neutral to alkaline pH and high temperature. Late high temperature fluids did not totally erase the fabrics created by earlier low to intermediate temperature fluids. The chloritization of biotite and muscovite occurred along the retrograde metamorphic path at lower temperatures. The silicification halo thickness decrease along Ingá orebody plunge, as well as the thickness of the major quartz vein, which reflects less hydrothermal fluid carrying silica down plunge. The phyllic and potassic alteration haloes thicknesses, in contrast, increase. Undated later BCS and QGSS dikes crosscut the stratigraphic sequence.

There is possibly an increase in fluid temperature in the thrust fault III plane. This increase in fluid temperature might be related to friction in the fault plane during hoarsening. The increase in fluid temperature that possibly occurred in the alteration and possible gold remobilization event from inferred invisible gold rich Aspy2 to form visible gold rich Aspy3 is in agreement with the increase in temperature towards the thrust fault III. This increase in temperature is also related to the evolving conditions of the hydrothermal fluids that formed the alteration haloes (e.g. elevated temperatures during potassic and silicification alteration). The formation of Aspy3 also implicated in reduced conditions, increased sulfur fugacity (fS_2) and insignificant oxygen fugacity (fO_2) variations. These conditions acting over Aspy2 possibly promoted a decrease in gold solubility, causing gold remobilization to Aspy3. The diversity of hydrothermal minerals and the extension of the alteration haloes suggest that the hydrothermal alterations were originated from high fluid/rock ratios, followed by a possible D2 remobilization event with low fluid/rock ratios.

Conclusion

The structural, mineralogical, and geochemical data set of this study provide an insight into the geologic history of the Ingá orebody Lower Zone. The orebody is composed, from top to bottom, by massive, brecciated, and laminated dolomite, followed by carbonaceous phyllite (GXN), major crack and seal quartz vein (VQZ), quartz-chlorite-sericite-garnet schist (GNCX), and metagraywacke with rare altered mafic dikes of biotite-chlorite schist (BCS) and quartz-garnet-sericite schist (QGSS) crosscutting the sequence. The Ingá orebody is structurally controlled by the thrust fault III (Structure III) and related shear zones. Compressive events D1, D2, and D3 affected the orebody configuration. During the retrograde metamorphic path, the hydrothermal alteration developed outwards from the Structure III and VQZ, affecting the GXN and GNCX. Hydrothermal alteration is characterized

outwards by silicification, potassic, phyllic, and carbonatic haloes. Different geochemical signatures clearly define these hydrothermal alteration haloes. The mineralization occurs in three different stages, mainly in the silicification zone, including: Pyrrhotite ± Pentlandite ± Arsenopyrite1 (Stage 1), Arsenopyrite2 (Stage II), Arsenopyrite3 ± Pyrrothite ± Chalcopyrite ± Ilmenite ± Rutile ± Magnetite ± Pentlandite ± visible Au (Stage III). Visible gold occurs mainly as free crystals in the basal levels of the VQZ, as free crystals in the GXN matrix, and rarely in rutile and pyrrhotite margins. The VQZ bearing gold vein probably had the bulk of the gold deposited in its basal levels by damming of mineralizing fluids during upward migration. Three types of arsenopyrite are texturally and geochemically identified: Aspy1 (early hydrothermal), Aspy2 (late hydrothermal, possibly invisible gold rich), and Aspy3 (later hydrothermal-remobilization). Visible gold also occurs as inclusions, filling fractures or along the margins of Aspy3. The whole-rock Bi ppm x Se ppm and S percent x Bi ppm plots and major gains in As, Ni, and Co in the Aspy rich carbonaceous phyllite silicification zone may be used to identify potential Aspy3 and gold rich zones in carbonaceous phyllite host rock. These indicators should be used carefully due to the use of whole arsenopyrite crystals in the analysis. SEM and EMP backscattering imaging, SEM-EDS qualitative analysis, EMP, and LA-ICP-MS quantitative analysis to differentiate Aspy2 from Aspy3 rich host rock could be used by the exploration geologist but is discouraged: sample size is limited, analysis costs are high, and times for treatment are long.

Possible remobilization of inferred invisible gold in Aspy2 to form visible gold in Aspy3 along late crystal fractures and selective alteration towards the margins occurred as a consequence of F2 folding. Possible remobilization and possible new deposition of visible gold substantially increased the orebody gold budget. The current microstructural setting of gold therefore masks a complex element mobility history that was linked to hydrothermal alteration and deformation, as suggested by microtextural and geochemical data. We conclude that late high temperature fluids did not totally erased the fabrics deposited by the earlier low to intermediate temperature fluids, and that the hydrothermal system at Ingá was gradative and heterogenous. This indicates that Ingá is not then a typical orogenic gold deposit. By now, a not totally understood external influence acted, encouraging new studies. Four prospective parameters for Ingá type orebodies in the Crixás Gold District were established: (1) major crack and seal quartz vein venulations in thrust fault planes and shear zones; (2) Aspy2 and Aspy3 in carbonaceous phyllite adjacent to major quartz vein and thrust fault; (3) E-W accommodation faults in the F2 folded major quartz vein and; (4) a silicification zone adjacent to the major quartz vein and thrust fault.

Acknowledgments

REFERENCES

Almeida, F.F.M., Neves, B.B.B., Fuck, R.R., 1977, Províncias Estruturais Brasileiras: Anais do Simpósio de Geologia do Nordeste SBG, vol. 8, p. 363-391.

Arehart, G.B., Chryssoulis, S.L., and Kesler, S.E., 1993, Gold and arsenic in iron sulfides from sediment-hosted disseminated gold deposits: Implications for depositional processes: Economic Geology, v. 88, p. 171–185.

Aylmore, M.G., and Graham, J., 1992, Arsenopyrite as a host for refractory gold [ext. abs.]: The Joint Conference on Electron Microscopy and Cell Biology: Electron Microscopy in Mining, Exploration and Metallurgy: Perth, Australia, University of Western Australia, 1992, Extended abstracts, p. 43.

Barbosa, O., Baptista, M.B., Dyer, R.C., Braun, O.P.G., Cotta, J.C., 1969, Geologia e Inventário dos Recursos Minerais da Região Central do Estado de Goiás - Projeto Brasília: Série Geologia DNPM, nº 18, Seção Geologia Básica, Nº 13, Brasília, DF.

Barret, T.J., Fralick, P.W., Jarvis, I., 1987, Rare-earth-element geochemistry of some Archean iron formations north of Lake Superior, Ontario: Canadian Journal of Earth Sciences, vol. 25, p. 570-580.

Barton, P.B. Jr., 1969, Thermochemical study of the system Fe-As-S: Geochimica et Cosmochimica Acta, v. 33, p. 841-857.

Berner, Z.A., Puchelt, H., Noltner, T., and Kramar, U.T.Z., 2013, Pyrite geochemistry in the Toarcian Posidonia Shale of south-west Germany: Evidence for contrasting trace-element patterns of diagenetic and syngenetic pyrites: Sedimentology, v. 60, p. 548-573.

Cabri, L.J., Chryssoulis, S.L., de Villiers, J.P.R., Laflamme, J.H.G., and Buseck, P.R., 1989, The nature of "invisible" gold in arsenopyrite: The Canadian Mineralogist, v. 27, p. 353–362.

Cabri, L.J., Newville, M., Gordon, R.A., Crozier, E.D., Sutton, S.R., McMahon, G. and Jiang, D.T., 2000, Chemical speciation of gold in arsenopyrite: The Canadian Mineralogist, vol. 38, p. 1265–1281.

Carpenter, R.L., 2003, Relative and absolute timing of supracrustal deposition, tectonothermal activity and gold mineralization, West Meliadine region, Rankin Inlet greenstone belt, Nunavut, Canada: Unpublished Ph.D. thesis, London, Ontario, University of Western Ontario, p. 391.

Carvalho, R.S., 2005, Mapeamento Geológico Estrutural da Faixa Leste-Oeste ao Norte do Greenstone Belt de Crixás (GO): Relatório Parcial, Universidade do Estado do Rio de Janeiro, 45 p.

Cathelineau, M., Boiron, M.-C., Holliger, P., Marion, P., and Denis, M., 1989, Gold in arsenopyrites; Crystal chemistry, location and state, physical and chemical conditions of deposition: Economic Geology Monograph, v. 6, p. 328–341.

Ciobanu, C.L., Cook, N.J., Utsunomiya, S., Kogagwa, M., Green, L., Gilbert, S. and Wade, B., 2012, Gold-telluride nanoparticles revealed in arsenic-free pyrite: American Mineralogist, vol. 97, p. 1515–1518.

Coleman, L.C., 1957, Mineralogy of the giant Yellowknife gold mine, Yellowknife, N.W.T.: Economic Geology, v. 52, p. 400-425.

Cook, N.J., Ciobanu, C.L., Mao, J., 2009, Textural control on gold distribution in As-free pyrite from the Dongping, Huangtuliang and Hougou gold deposits, North China Craton (Hebei Province, China): Chemical Geology, v. 264, p. 101–121.

Cook, N.J., Ciobanu, C.L., Meria, D., Silcock, D. andWade, B., 2013, Arsenopyrite-pyrite association in an orogenic gold ore: tracing mineralization history from textures and trace elements: Economic Geology, v. 108, p. 1273–1283.

Cook, N.J. and Chryssoulis, S.L., 1990, Concentrations of invisible gold in the common sulfides: The Canadian Mineralogist, v. 28, p. 1–16.
Deer, W.A., Howie, A., Sussman, J., 1986, An introduction to rock-forming minerals: London, Longman Limited, 528 p.

Deditius, A.P., Utsunomiya, A.S., Reich, M., Kesler, S.E., Ewing, R.C., Hough, R. and Walshe, J., 2011, Trace metal nanoparticles in pyrite: Ore Geology Reviews, v. 42, p. 32-46.

Dubé, B., Mercier-Langevin, P., Hannington, M., Lafrance, B., Gosselin, P., 2007, The LaRonde Penna world-class Au-rich volcanogenic massive sulfide deposit, Abitibi, Québec: Mineralogy and geochemistry of alteration and implications for genesis and exploration: Economic Geology, v. 102, p. 633-666.

Duuring, P., Hassan, L., Zelic, M., Gessner, K., 2016, Geochemical and spectral footprint of metamorphosed and deformed VMS-style mineralization in the Quinns District, Yilgarn Craton, Western Australia: Economic Geology, v. 111, p. 1411-1438.

Fleet, M.E., MacLean, P.J., and Barbier, J., 1989, Oscillatory-zoned Asbearing pyrite from the strata-bound and stratiform gold deposits: An indicator of ore fluid evolution: Economic Geology Monograph, vol. 6, p. 356–362.

Fleet, M.E., and Mumin, A.H., 1997, Gold-bearing arsenian pyrite and marcasite and arsenopyrite from Carlin Trend gold deposits and laboratory synthesis: American Mineralogist, v. 82, p. 182–193.

Fortes, P.T.F.O., 1996, Metalogenia dos depósitos auríferos Mina III, Mina Nova e Mina Inglesa, Greenstone Belt de Crixás, Goiás: Unpublished Ph.D. thesis, Brasília, Brazil, University of Brasilia, p. 177.

Fortes, P.T.F.O., Cheilletz, A., Giuliani, G., Féraud, G., 1997, A Brasiliano age (500±5 Ma) for the Mina III gold deposit, Crixás Greenstone Belt, Central Brazil: International Geology Review, vol. 39, p. 449–460.

Fortes, P.T.F.O., Pimentel, M.M., Santos, R.V., Junges, S.L., 2003, Sm–Nd studies at Mina III gold deposit, Crixás greenstone belt, Central Brazil: implications for the depositional age of the upper metasedimentary rocks and associated Au mineralization: Journal of South American Earth Sciences, vol. 16, p. 503–512.

Fougerouse, D., Micklethwaite, S., Ulrich, S., Miller, J., Godel, B., Adams, D.T., McCuaig, T.C., 2017, Evidence for two stages of mineralization in west Africa's largest gold deposit: Obuasi, Ghana: Economic Geology, v. 112, p. 3–22.

Fuck, R.A., Jardim, E.F., Pimentel, M.M., Dardenne, M.A., Pedrosa-Soares, A.C., 1993, As faixas de dobramentos marginais do Cráton do São Francisco: síntese dos conhecimentos, in: Dominguez, J.M.L., Misi, A., ed., O Cráton do São Francisco, 1st ed.: Salvador, SBG/SGMCNPq, p. 161-185.

Fuck, R.A., 1994, A Faixa Brasília e a compartimentação tectônica da Província Tocantins [ext. abs.]: Simposio de Geologia do Centro-Oeste SBG, 4th, Brasilia, Brazil, 1994, Extended abstracts, p. 184-187.

Genkin, A.D., Bortnikov, N.S., Cabri, L.J., Wagner, F.E., Stanley, C.J., Safonov, Y.G., McMahon, G., Friedl, J., Kerzin, A.L., and Gamyanin, G.M., 1998, A multidisciplinany study of invisible gold in arsenopyrite from four mesothermal gold depositis in Siberia, Russian Federation: Economic Geology, v. 93, p. 463–487.

Gourcerol, B., Kontak, D.J., Thurston, P.C., Petrus, J.A., 2018. Application of LA-ICP-MS sulfide analysis and methodology for deciphering elemental paragenesis and associations in addition to multi-stage processes in metamorphic gold settings: Economic Geology, v. 56, p. 39-64.

Grant, J., 1986, The isocon diagram – A simple solution to Gresens`equation for metasomatic alteration: Economic Geology, v. 81, p. 1976-1982.

Gregory, D.D., Large, R.R., Halpin, J.A., Baturina, E.L., Lyons, T.W., Wu, S., Danyushevsky, L., Sack, P.J., Chappaz, A., Maslennikov, V.V., Bull, S.W., 2015, Trace element content of sedimentary pyrite in black shales: Economic Geology, v. 110, p. 1389-1410.

Gregory, D.D., Large, R.R., Bath, A.B., Steadman, J.A., Wu, S., Danyushevsky, L., Bull, S.W., Holden, P., and Ireland, T.R., 2016, Trace element content of pyrite from the Kapai Slate, St. Ives gold district, Western Australia: Economic Geology, v. 111, p. 1297–1320.

Haskin, L.A., Frey, F., A, Schmitt, R.A., Smith, R.H., 1968, Meteoric, solar and terrestrial rare-earth distributions: Physical Chemical Earth, vol. 7, p. 167–321.
Haskin, M.A., and Haskin, L.A., 1966, Rare earths in European shales: A redetermination: Science, v. 154, p. 507-509.

Hazarika, P., Mishra, B., Chinnasamy, S.S. and Bernhardt, H.J., 2013, Multi-stage growth and invisible gold distribution in pyrite from the Kundarkocha sedimenthosted gold deposit, eastern India: Ore Geology Reviews, vol. 55, p. 134–145.

Heinrich, C.A., and Eadington, P.J., 1986, Thermodynamic predictions of the hydrothermal chemistry of arsenic, and their significance for the paragenetic sequence of some cassiterite-arsenopyrite-base metal sulfide deposits: Economic Geology, v. 81, p. 511–529.

Hey, M.H., 1954, A new review of the chlorites: Mineral Magazine, vol. 80, p. 277-292.

Huston, D.I., Sie, S.H., Suter, G.F., Cooke, D.R., Both, R.A., 1995, Trace elements in sulfide minerals from eastern Australia volcanichosted massive sulphide deposit: Economic Geology, v. 90, p. 1167-1196.

Johan, Z., Marcoux, E. and Bonnemaison, M., 1989, Arsénopyriteaurifère: mode de substitution de Au dans le structure de FeAsS: Comptes Rendus de l'Académie des Sciences, v. 308, p. 185–191.

Jost, H., Theodoro, S.M.C.H., Figueiredo, A.M.G., Boa Ventura, G.R., 1996, Propriedades geoquímicas e proveniência de rochas metassedimentares detríticas arqueanas dos greenstone belts de Crixás e Guarinos, Goiás: Revista Brasileira de Geociências, vol. 26, p. 151–166.

Jost, H., Chemale Jr., F., Dussin, I.A., Tassinari, C.C.G., Martins, R., 2010, A U-Pb zircon Paleoproterozoic age for the metasedimentary host rocks and gold mineralization of the Crixas greenstone belt, Goias, Central Brazil: Ore Geology Reviews, vol. 37, p. 127-139.

Jost, H., and Fortes, P.T.F.O., 2001, Gold deposits and occurrences of the Crixás Goldfields, central Brazil: Mineralium Deposita, v. 36, p. 358-376.

Jost, H. & Oliveira, A.M. 1991. Stratigraphy of the greenstone belts, Crixás region, Goiás, Central Brazil: Journal of South American Earth Sciences, v. 4, p. 201-214.

Kamber, B.S., Greig, A., Collerson, K.D., 2005, A new estimate for the composition of weathered young upper continental crust from alluvial sediments, Queensland, Australia: Geochimica et Cosmochimica Acta, vol. 69, p. 1041-1058.

Kretschmar, U. and Scott, S.D., 1976, Phase relations involving arsenopyrite in the system Fe-As-S and their application: The Canadian Mineralogist, vol. 14, p. 364–386.

Large, R.R., Maslennikov, V.V., Robert, F., Danyushevsky, L.V. and Chang, Z. (2007) Multistage sedimentary and metamorphic origin of pyrite and gold in the giant Sukhoi Log deposit, Lena gold province, Russia: Economic Geology, vol. 102, p. 1233–1267.

Large, R.R., Danyushevsky, L., Hollit, C., Maslennikov, V., Meffre, S., Gilbert, S. and Foster, J., 2009, Gold and trace element zonation in pyrite using a laser imaging technique: implications for the timing of gold in orogenic and Carlin-style sediment-hosted deposits: Economic Geology, v. 104, p. 635–668.

Large, R.R., Bull, S., and Maslennikov, V.V., 2011, A carbonaceous sedimentary source-rock model for Carlin-type and orogenic gold deposits: Economic Geology, v. 106, p. 331–358.

Larocque, A.C.L., Hodgson, C.J., Cabri, L.J., and Jackman, J.A., 1995, Ion microprobe analysis of pyrite, chalcopyrite and pyrrhotite from the Mobrun VMS deposit in northwestern Quebec: Evidence for metamorphic remobilization of gold: Canadian Mineralogist, v. 33, p. 373–388.

Lawley, C.J.M., Creaser, R.A., Jackson, S.E., Yang, Z., Davis, B.J., Pehrsson, S.J., Dubé, B., Mercier-Langevin, P., Vaillancourt, D., 2015, Unraveling the western Churchill Province paleoproterozoic gold metallotect: Constraints from Re-Os arsenopyrite and U-Pb xenotime geochronology and LA-ICP-MS arsenopyrite trace element chemistry at the BIF-hosted Meliadine Gold District, Nunavut, Canada: Economic Geology, v. 110, p. 1425-1454.

Lebrun, E., Thébaud, N., Miller, J., Roberts, M., Evans, N., 2017, Mineralization footprints and regional timing of the world-class Siguiri orogenic gold district (Guinea, West Africa): Mineralium Deposita, v. 52, p. 539-564.

Magalhães, L.F., 1991, Cinturão de Cisalhamento de Empurrão Córrego Geral-Meia Pataca: Geologia, Deformação, Alteração Hidrotermal e Mineralizações Auríferas Associadas Crixás-Goiás: Unpublished M.Sc. thesis, Brasília, Brazil, University of Brasilia, p. 233.

Morey, A.A., Weinberg, R.F., and Bierlein, F.P., 2007, The structural controls of gold endowment within the Bardoc Tectonic Zone, Eastern Goldfields Province, Western Australia: implications for gold endowment in shear systems: Mineralium Deposita, v. 42, p. 583–600.

Morey, A.A., Tomkins, A.G., Bierlein, F.P., Weinberg, R.F., and Davidson, G.J., 2008, Bimodal distribution of gold in pyrite and arsenopyrite: Example from the Archean Boorara and Bardoc shear systems, Yilgarn craton, western Australia: Economic Geology and the Bulletin of the Society of Economic Geologists, v. 103, p. 599–614.

Mumin, A.H., Fleet, M.E., and Chryssoulis, S.L., 1994, Gold mineralization in As-rich mesothermal gold ores of the Bogosu-Prestea mining district of the Ashanti gold belt, Ghana: Remobilization of "invisible" gold: Mineralium Deposita, v. 29, p. 445–460.

Oberthür, T., Weiser, T., Amanor, J.A., and Chryssoulis, S.L., 1997, Mineralogical siting and distribution of gold in quartz veins and sulfide ores of the Ashanti mine and other deposits in the Ashanti belt of Ghana: genetic implications: Mineralium Deposita, v. 32, p. 2–15.

Palenik, C.S., Utsunomiya, S., Reich, M., Kesler, S.E., Wang, L., and Ewing, R.C., 2004, "Invisible" gold revealed: Direct imaging of gold nanoparticles in a Carlin-type deposit: American Mineralogist, v. 89, p. 1359–1366.

Passchier, C.W., and Trouw, R.A., 2005, Microtectonics: Berlin, Springer, 382p.

Pimentel, M.M., Fuck, R.A., Jost, H., Ferreira Filho, C.F., Araújo, S.M., 2000, The basement of the Brasilia Fold Belt and the Goias Magmatic Arc, in Cordani, U.G., Milani, E.J., Thomaz Filho, A., Campos, D.A., ed., Tectonic evolution of South America, 1st ed.: Rio de Janeiro, 31st International Geological Congress Special Publication, p. 195-229.

Piper, D.Z., 1974, Rare earth elements in the sedimentary cycle: a summary: Chemical Geology, v. 14, p. 285-304.

Pirajno, F., 2009, Hydrothermal Processes and Mineral Systems, Springer Netherlands, 1250p.

Platt, J.P., 1983, Progressive refolding in ductile shear zones: Journal of Structural Geology, v. 6, p. 619-622.

Pokrovski, G.S., Kara, S., and Roux, J., 2002, Stability and solubility of arsenopyrite, FeAsS, in crustal fluids: Geochimica et Cosmochimica Acta, v. 66, p. 2361–2378.

Portocarrero, J.L.T., 1996, Geologia da jazida aurífera Mina Nova, greenstone belt de Crixás, Goiás. Brasília: Unpublished M.Sc. thesis, Brasilia, Brazil, University of Brasilia, p. 102.

Resende, M.G., Jost, H., Osborne, G.A., Mol, A.G., 1998, Stratigraphy of the Goiás and Faina greenstone belts, central Brazil: a new proposal: Revista Brasileira de Geociências, vol. 28, p. 77-94.

Robert. F., Poulsen, H., 2001, Vein formation and deformation in Greenstone gold deposits: Society of Economic Geologists Reviews, v. 14, p. 111-155.

Rottier, B., Kouzmanov, K., Wälle, M., Bendezú, R., and Fontboté, L., 2016, Sulfide replacement processes revealed by textural and LA-ICP-MS trace element analyses: Example from the early mineralization stages at Cerro de Pasco, Peru: Economic Geology, v. 111, p. 1347-1367.

Spearman, C., 1904, The proof and measurement of association between two things: American Journal of Psychology, v. 15, p. 72-101.

Queiroz, C.L., 1995, Caracterização dos domínios estruturais e da arquitetura do Greenstone Belt de Crixás, Goiás: Unpublished M.Sc. thesis, Brasilia, Brazil, University of Brasília, p. 118.

Sabóia, L.A., 1979, Os greenstone belts de Crixás e Goiás, GO: Boletim Informativo da Sociedade Brasileira de Geologia Núcleo Centro-Oeste, vol. 9, p. 44-72.

Sabóia, L.A., Teixeira, N.A., Castro, J.H.G., Texeira, A.S., 1981, Geologia do greenstone belt de Crixás (GO) e suas implicações geotectônicas [ext. abs.]: Simpósio sobre o Cráton de São Francisco e suas Faixas Marginais, 1st, Salvador, Brazil, 1981, Extended Abstracts, p. 39-50.

Sabóia, L.A. & Teixeira, N.A., 1980, Lavas ultrabásicas da unidade basal do greenstone belt de Crixás (GO): Uma nova classe de rochas ultrabásicas no Estado de Goiás: Revista Brasileira de Geociências, vol. 10, p. 28-42.

Sayab, M., Suuronen, J.P., Molnar, F., Villanova, J., Kallonen, A., O`Brien, H., Lahtinen, R., Lehtonen, M., 2016, Three-dimensional textural and quantitative analyses of orogenic gold at the nanoscale: Geology, v. 44, p. 739-742.

Sharp, Z. D., Essene, E.J., and Kelly, W.C., 1985, A re-examination of the arsenopyrite geothermometer: Pressure considerations and applications to natural assemblages: Canadian Mineralogist, v. 23, p. 517–534.

Simon, G., Huang, H., Penner-Hahn, J.E., Kesler, S.E., and Kao, L., 1999a, Oxidation state of gold and arsenic in gold-bearing arsenian pyrite: American Mineralogist, v. 84, p. 1071–1079.

Simon, G., Kesler, S.E. and Chryssoulis, S., 1999b, Geochemistry and textures of gold-bearing arsenian pyrite, Twin Creeks, Nevada; implications for deposition of gold in Carlin-type deposits. Economic Geology, vol. 94, p. 405–421.

Speer, J.A., 1981, Micas in igneous rocks: Canadian Mineralogist, vol. 19, p. 35-46.

Steadman, J.A., and Large, R.R., 2016, Synsedimentary, diagenetic, and metamorphic pyrite, pyrrhotite, and marcasite at the Homestake BIF-hosted gold deposit, South Dakota, USA: Insights on Au-As ore genesis from textural and LA-ICP-MS trace element studies: Economic Geology, v. 111, p. 1731-1752.

Sung, Y.H., Brugger, J., Ciobanu, C.L., Pring, A., Skinner, W., and Nugus, M., 2009, Invisible gold in arsenian pyrite and arsenopyrite from a multistage Archaean gold deposit: Sunrise Dam, Eastern Goldfields Province, Western Australia: Mineralium Deposita, v. 44, p. 765–791.

Tarnocai, C.A., Hattori, K. and Cabri, L.J., 1997, 'Invisible' gold in sulfides from the Campbell mine, Red Lake greenstone belt, Ontario: evidence for mineralization during the peak of metamorphism. The Canadian Mineralogist, vol. 35, p. 805–815.

Taylor S. R. and McLennan S. M., 1985, The Continental Crust: Its Composition and Evolution: Oxford UK, Blackwell, p. xxx.

Theodoro, S.M.C.H., 1995, Ambiente de sedimentação da Formação Ribeirão das Antas, Grupo Crixás – Goiás: Unpublished M.Sc. thesis, Brasília, Brazil, University of Brasilia, p. 88.

Tomkins, A.G., and Mavrogenes, J.A., 2001, Redistribution of gold within arsenopyrite and löllingite during pro- and retrograde metamorphism: Application to timing of mineralization: Economic Geology, v. 96, p. 525–534.

Tomkins, A.G., and Mavrogenes, J.A., 2002, Mobilization of gold as a polymetallic melt during pelite anatexis at the Challenger deposit, South Australia: A metamorphosed Archean gold deposit: Economic Geology, v. 97, p. 1249–1271.

Yamaoka, W.N., Araújo, E.M., 1988, Depósitos de Ouro da Mina III. Crixás Goiás, in Schobbenhaus, C., Queiroz, E.T., Coelho, C.E.S., ed., Principais Depósitos Minerais do Brasil vol. 3, 1st ed.: Brasilia, Brazilian Ministry of Mines and Energy, Departamento Nacional da Produção Mineral, p. 491–498.

Wilkinson, J.J., Chang, Z., Cooke, D.R., Baker, M.J., Wilkinson, C.C., Inglis, S., Chen, H., Gemmell, J.B., 2015, The chlorite proximitor: A new tool for detecting porphyry ore deposits: Journal of Geochemical Exploration, v. 152, p. 10-26.

Wu, X. and Delbove, F., 1989, Hydrothermal synthesis of gold-bearing arsenopyrite: Economic Geology, vol. 84, p. 2029–2032.

3.   REFERÊNCIAS BIBLIOGRÁFICAS

Almeida, B.S. 2006. Mineralização aurífera, alteração hidrotermal e indicadores prospectivos do Corpo Palmeiras, greenstone belt de Crixás, Goiás. Trabalho de Conclusão de Curso de Geologia, Instituto de Geociências, Universidade Federal do Rio Grande do Sul, 88 p.

Almeida, F.F.M., Neves, B.B.B. & Fuck, R.R. 1977. Províncias Estruturais Brasileiras. In: Simpósio de Geologia do Nordeste, 8., 1977, Anais, SBG, p. 363-391.

Arndt, N.T., Teixeira, N.A., White, W.M. (1989). Bizarre geochemistry of komatiites from the Crixás greenstone belts, Brazil. Contributions to Mineral Petrology. 101: 187-197.

Barbosa, O., Baptista, M.B., Dyer, R.C., Braun, O.P.G., Cotta, J.C. 1969. Geologia e Inventário dos Recursos Minerais da Região Central do Estado de Goiás - Projeto Brasília. DNPM, Série Geologia, nº 18, Seção Geologia Básica, Nº 13, Brasília, DF, 1989.

Bierlein, F.P., Crowe, D.E. 2000. Phanerozoic orogenic lode gold deposits. Reviews in Economic Geology, 13: 103-139.

Carvalho, R.S. 2005. Mapeamento Geológico Estrutural da Faixa Leste-Oeste ao Norte do Greenstone Belt de Crixás (GO). Rio de Janeiro, Universidade do Estado do Rio de Janeiro, 45 p., Relatório Parcial.

Castoldi, M.A.S.C. 2015. O distrito aurífero de Crixás – GO: Caracterização do novo corpo de minério Ingá. Trabalho de Conclusão de Curso de Geologia, Instituto de Geociências, Universidade Federal do Rio Grande do Sul, 182 p.

Colvine, A.C., Fyon, J.A., Heather, K.B., Marmont, S., Simth, P.M., Troop, D.G. 1988. Archean lode gold deposits in Ontario. Ontario Geological Survey, Misc Pap 139.

Colvine, A.C., 1989. An empirical model for the formation of Archean gold deposits. Products of final cratonization of the Superior Province, Canada. In: Keays, R.R., Ramsay, W.R.H., Groves, D.I. (Ed.) The Geology of Gold Deposits: The Perspective in 1988. Economic Geology Monograph, 6: 37–53.

Danni, J.C.M. & Ribeiro, C.C. 1978. Caracterização Estratigráfica da Sequência Vulcano-Sedimentar de Pilar de Goiás e de Guarinos, Goiás. In: Congresso Brasileiro de Geologia, Anais, SBG, 34: 582-596.

Dantas, E.L., Jost, H., Fuck, R.A., Brod, J.A., Pimentel, M.M. 2001. Proveniência e idade deposicional de sequências metavulcano-sedimentares da região de Santa Terezinha de Góias, baseada em dados isotópicos Sm-Nd e de U-Pb em monocristal de zircão. Revista Brasileira de Geociências., 31: 329-334.

Fortes, P.T.F.O., Cheilletz, A., Giulian, G., Féraud, G. 1997. A Brasiliano Age (500±5 Ma) for the Mina III Gold Deposit, Crixás Greenstone Belt, Central Brazil. International Geology Review, 39: 449-460.

Fortes, P.T.F.O., Pimentel, M.M., Santos, R.V., Junges, S.L. 2003. Sm–Nd studies at Mina III gold deposit, Crixás greenstone belt, Central Brazil: implications for the depositional age of the upper metasedimentary rocks and associated Au mineralization. Journal of South American Earth Sciences, 16: 503–512.

Foster, R.P., Mann, A.G., Stowe, C.W., Wilson, J.E. 1986. Archean gold mineralization in Zimbabwe. In: Anhaeusser C.R., MASKE S. (eds) Mineral deposits of Southern Africa. Johannesburg. Geological Society of Africa 1, p. 43-112.

Fuck, R.A., Jardim, E.F., Pimentel, M.M., Dardenne, M.A., Pedrosa-Soares, A.C. 1993. As faixas de dobramentos marginais do Cráton do São Francisco: síntese dos

conhecimentos. In: J.M.L. Dominguez, A. Misi (Eds.) O Cráton do São Francisco, Salvador. SBG/SGMCNPq, p. 161-185.

Fuck, R.A. 1994. A Faixa Brasília e a compartimentação tectônica da Província Tocantins. In: SBG, Simp. de Geologia do Centro-Oeste, IV, Anais, p. 184-187.

Groves, D.I., Phillips, G.N., Ho, S.E., Houston, S.M., Standing, C.A. 1987. Craton-scale distribution of Archean greenstone gold deposits: predictive capacity of the metamorphic model. Economic Geology, 81: 2045-2058.

Groves, D.I. & Foster, R.P. 1991. Archean Lode gold deposits. In: Foster R.P. (ed) Gold metallogeny and exploration. Chapman and Hall, London, 63-103 p.

Groves, D.I., Goldfarb, R.J., Gebre-Mariam, M., Hagemann, S.G., Robert, F. 1998. Orogenic gold deposits: A proposed classification in the context of their crustal distribution and relationship to other gold deposit types. Ore Geology Reviews, 13: 7–27.

Groves, D.I., Goldfarb, R.J., Robert, F., Hart, C.J.R. 2003. Gold deposits in metamorphic belts: Overview of current understanding, outstanding problems, furute research and exploration significance. Economic Geology, 98: 1-29.

Hagemann, S.G., Cassidy, K.F. 2000. Archean orogenic lode gold deposits. Reviews in Economic Geology, 13: 9-68.

Jost, H. & Oliveira, A.M. 1991. Stratigraphy of the greenstone belts, Crixás region, Goiás, Central Brazil. Journal of South American Earth Sciences, v. 4: 201-214.

Jost, H., Carmelo, A.C. & Menezes, P.R. 1994a. Litologias, relações de contato e estrutura do Bloco Caiamar, Crixás, Goiás. In: Simpósio de Geologia do Centro-Oeste, v. 4, 1994, Brasília, SBG, Resumo expandido, p. 18-20.

Jost, H., Theodoro, S.M.C.H., Figueiredo, A.M.G., Boaventura, G.R. 1994b. Propriedades geoquímicas e proveniência de rochas metassedimentares detríticas arqueanas dos greenstone-belts de Crixás e Guarinos, Goiás. Revista Brasileira de Geociências, 26: 151-166.

Jost, H. 2001. Síntese dos terrenos arqueanos de Goiás. Relatório interno – AngloGold Ashanti. 38p.

Jost, H. & Fortes, P.T.F.O. 2001. Gold deposits and occurrences of the Crixás Goldfields, central Brazil. Mineralium Deposita 2001.

Jost, H., Chemale Jr., F., Dussin, I.A., Tassinari, C.C.G., Martins, R. 2010. A U-Pb zircon Paleoproterozoic age for the metasedimentary host rocks and gold mineralization of the Crixás greenstone belt, Goiás, Central Brazil. Ore Geology Reviews 37 (2010): 127-139.

Massucato, A.J. 2004. Relatório de Geologia Estrutural - Aspectos Estruturais do Greenstone Belt de Crixás - GO - Anglogold Ashanti, Crixás-GO, 30p. Relatório Interno.

Matsui, J. 2002. Seção logitudinal da MINA III. AngloGold Ashanti – Serra Grande.

Oliveira, C.C. 1983. Programa Levantamentos Geológicos Básicos do Brasil. Folha 22-Z-C-VI/ Itaguaru-GO. Goiânia. CPRM/DNPM.

Phillips, G.N. & Groves, D.I. 1983. The nature of Archean gold-bearing fluids as deduced from gold deposits of Western Australia. J Geol Soc Aust 30: 35-39.

Pimentel, M.M., Fuck, R.A., Jost, H., Ferreira Filho, C.F., Araújo, S.M. 2000. The basement of the Brasilia Fold Belt and the Goias Magmatic Arc. In: Cordani UG, Milani EJ, Thomaz Filho A, Campos DA (eds) Tectonic evolution of South America. 31st International Geological Congress Special Publication, Rio de Janeiro, pp 195-229.

Portocarrero, J.L.T. 1996. Geologia da jazida aurífera Mina Nova, greenstone belt de Crixás, Goiás. Brasília, 102 p. Dissertação de Mestrado, Instituto de Geociências, UNB.

Queiroz, C.L. 2000. Evolução tectono-estrutural dos terrenos granito-greenstone belt de Crixás, Brasil Central. Dissertação de Doutorado, Instituto de Geociências, Universidade de Brasília, 209 p.

Resende, M.G., Jost, H., Osborne, G.A., Mol, A.G. 1998. Stratigraphy of the Goiás and Faina greenstone belts, central Brazil: a new proposal. Revista Brasileira de Geociências, 28(1): 77-94.

Resende, M.G. 1999. Estudo da evolução das supracrustais metassedimentares dos greenstone belts de Goiás e Faina, GO. Brasília, 259 p. Tese de Doutorado em Geociências, Universidade de Brasília.

Robert, F., Poulsen, K.H., Dubé, B. 1997. Gold deposits and their geological classification. Exploration Geochemistry. In: Proceedings of Exploration 97: Fourth Decennial International Conference on Mineral Exploration", pp. 12.

Sabóia, L.A. & Teixeira, N.A. 1980. Lavas ultrabásicas da unidade basal do greenstone belt de Crixás (GO): Uma nova classe de rochas ultrabásicas no Estado de Goiás. Revista Brasileira de Geociências, 10(1): 28-42.

Sabóia, L.A., Teixeira, N.A., Castro, J.H.G., Texeira, A.S. 1981. Geologia do greenstone belt de Crixás (GO) e suas implicações geotectônicas. In: SBG. Simpósio sobre o Cráton de São Francisco e suas Faixas Marginais, Salvador, Anais, p. 39-50.

Silva, H.V. 2014. Descrição litológica e hidrotermal de testemunhos de sondagem do "Corpo Ingá - Estrutura III" do greenstone belt de Crixás, Goiás. Relatório do Estágio Supervisionado em Geologia, Centro de Ciências Agrárias, Universidade Federal do Espírito Santo, 55 p.

Sobiesiak, M.S. 2011. Caracterização de depósito aurífero no Corpo Pequizão, Crixás-GO. Trabalho de Conclusão de Curso de Geologia, Instituto de Geociências, Universidade Federal do Rio Grande do Sul, 100 p.

Theodoro, S.M.C.H. 1995. Ambiente de sedimentação da Formação Ribeirão das Antas, Grupo Crixás - Goiás. Brasília, 88 p. Dissertação de Mestrado. Instituto de Geociências, Universidade Federal de Brasília.

Vargas, M.C. 1992. Geologia dos Granito-Gnaisses dos Terrenos Granito-Greenstone da Região de Crixás, Guarinos, Pilar de Goiás e Hidrolina, Goiás. Brasília, 172 p. Dissertação de Mestrado. Instituto de Geociências, Universidade de Brasília.

Yamaoka, W.N., & Araújo, E.M. 1988. Depósitos de Ouro Mina III, Crixás, Goiás. In: C. Schobbenhaus & C.E.S. Coelho (Eds.) Principais Depósitos Minerais do Brasil, Brasília, NPM/CVRD, v. 3, cap. 34: 491-498.

4.   HISTÓRICO ESCOLAR

MARCO ANTONIO SARTORI CASTOLDI

193394

Lista das atividade de ensino do aluno avaliadas pelo curso.

HISTÓRICO CURSO
GEOCIÊNCIAS – Mestrado Acadêmico - 01/03/2016

Período Letivo	Código	Disciplina	Créditos	Conceito	Situação
2017/02	GEB00129	Petrologia orgânica e geoquímica de carvão e rochas geradoras de petróle	6	A	Aprovado
2017/01	GEB00065	Geoquímica isotópica aplicada a depósitos minerais	5	A	Aprovado
2016/02	GEB00057	Depósitos minerais em ambientes hidrotermais	5	A	Aprovado
2016/02	GEB00104	Petrologia e metalogenia de rochas máficas-ultramáficas	4	A	Aprovado
2016/01	GEP92-58	T. E. em Geoquímica: CURRENT TOPICS IN ROCK METAMORPHISM	2	B	Aprovado
2015/01	MMD00073	INTRODUÇÃO A GEOESTATÍSTICA	3	B	Validação
		Inglês em 06/08/2017	-	-	-

Totais

Créditos Cursados com Aprovação neste Curso: 22
Créditos por Validação: 3
Total: 25

5.   PARECERES DA BANCA EXAMINADORA

ATA Nº 841

A comissão abaixo assinada tendo examinado a Dissertação de Mestrado do aluno **Marco Antônio Sartori Castoldi**, intitulada *"GEOLOGIA E GEOQUÍMICA DA ZONA INFERIOR DO CORPO DE MINÉRIO INGÁ, DISTRITO AURÍFERO DE CRIXÁS, GOIÁS, BRASIL: IMPLICAÇÕES GENÉTICAS E EXPLORATÓRIAS"*, atribuem os seguintes conceitos:

Prof. Dr. Diego Machado Marques (PPGGEO/UFRGS)
CONCEITO: "A" (EXCELENTE)

Prof. Dr. Artur Cezar Bastos Neto (PPGGEO/UFRGS)
CONCEITO: "A" (EXCELENTE)

Prof. Dr. Arthur Lemos Giovannini (Degeo/UFRGS)
CONCEITO: "A" (EXCELENTE)

de   de 2018.

Homologação pela Comissão de Pós-Graduação,	
Ata nº	Data:
Conceito Final:	
Rubrica:	

ANEXO I

Título da Dissertação/Tese:

"GEOLOGIA E GEOQUÍMICA DA ZONA INFERIOR DO CORPO DE MINÉRIO INGÁ, DISTRITO AURÍFERO DE CRIXÁS, GOIÁS, BRASIL: IMPLICAÇÕES GENÉTICAS E EXPLORATÓRIAS"

Área de Concentração: Geoquímica

Autor: **Marco Antônio Sartori Castoldi**

Orientador: Prof. Dr. José Carlos Frantz

Examinador: Prof. Dr. Artur Cezar Bastos Neto

Data: 11 de janeiro de 2013

Conceito: A EXCELENTE

PARECER:

A dissertação está estruturada de acordo com o padrão do PPGEO. No Capítulo 1, os objetivos são apresentados de forma muito clara. No Estado da Arte e Contextualização Teórica o autor demonstra que adquiriu um grande poder de síntese, mas permanece com dificuldades para entender quando termos como arquesano são utilizados como substantivo ou como adjetivo referente a maciços ou minerais respectivamente. O autor também ainda não entendeu que fluído (com acento) não é substantivo, sendo o particípio do verbo fluir.

O artigo foi submetido a periódico internacional específico da área do estudo e de ótimo nível. Todas as informações necessárias para os entendimentos do problema inseridos no contexto geológico são fornecidas. A amostragem é descrita e adequadamente, assim como os métodos analíticos empregados.

A apresentação dos resultados inicia com as descrições petrográficas da rocha encaixante e na alteração hidrotermal e da mineralização. Ambas são muito bem ilustradas por uma coleção de fotografias de testemunhos e minerais, além de boas fotomicrografias muito esclarecedoras. Os dados estruturais são apresentados corretamente. O ponto fraco do trabalho está na mineralogia, mais especificamente nos lados de mineração de tríaca. O grande número de dados disponíveis é subutilizado e mal apresentado na Tabela 4 que tem numerosos problemas de organização/ordem, além da ausência de informações sobre como foram efetuados os cálculos de fórmula estrutural, distribuição dos elementos nos diferentes sítios dos diferentes minerais.

O termo semi-estável não é recomendável e tratando-se de dados e MSE, não tem nenhum significado. A mistura de dados petrográficos com dados obtidos por MSE, como ocorre nas páginas 41 e 43, não serão aceitas pelos revisores do artigo. A Figura 7 tem dois diagramas estranhos. O diagrama E apresenta valor negativo de ΔFI. Pelo diagrama G, um Pilosilicato com k=0,5 (0,25, calculado para 0=11) seria uma muscovita fengítica; possivelmente, os campos não foram corretamente identificados.

O ponto forte do trabalho está na discussão. O autor demonstra grande conhecimento geológico, embora, às vezes, a discussão e as interpretações extrapolem os dados disponíveis, como é o caso da parte estrutural.

Os pequenos problemas não diminuem a qualidade do trabalho que representa uma ótima contribuição que implica em grandes avanços no conhecimento da evolução geológica e mineralógica da zona inferior do corpo mineralizado do Ipueira. Este era o objetivo principal do trabalho, foi plenamente atingido, justificando com sobras o conceito A Excelente.

Assinatura: Artur Bastos   Data: 11/01/2013

Ciente do Orientador:

Ciente do Aluno:

ANEXO I

Título da Dissertação/Tese:

"GEOLOGIA E GEOQUÍMICA DA ZONA INFERIOR DO CORPO DE MINÉRIO INGÁ, DISTRITO AURÍFERO DE CRIXÁS, GOIÁS, BRASIL: IMPLICAÇÕES GENÉTICAS E EXPLORATÓRIAS"

Área de Concentração: Geoquímica

Autor: **Marco Antônio Sartori Castoldi**

Orientador: Prof. Dr. José Carlos Frantz

Examinador: Prof. Dr. Arthur Lemos Giovannini

Data:
11 de janeiro de 2019

Conceito:
A - Excelente

PARECER:

A dissertação esta bem estruturada conforme o padrão do PPGGEO, com um artigo submetido a uma revista internacional nível A1 com um corpo editorial e de revisores qualificados.

Os objetivos do trabalho são bem apresentados, bem como os métodos utilizados para atingi-los. O estado da arte apresenta uma ótima revisão sobre a geologia e a mineralização na região.

Os resultados obtidos são bem apresentados, as descrições petrográficas são muito boas e corroboradas com ótimas imagens, apresentando as assembleias minerais das alterações hidrotermais, resumidas nas tabelas 3a e 3b. Os dados estruturais obtidos também são bem apresentados.

O trabalho apresenta alguns problemas na mineralogia, principalmente na química mineral, o número de dados de microssonda eletrônica é muito bom, porém a apresentação dos mesmos na tabela 4 é confusa, os resultados das fórmulas minerais não estão separados por sítios, o que dificulta a classificação das mesmas, os diagramas de classificação também apresentam erros, principalmente a figura F e a G. Também não é informado como foi feito o cálculo de fórmula, nem a proporção de Fe^{2+} e Fe^{3+}.

A geoquímica e muito interessante, principalmente a análise de variação dos elementos nas diferentes zonas de alteração hidrotermal, embora falte uma tabela com os dados químicos utilizados. Na página 47 ocorre também um erro na numeração das figuras, a figura F (E, F, G, H, I e J) são respectivamente figura 8 (e, F, G, H, I e J)

A discussão é muito boa e utiliza bem os resultados obtidos para a interpretação dos fenômenos. As conclusões estão bem escritas e demonstram que os objetivos do trabalho foram plenamente atingidos.

Embora tenha alguns pequenos problemas o trabalho é de alta qualidade e é uma ótima contribuição para o conhecimento da mineralização na região.

O conceito final é A - excelente.

Assinatura: _[assinatura]_   Data: 11/01/2019

Ciente do Orientador:

Ciente do Aluno:

ANEXO I

Título da Dissertação/Tese:

"GEOLOGIA E GEOQUÍMICA DA ZONA INFERIOR DO CORPO DE MINÉRIO INGÁ, DISTRITO AURÍFERO DE CRIXÁS, GOIÁS, BRASIL: IMPLICAÇÕES GENÉTICAS E EXPLORATÓRIAS"

Área de Concentração: Geoquímica

Autor: **Marco Antônio Sartori Castoldi**

Orientador: Prof. Dr. José Carlos Frantz

Examinador: Prof. Dr. Diego Machado Marques

Data: 07/01/2019

Conceito: A

PARECER:

A dissertação de mestrado de **Marco Antônio Sartori Castoldi** apresenta um texto estruturado e bem escrito. O tema trata de um assunto relevante, tanto do ponto de vista científico quanto do ponto de vista econômico por caracterizar a evolução geológica e metalogenética de parte do greenstone belt de Crixás, relacionando com as mineralizações auríferas.

O texto foi bem redigido e organizado. O capítulo inicial com o estado da arte e a contextualização teórica está adequado ao proposto de tema da dissertação. As referências bibliográficas são compatíveis com o tema e atualizadas.

A estrutura da dissertação está de acordo com as normas do PPGgeo, sendo um capítulo introdutório e um artigo científico, sendo este a parte principal do trabalho.

As informações no artigo estão claramente discutidas, sendo a linguagem adequada. A localização da área de estudo bem como o contexto geológico são bem definidos, permitindo o bom entendimento dos dados relacionados a pesquisa. A revisão bibliográfica é abrangente e pertinente aos assuntos da dissertação em questão. A metodologia utilizada dispõe de técnicas modernas e complementares, permitindo uma boa caracterização da área de estudo.

O estudo apresenta uma contribuição significativa na avaliação metalogenética do greenstone belt de Crixás, fornecendo uma petrografia detalhada dos furos de sondagem selecionados, bem como a química mineral e dados geoquímicos. No entanto, a apresentação das informações sobre os resultados foi extensa, dificultando a leitura em alguns momentos (principalmente se tratando de um artigo). Uma parte importante em um trabalho de mestrado é a interpretação de dados e não os dados brutos, podendo esses ser apresentados em forma de anexo se assim o aluno desejar. Lembrando que essa observação tem o objetivo de ajudar o aluno a aprimorar o trabalho, não desabonando o que foi feito.

A dissertação é considerada de muito boa qualidade e atingiu plenamente os critérios para aprovação. Parabenizo a autora, seus orientadores e o PPGGeo pela excelência do trabalho. O texto permitiu avaliar de forma adequada o desenvolvimento do trabalho, sendo que o mesmo preenche os requisitos necessários para ser considerado uma dissertação de mestrado. O mesmo apresenta uma base teórica adequada do tema escolhido. Os métodos escolhidos são coerentes com a proposta do estudo e os resultados estão em sintonia com as discussões. Os resultados obtidos são interessantes e podem ser a base para trabalhos futuros com outas bases de dados, a fim de complementar o trabalho.

Assinatura: Data:07/01/2017

Ciente do Orientador:

Ciente do Aluno: